# Spin and Heat Transport in Nanoscale Superconductor Hybrid Structures

Zur Erlangung des akademischen Grades eines
DOKTORS DER NATURWISSENSCHAFTEN
durch die Fakultät für Physik
des Karlsruher Instituts für Technologie

genehmigte

DISSERTATION

von

Dipl.-Phys. Stefan Kolenda
aus Würzburg

Tag der mündlichen Prüfung: 20.01.2017
Referent: Priv.-Doz. Dr. Detlef Beckmann
Korreferent: Prof. Dr. Alexey Ustinov

# Contents

# 1 Introduction

Superconductivity and ferromagnetism are competing quantum mechanical ground states of the electron system in solid state systems. While ferromagnets prefer to align the electron spins in parallel, the microscopic origin of conventional superconductivity is the condensation of electrons into Cooper pairs with antiparallel spin orientation. Due to their competing order, at the interface of a ferromagnet and a superconductor fascinating effects can occur. In recent years, especially the creation of odd-frequency triplet supercurrents has gained lots of interest [1–6]. Here, the conversion of conventional s-wave paired supercurrent into triplet paired supercurrent by the use of inhomogeneous magnetization at the interface is studied, mostly in Josephson junctions which have a ferromagnetic weak link. Triplet paired superconductivity is of special interest as it can provide fully spin-polarized lossless currents and opens the field of superconducting spintronics [7, 8].

Also interesting in this context are recent experimental works which report long-range quasiparticle spin transport [9–13] in spin-split superconductors. In these experiments a local spin imbalance was created at an injector contact by injecting quasiparticles of a certain spin projection using the energy dependence of the spin-split density of states in the superconductor. Spin imbalance signals were measured with several ferromagnetic electrodes in a nonlocal measurement geometry for various distances. From the decay of these signals the spin diffusion length of the superconductor could be extracted. Surprisingly, a length scale of several $\mu m$ was found, much larger than the relaxation length in the normal state and also larger than the charge imbalance relaxation length [14, 15]. Hence, the separation of charge and spin currents is possible in nanoscale superconducting hybrid structures. Initially, the origin of the large spin diffusion length was unclear until recent theory works [16–19] showed that the nonlocal signals are of thermoelectric origin. They arise as the superconductor is heated by the injection of quasiparticles, so that a temperature difference to the detector contact is created. Therefore, at the detector contact a thermoelectric current flows which results in the nonlocal signals. Modeling of the nonlocal conductance by using this theory showed excellent agreement with the experimental data [16]. Furthermore, the theory is consistent with similar theoretical works which recently predicted large thermoelectric effects in ferromagnet/superconductor tunnel junctions [20, 21] in spin-split superconductors due to the broken electron-hole symmetry.

In the first part of this work, an experiment is shown which directly demonstrates the thermoelectric effect in such a junction in high magnetic fields. In order to do that ferromagnetic/superconductor hybrid structures were fabricated which enable to generate a temperature difference across the tunnel junction by heating the ferromagnet, while at the same time it was possible to detect the resulting thermoelectric current which flowed across the junction. As we will see, the resulting current is spin-polarized and directly proofs the coupling of spin and heat transport in spin-split superconductors. This is also interesting in so far as it was recently shown that the interplay of spin

and heat currents in normal metal ferromagnet structures leads to spin-dependent Seebeck [22] and Peltier [23] effects which have created the field of spin caloritronics [24]. The thermoelectric effect in ferromagnet/superconductor tunnel junctions is predicted to be larger [20, 21, 25–27] than in normal metal structures and so it opens up the possibility for high-sensitive local electron thermometry [28] as well as for improved local electronic refrigeration [29, 30] working on the principle of microrefrigerators based on normal metal/insulator/superconductor tunnel junctions [31, 32].

In the second part of this work the studies of the thermoelectric effect are expanded to systems for which the superconductor is in proximity contact to a ferromagnetic insulator. The experiments shown here base upon the work of Michael J. Wolf [33] who established the fabrication of thin films of the ferromagnetic insulator europium sulfide and studied the conductance in europium sulfide/aluminum proximity systems. In accordance with similar older experiments [12, 34–37], his work showed that in these systems an intrinsic exchange field appears which boosts the spin-splitting in the superconductor in addition to the applied magnetic field. The proximity systems are therefore favorable candidates for providing large spin splitting also in small applied fields and for enabling the local control over the spin-splitting field in the superconductor [38]. However, the strength of the exchange field depends sensitively on the quality of the europium sulfide/aluminum interface and is not understood sufficiently, especially in the range of small applied fields. We will therefore first show further local spectroscopy measurements which provide the possibility to investigate the intrinsic exchange field and its dependence on the applied magnetic field. Later, studies of the influence of the exchange field on the thermoelectric signal are presented which also revealed promising results.

In the last part of the work, first results of a new spin transport experiment are presented. The experiment is based on the spin transport measurements of Hübler et al. [9] and Wolf et al. [11], but here also the case of perpendicular alignment between the magnetization of the ferromagnetic electrodes and the induced Zeeman splitting in the superconductor is investigated. In this case, it is proposed that spin-Hanle precession of the quasiparticle spin should occur [39] which would be measurable in the nonlocal spin signal. Studies of the spin-Hanle precession were already successfully done in structures consisting of normal metals [40–42] or semiconductors [43, 44], but are missing for superconductors so far.

# 2 Theory

This chapter deals with an introduction to the theoretical basics which are essential for the understanding of the following experimental work. The chapter starts with an overview of the antagonistic phenomena ferromagnetism and superconductivity. For that matter it is based on the textbooks of S. Blundell "Magnetism in condensed matter" [45] and M. Tinkham "Introduction to superconductivity" [46] in analogy to reference [33]. Building up on this, phenomena which occur in nanoscale superconducting hybrid structures are discussed. Here, particular attention is paid to the interplay of superconductivity and ferromagnetism at interfaces and in the generation of thermoelectric effects in superconductor ferromagnet hybrid structures.

Throughout this work, the abbreviations F,I,S and N are used to denominate ferromagnetic, insulating, superconducting and normal metal parts of the structures, e.g. FIS for a ferromagnet/insulator/superconductor junction.

## 2.1 Ferromagnetism

Ferromagnetism is a type of magnetic order in which the magnetic moments lie in parallel alignment. Here, the phenomenon is briefly discussed for insulating materials where it is induced by localized magnetic moments as well as for magnetic metals where it is induced by magnetism of the interacting electron gas.

### 2.1.1 Magnetism of local moments

Quantum mechanical exchange interactions which are generated by electrostatic interactions and the Pauli principle [45, chapter 4.2] lead to long range order of isolated magnetic moments in certain materials. In an applied magnetic field $\mathbf{B}$ this is described by the Hamiltonian [45, chapter 5.1]

$$\mathcal{H} = -\sum_{ij} J_{ij}\mathbf{S}_i \cdot \mathbf{S}_j + g\mu_\mathrm{B}\sum_j \mathbf{S}_j \cdot \mathbf{B} \tag{1}$$

where $J_{ij}$ is the exchange constant between the spins $\mathbf{S}_i$ and $\mathbf{S}_j$, g is the Landé factor and $\mu_\mathrm{B}$ is the Bohr magneton. For ferromagnetic alignment the exchange constant is positive. To solve the problem it is useful to make an approximation and to introduce the effective molecular field

$$\mathbf{B}_\mathrm{mf} = -\frac{2}{g\mu_\mathrm{B}}\sum_j J_{ij}\mathbf{S}_j. \tag{2}$$

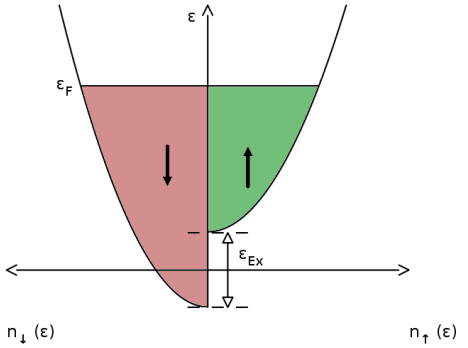


**Figure 2.1:** Density of states showing spontaneous splitting of the energy bands by the exchange energy $\varepsilon_{\mathrm{ex}}$. After Fig. 13(a) in [45]

In physical terms this means that the exchange term is replaced by an effective field which is generated by the neighboring spins. Inserting it into equation (1), the Hamiltonian is written as

$$\mathcal{H} = g\mu_{\mathrm{B}} \sum_i \mathbf{S}_i \cdot (\mathbf{B} + \mathbf{B}_{\mathrm{mf}}) \tag{3}$$

which is equivalent to the problem of a paramagnet in the field $(\mathbf{B} + \mathbf{B}_{\mathrm{mf}})$. Within the Weiss model of ferromagnetism it can be solved by simultaneously solving the equations

$$\frac{M}{M_{\mathrm{S}}} = B_J(y) \quad \text{and} \quad y = \frac{g_J \mu_{\mathrm{B}} J(B + \lambda M)}{k_{\mathrm{B}} T} \tag{4}$$

where $\lambda M = B_{\mathrm{mf}}$ is the molecular field, $B_J(y)$ is the Brillouin function, $k_{\mathrm{B}}$ is the Boltzmann constant and $g_J$ is the Landé factor of the magnetic moment $J$. From the coupling strength of the molecular field $\lambda$ and the saturation magnetization $M_{\mathrm{S}}$ the Curie temperature can be inferred by

$$T_{\mathrm{Cu}} = \frac{g_J \mu_{\mathrm{B}} (J+1) \lambda M_{\mathrm{S}}}{3 k_{\mathrm{B}}}. \tag{5}$$

### 2.1.2 Magnetism of the electron gas

Ferromagnetism exists not only in insulators, but can also be induced in metals by magnetism of the electron gas. In a metal, the energy dispersion relation for the approximation of the free electron gas is given by

$$\varepsilon(\mathbf{k}) = \frac{(\hbar k)^2}{2m^*} \tag{6}$$

where $\hbar = h/2\pi$ is the reduced Planck constant and $m^*$ is the effective mass of the electron in the crystal representing the bending of the electron band. In a simple one band model the dispersion has the form of a parabola for both spin projections. Both spin bands are filled equally up to the Fermi energy $\varepsilon_{\mathrm{F}}$. However, in some metals it is energetically favorable to redistribute the electrons in a small energy range near $\varepsilon_{\mathrm{F}}$.

Thereby, the spin-degeneracy of the bands is lifted and the spin-up and spin-down bands are shifted by the exchange energy $\varepsilon_{\mathrm{ex}}$ with respect to each other. This is schematically depicted in Figure 2.1. Because the redistribution of the occupied states in principle needs energy, the energy gain which is reached by the magnetization $M = \mu_{\mathrm{B}}(n_\downarrow - n_\uparrow)$ must compensate it. To provide this, the Stoner criterion [45, chapter 7.3]

$$Un(\varepsilon_{\mathrm{F}}) \geq 1 \tag{7}$$

has to be fulfilled. Here, $U$ is a measure of the exchange energy and $n(\varepsilon_{\mathrm{F}})$ is the density of states at the Fermi energy. Thus, the condition requires strong exchange interaction and a large density of states at the Fermi energy.

The band splitting results in an inequality of $n_\downarrow(\varepsilon_{\mathrm{F}})$ and $n_\uparrow(\varepsilon_{\mathrm{F}})$. Since many electronic properties of a metal are directly dependent on the density of states at the Fermi energy, it is useful to define the spin polarization

$$P_n = \frac{n_\downarrow(\varepsilon_{\mathrm{F}}) - n_\uparrow(\varepsilon_{\mathrm{F}})}{n_\downarrow(\varepsilon_{\mathrm{F}}) + n_\uparrow(\varepsilon_{\mathrm{F}})} \tag{8}$$

to characterize the ferromagnet.

## 2.2 Superconductivity

Superconductivity is named after its most outstanding property, the loss of its ohmic resistance and the lossless conduction of currents below a critical temperature $T_{\mathrm{c}}$. The microscopic origin for superconductivity is the condensation of each two electrons with energies near the Fermi energy $\varepsilon_{\mathrm{F}}$ into Cooper pairs. The corresponding theory was first postulated by Bardeen, Schrieffer and Cooper [47] and is named after its discoverers "BCS-theory". It is based on the discovery by Cooper [48] that a net attractive interaction amongst the electrons leads to the formation of electron pairs. In conventional superconductors this interaction is mediated via virtual phonons. Considerations of the phase space show that the attractive interaction is most favorable for electrons which have opposite spin and opposite momentum. In the formalism of second quantization the BCS ground state is given by

$$|\Psi_G\rangle = \prod_{\mathbf{k}=\mathbf{k}_1,\ldots,\mathbf{k}_M} (u_{\mathbf{k}} + v_{\mathbf{k}} c^*_{\mathbf{k}\uparrow} c^*_{-\mathbf{k}\downarrow})|\Phi_0\rangle \tag{9}$$

where $|u_{\mathbf{k}}|^2 + |v_{\mathbf{k}}|^2 = 1$ and $|\Phi_0\rangle$ is the vacuum ground state. The creation operators $c^*_{\mathbf{k}\uparrow}$ and $c^*_{-\mathbf{k}\downarrow}$ create a pair of electrons with opposite momentum and spin that is occupied with probability $|v_{\mathbf{k}}|^2$, while the pair state is unoccupied with the probability $|u_{\mathbf{k}}|^2$. The reduced Hamiltonian in grand canonical ensemble reads

$$\mathcal{H} - \mu N = \sum_{\mathbf{k},\sigma} \xi_{\mathbf{k}} n_{\mathbf{k},\sigma} + \sum_{\mathbf{kl}} V_{\mathbf{kl}} c^*_{\mathbf{k}\uparrow} c^*_{-\mathbf{k}\downarrow} c_{-\mathbf{l}\downarrow} c_{\mathbf{l}\uparrow} \tag{10}$$

with the single particle energies $\xi_{\mathbf{k}} = \varepsilon_{\mathbf{k}} - \mu$ measured with respect to the chemical potential (or Fermi energy) $\mu = \varepsilon_{\mathrm{F}}$. Here introduced are the annihilation operators $c_{\mathbf{k}\sigma}$, the particle number operator $n_{\mathbf{k},\sigma} = c^*_{\mathbf{k}\sigma} c_{\mathbf{k}\sigma}$ and the scattering potential $V_{\mathbf{kl}}$. Here, the indices **l,k** describe momentum states, while $\sigma$ describes the spin state. In the Hamiltonian of equation (10) terms which involve unpaired electrons are omitted. Using a mean field approximation first simplifies the Hamiltonian, in the following it can be treated with a canonical transformation [49], [46, chapter 3.5]. Thereby, new Fermi operators $\gamma_{\mathbf{k}0}$ and $\gamma^*_{\mathbf{k}1}$ are defined which later can be identified as single particle excitation creation and annihilation operators. The appropriate transformation reads

$$c_{\mathbf{k}\uparrow} = u^*_{\mathbf{k}} \gamma_{\mathbf{k}0} + v_{\mathbf{k}} \gamma^*_{\mathbf{k}1} \tag{11}$$

$$c_{\text{-}\mathbf{k}\downarrow} = -v^*_{\mathbf{k}} \gamma_{\mathbf{k}0} + u_{\mathbf{k}} \gamma^*_{\mathbf{k}1} \tag{12}$$

where $|u_{\mathbf{k}}|^2 + |v_{\mathbf{k}}|^2 = 1$. Further calculations show that with the choice of the coherence factors

$$|u_{\mathbf{k}}|^2 = \frac{1}{2}\left(1 + \frac{\xi_{\mathbf{k}}}{E_{\mathbf{k}}}\right), \quad |v_{\mathbf{k}}|^2 = \frac{1}{2}\left(1 - \frac{\xi_{\mathbf{k}}}{E_{\mathbf{k}}}\right) \tag{13}$$

the Hamiltonian can be diagonalized.

For single particle excitations, the so called quasiparticles, the energy dispersion is found to be

$$E_{\mathbf{k}} = (\xi^2_{\mathbf{k}} + |\Delta_{\mathbf{k}}|^2)^{1/2}. \tag{14}$$

Here $\Delta_{\mathbf{k}}$ plays the role of an energy gap since below that energy single particle states do not exist. As density of states (DOS) for quasiparticles one obtains the so-called BCS density of states [46, chapter 3.7]

$$\frac{n_{\mathrm{S,BCS}}}{n_0} = \frac{d\xi}{dE} = \begin{cases} \frac{E}{\sqrt{E^2 - \Delta^2}} & \text{for } |E| > \Delta \\ 0 & \text{for } |E| < \Delta \end{cases} \tag{15}$$

where $n_0$ is the normal-state density of states. So, there is a singularity in the DOS for quasiparticles for $|E| = \Delta$ and the DOS converges to the normal state value for $E \to \infty$.

## 2.3 Tunneling in superconductor hybrid structures

Tunneling is a quantum mechanical process which allows particles of energy $\varepsilon$ to overcome potential barriers $V > \varepsilon$. The condition for allowing this classically forbidden process is that the barrier is thin enough, so that the wave function of the particle has a tail and therefore a non-vanishing probability density behind it. In solid state physics tunnel junctions are often realized by thin insulating barriers between two materials. For dealing with superconductors tunnel junctions to normal metals were found to be quite useful. With the measurement of current flowing across a normal metal/superconductor tunnel contact, I. Giaever [50] confirmed in 1960 the existence

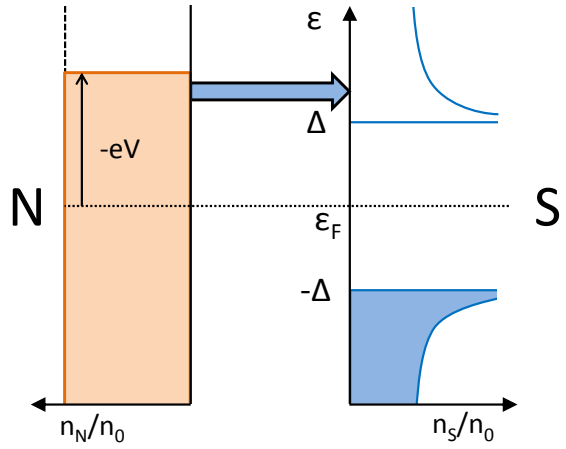


**Figure 2.2:** Schematic illustration of a normal metal/superconductor tunnel junction in the semiconductor picture. After Figure 3.6 in [46].

of the energy gap in the density of states of a superconductor and therefore the BCS theory.

The tunneling process is illustrated in Figure 2.2 in the semiconductor picture. On the left side the density of states of the normal metal (N) is depicted, on the right side the DOS of the superconductor (S). In the normal metal the chemical potential may be tuned by the voltage $V$ which can be provided by a dc-power source. Tunneling is only possible, if states with the same energy $\varepsilon$ are occupied on one side of the barrier and unoccupied on the other side. So, for small voltages $|eV| < \Delta$ tunneling is forbidden in the NIS junction due to the vanishing DOS in the superconductor in the energy gap. Electrons can only tunnel from N into S, if their energies are tuned to $-eV > \Delta$. Also possible is the reverse process that electrons tunnel from S into N for energies $-eV < -\Delta$. Mathematically the tunnel current is described by [46, chapter 3.8]

$$I_{\mathrm{T}}(V) = \frac{G_{\mathrm{T}}}{e} \int_{-\infty}^{\infty} n_{\mathrm{S}}(\varepsilon)(f_0(\varepsilon - eV) - f_0(\varepsilon))d\varepsilon \tag{16}$$

where $G_{\mathrm{T}}$ is the normal state tunnel conductance of the junction, $e = -|e|$ is the charge of the electron, $n_{\mathrm{S}}$ is the normalized density of states in S and

$$f_0 = \frac{1}{e^{(\varepsilon-\mu)/k_{\mathrm{B}}T} + 1} \tag{17}$$

is the Fermi distribution on both sides of the barrier. A more direct comparison between theory and experiment is done by building the differential conductance $g = dI_{\mathrm{T}}/dV$ of the tunnel junction which is the derivative of equation (16) after the voltage $V$. It reads

$$g = \frac{dI_{\mathrm{T}}}{dV} = G_{\mathrm{T}} \int_{-\infty}^{\infty} n_{\mathrm{S}}(\varepsilon) \frac{\partial f_0(\varepsilon - eV)}{\partial(eV)} d\varepsilon. \tag{18}$$

As $\partial f_0(\varepsilon - eV)/\partial eV$ is a bell shaped function with width $4k_{\mathrm{B}}T$, the differential conductance reflects the DOS in the superconductor additionally broadened by the thermal smearing. Hence, the measurements of $g$ is a powerful tool to investigate the properties

of superconducting tunnel junctions, especially for $T \to 0$.

For tunnel junctions between ferromagnets and superconductors the tunnel current is modified due to the finite polarization $P_n$ of the ferromagnet. In a simple picture where spin flips in the insulator are neglected it can be described by the model of two independent spin currents. The tunnel equation then reads

$$I_{\mathrm{T}}(V) = \frac{G_{\mathrm{T}}}{2e} \int_{-\infty}^{\infty} ((1-P)n_+(\varepsilon) + (1+P)n_-(\varepsilon))(f_0(\varepsilon - eV) - f_0(\varepsilon))d\varepsilon \tag{19}$$

where $n_+(\varepsilon)$ and $n_-(\varepsilon)$ are the density of states for spin-up and respectively spin-down quasiparticles. Note that

$$P = \frac{G_\downarrow - G_\uparrow}{G_\downarrow + G_\uparrow} \tag{20}$$

describes the polarization of the tunnel junction and not the polarization of the ferromagnet. Here, $G_{\uparrow,\downarrow}$ is the normal-state conductance of the respective spin projection.

To describe tunneling in high magnetic fields $B$ and with non-zero temperature $T$ properly the previous model for the density of states in S has to be extended. In order to do that spin-orbit scattering effects and orbital pair breaking have to be included. Then, the DOS for both spin projections is given by [51–53]

$$n_\pm = \mathrm{Re}\left(\frac{u_\pm}{\sqrt{u_\pm^2 - 1}}\right) \tag{21}$$

where the complex quantities $u_\pm$ have to be found by the implicit equation

$$\frac{\varepsilon \mp \mu_{\mathrm{B}} B}{\Delta} = u_\pm \left(1 - \frac{\Gamma}{\Delta}\frac{1}{\sqrt{1-u_\pm^2}}\right) + b_{\mathrm{so}} \left(\frac{u_\pm - u_\mp}{\sqrt{1-u_\mp^2}}\right). \tag{22}$$

Here, the pair breaking parameter $\Gamma$ and the spin-orbit scattering strength $b_{\mathrm{so}} = \hbar/3\tau_{\mathrm{so}}\Delta$ are introduced while higher order terms of $b_{\mathrm{so}}$ are neglected.

In Figure 2.3 the influence of the magnetic field and the specific junction parameters on the conductance of a tunnel junction is illustrated by some examples. In each panel the black curve represents the total conductance, while the red and the green curves represent the parts of the respective spin projection as indicated by the red and green arrows. The spin-splitting field $B = 1$ T and the temperature $T_0 = 100$ mK are chosen here. In Figure 2.3(a) the conductance is shown for a junction with $P = 0$. Orbital pair breaking and spin-orbit scattering are also neglected first. We see that the magnetic field induces a Zeeman splitting of the quasiparticle DOS and so the energies of the spin-down and spin-up quasiparticles are shifted by $\pm\mu_{\mathrm{B}}B$ with respect to each other. The conductance now exhibits four coherence peaks instead of the two which are found in zero field. Consequently, the energy gap is reduced to the value $E_{\mathrm{G}} = \Delta - 2\mu_{\mathrm{B}}B$.

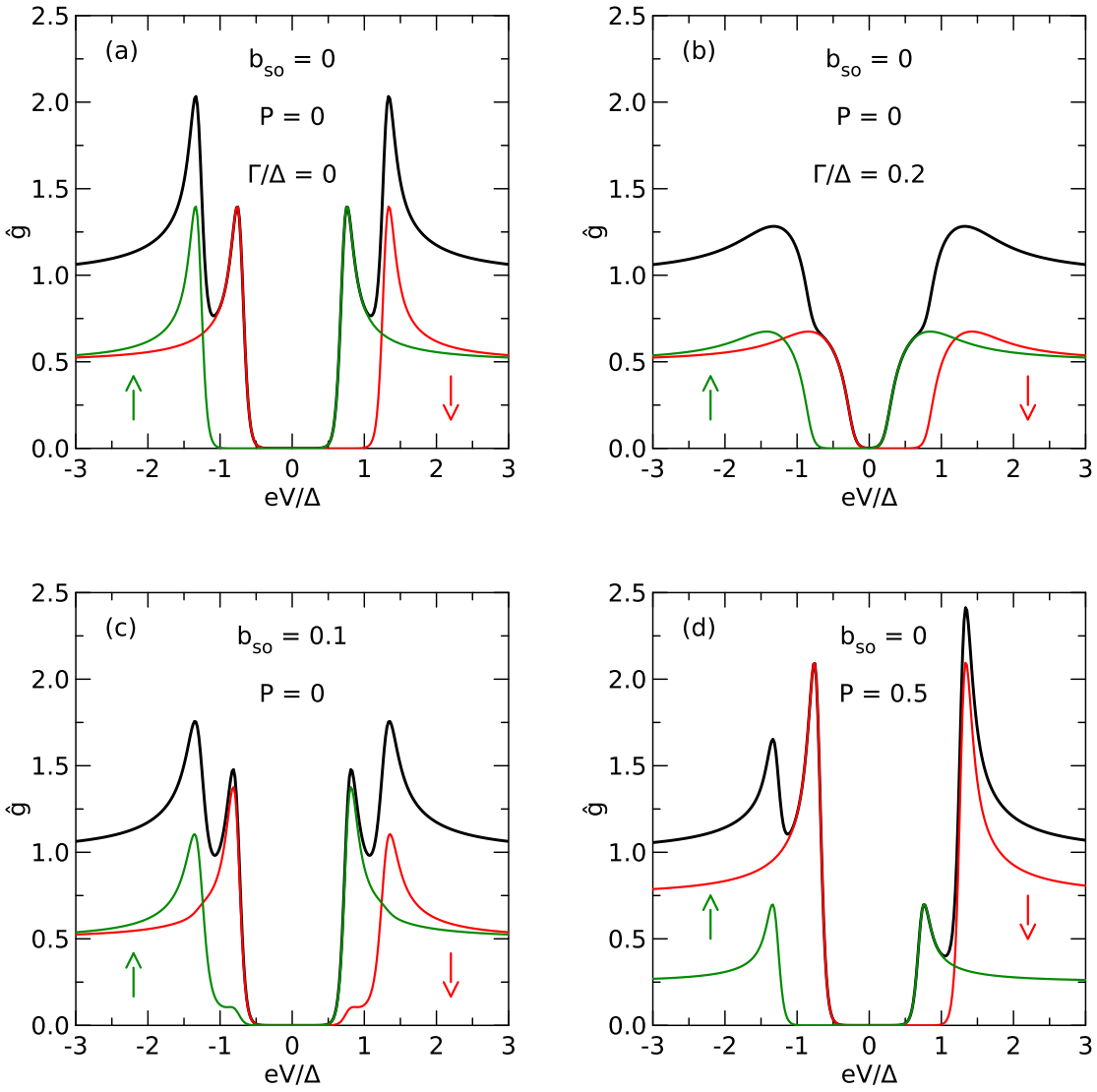


**Figure 2.3:** Normalized differential conductance $\hat{g} = g/G_\mathrm{T}$ as a function of the voltage $eV$ in units of the pair potential $\Delta$. The black curve represents the total conductance, the red and green ones the contributions of the particular spin projections, marked with an arrow. The curves are shown for the pair potential $\Delta = 200$ $\mu$eV, the spin-splitting field $B = 1$ T and the temperature $T_0 = 100$ mK. In panels (a) and (b) the polarization $P = 0$ and the spin-orbit scattering strength $b_\mathrm{so} = 0$ are set. The pair breaking parameter is $\Gamma/\Delta = 0$ (panel (a)), respectively $\Gamma/\Delta = 0.2$ (panel (b)). Conductance curves with parameters $P = 0$ and $b_\mathrm{so} = 0.1$ are shown in panel (c) and curves with $P = 0.5$ and $b_\mathrm{so} = 0$ are shown in panel (d). In these panels $\Gamma/\Delta = 0$. After Figure 2.4 in [33].

Next, the influence of the orbital pair breaking effects on the density of states in S is discussed. The magnetic field affects the orbital motion of the electrons and breaks the time-reversal degeneracy of the paired states. The first theory to describe this effect was developed by Abrikosov and Gor'kov [54], initially for certain concentrations of magnetic impurities in superconductors. Later, Maki [55] showed that the impact of the magnetic field on the electron motion in thin superconducting films can be described in the same way and by using only one pair breaking parameter $\Gamma$. Figure 2.3(b) shows that including the pair breaking parameter $\Gamma/\Delta = 0.2$ into the model for the DOS leads to broadening of the coherence peaks in the conductance and further reduction of the energy gap $E_\mathrm{G}$. A detailed study about this reduction can be found in reference [56].

In Figure 2.3(c) spin-orbit scattering effects are included while the pair breaking parameter is set to zero again. The spin-orbit scattering leads to spin flips of the quasiparticles, so that the spin projections are mixed and quasiparticles of a certain spin projection have also a small DOS part in the other spin band. In the spin-separated conductance curves (red and green lines) this is visible by the small shoulders which are formed just above the energy gap. However, in the total conductance which is experimentally accessible this effect is hard to observe for $b_\mathrm{so} \ll 1$.

Finally, the influence of a finite polarization $P$ on the tunneling conductance is discussed. The spin polarization of the junction represents the difference in the conductance for spin-up and spin-down electrons. Thus, the symmetry of the conductance around the Fermi energy is broken and the coherence peaks differ in height for positive and negative energies. This is visible in Figure 2.3(d) where the polarization $P = 0.5$ and the other parameters $\Gamma = b_\mathrm{so} = 0$ were chosen. In return, one can extract the spin polarization of a tunnel junction by comparing the heights of the inner conductance peaks. In such way, Tedrow and Meservey [57] could extract the spin polarization of a superconducting tunnel junction to ferromagnetic nickel. Thereby, they were the first to measure spin-dependent conductance in superconductor hybrid structures.

## 2.4 Nonequilibrium superconductivity

If current flows from a normal metal (or ferromagnet) into a superconductor, the population of the quasiparticle states is driven out of equilibrium [46, chapter 11.2]. In thermal equilibrium the quasiparticles states in S are occupied with the probability given by the Fermi distribution $f_0(E_k/k_\mathrm{B}T)$ where the energy $E_k$ of the state is described by equation (14). The injection of electrons via tunneling processes changes the occupation of states and it must be described now by the actual occupation number $f_k \neq f_0(E_k/k_\mathrm{B}T)$. It is important now to notice that the quasiparticle spectrum has an electron-like ($\xi > 0$) and a hole-like ($\xi < 0$) branch and that the quasiparticle charge $q_k^* = e\xi_k/E_k$ is energy dependent. The fractional charge represents the fact that the quasiparticle creation and annihilation operators are linear combinations of the electron creation and annihilation operators (c.f. equation (12)). This also implies that an

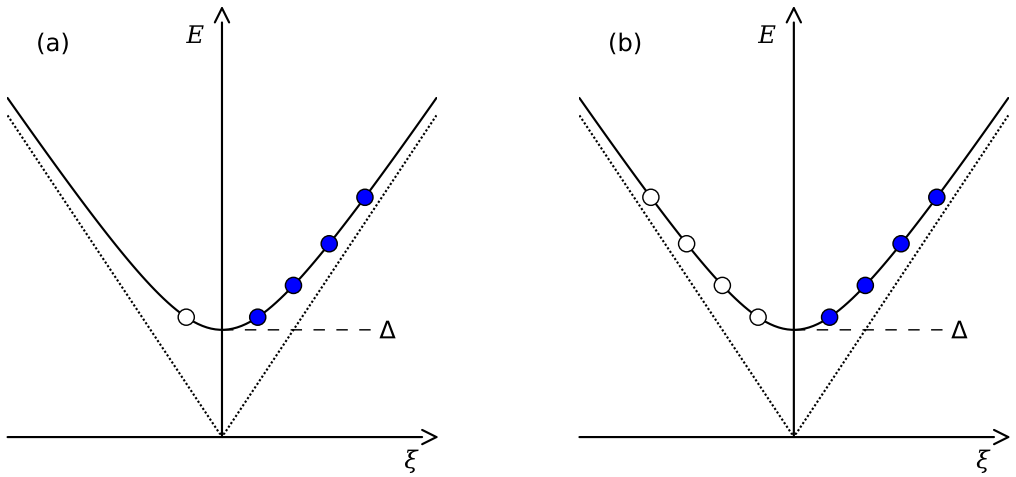


**Figure 2.4:** Dispersion curve of excitation energies in the superconducting (solid line) and normal (dashed line) state. Schematic illustration of the branch population in (a) the charge imbalance regime and (b) the energy imbalance regime. Adapted from Figure 11.1 in [46].

electron that tunnels into the superconductor has unequal coherence factors for being converted into an electron-like or a hole-like quasiparticle.

So, the so-called charge imbalance [58, 59] is created which is characterized by the unequal population of both branches (see Figure 2.4(a)). It can be classified by the quasiparticle charge

$$Q^* = 2n_0 \int_{-\infty}^{\infty} q_k^*(\xi) f_k(\xi) d\xi. \tag{23}$$

This quantity can be observed in nanoscale structures by nonlocal detection techniques [14]. It is only non-zero for unequal occupation numbers $f_k(\xi) \neq f_k(-\xi)$. To maintain electrical neutrality the chemical potential of the superconducting pairs is shifted out of its equilibrium value.

Another kind of nonequilibrium is the so-called energy imbalance. It is schematically depicted in Figure 2.4(b). It is characterized by an equal population of the branches which is higher than in thermal equilibrium. It is only indirectly measurable via the self-consistency equation for the pair potential [46]

$$1 + \mathcal{V} \int_{-\infty}^{\infty} \frac{1 - 2f_k(\xi_k)}{\sqrt{\Delta^2 + \xi_k^2}} d\xi = 0 \tag{24}$$

where $\mathcal{V}$ is the pairing interaction. One can define the effective temperature $T_S^*$ of the superconductor by inverting equation (24). Then $\Delta(T_S^*)$ equals the $\Delta(f_k)$.

It should be mentioned here that there is also a more general theory for nonequilibrium phenomena in superconductors, developed by A. Schmid and G. Schön [60]. In this

theory the model of quasi-classical Green's functions is used to describe the nonequilibrium effects. The charge imbalance is labeled as "transverse" mode, while the energy imbalance is labeled as "longitudinal" mode.

## 2.5 Thermoelectric effect

The term thermoelectric effect describes the phenomenon that a temperature difference $\delta T$ applied across an electric conductor leads to an electric current and vice versa [61]. The appearance of the current can be understood as follows [24, box 1]. The temperature in the conductor is represented by the broadening of the Fermi function. In the case of a non-vanishing temperature gradient across the conductor, more electrons with energies $\varepsilon > \varepsilon_\mathrm{F}$ are populated in the hot region of the conductor than in the cold region due to the thermal excitations. In contrary, in the cold region more electrons with energies $\varepsilon < \varepsilon_\mathrm{F}$ are populated. Thus, high-energy electrons flow from the hot region to the cold one and low-energy electrons flow from the cold region to the hot one. Two competing currents form and small asymmetries of the conductance around the Fermi energy lead to a net thermoelectric current. If one prevents current flow by using an open circuit configuration, in equilibrium the electric potential $V$ will build up. The electric potential points against the temperature difference and is classified by the Seebeck coefficient

$$S = -\frac{V}{\delta T}. \tag{25}$$

For a normal metal the Seebeck coefficient can be derived in the Sommerfeld expansion by Mott's formula [62]

$$S = -eL_0 T \frac{\partial}{\partial \varepsilon} \ln \sigma(\varepsilon)|_{\varepsilon_\mathrm{F}} \tag{26}$$

where $L_0 = \pi^2 k_\mathrm{B}^2/3e^2$ is the Lorenz number and $\sigma(\varepsilon)$ is the conductivity of the material. In this formula, it is reflected that the sign and the magnitude of the thermoelectric effects depend on the symmetry of the conductance around the Fermi energy. As for a metal $\partial\sigma/\partial\varepsilon$ is of the order $\sigma/\varepsilon_\mathrm{F}$ in the Sommerfeld expansion [61, chapter 13], the Seebeck coefficients are of the order $k_\mathrm{B}T/\varepsilon_\mathrm{F}$. So, they are typically of the order of several $\mu eV$ at room temperature and vanishing in the sub-Kelvin regime where $k_\mathrm{B}T \ll \varepsilon_\mathrm{F}$. Better materials for thermoelectric effects are semiconductors where the chemical potential can be tuned by doping near the band edges, so that the symmetry of the density of states near $\varepsilon_\mathrm{F}$ is strongly broken.

Similarly, the breaking of the electron-hole symmetry can also be found for a spin-polarized superconductor tunnel junction in the presence of a magnetic field [20,21,25]. Figure 2.5 shows the generation of thermoelectric current in such a junction schematically. Here, the semiconductor picture is used again to show the energy dependence of the density of states in F and S, respectively. The superconductor is considered to stay at temperature $T_\mathrm{S} = T$ while the quasiparticle density of states is assumed to be spin-split by the magnetic field. As a consequence the energy of spin-down quasiparticles is lowered, while the energy of spin-up quasiparticles is raised and also the energy

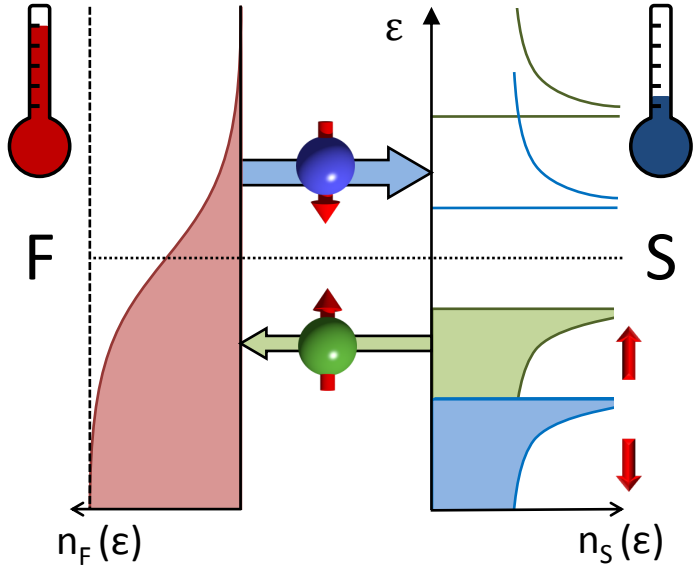


**Figure 2.5:** Density of states of a ferromagnet/superconductor tunnel junction in high magnetic field in the semiconductor picture. The ferromagnet is heated to the temperature $T_\mathrm{F} = T_\mathrm{S} + \delta T$. The resulting spin-polarized currents are sketched with arrows.

gap $E_\mathrm{G}$ is reduced depending on the magnetic field strength. Now, the ferromagnet is heated to the temperature $T_\mathrm{F} = T_\mathrm{S} + \delta T$, so that a finite temperature difference $\delta T$ is generated across the junction. The heating of F is reflected by the broadening of the Fermi distribution around $\varepsilon_\mathrm{F}$. Once the responsible energy scales are of the same order, $k_\mathrm{B}T_\mathrm{F} \approx E_\mathrm{G}$, two currents form. One of the currents consists of high-energy spin-down electrons which tunnel from F into the lower unpopulated spin-band in S. The other current consists of low-energy spin-up quasiparticles which tunnel from S into the free states of F. It is noteworthy that both currents are fully spin polarized and would cancel each other out in a non-polarized junction. However, here the polarization of the junction lifts the symmetry, so that a net current flows across it, driven by the temperature difference.

Mathematically, the effect can be described by adding the temperature dependence to the tunneling model, equation (19). It then reads [21]

$$I_\mathrm{T}(V,T,\delta T) = \frac{G_\mathrm{T}}{e}\int_{-\infty}^{\infty}\left[N_+(\varepsilon) + PN_-(\varepsilon)\right]\left[f_0(\varepsilon - eV, T+\delta T) - f_0(\varepsilon, T)\right]d\varepsilon \qquad (27)$$

where $N_+(\varepsilon) = (n_-(\varepsilon) + n_+(\varepsilon))/2$ is symmetric in energy, while $N_-(\varepsilon) = (n_-(\varepsilon) - n_+(\varepsilon))/2$ is asymmetric. The $n_\pm$ describe the density of states for spin-up and spin-down quasiparticles and have to be calculated by equation (21). Note that the thermoelectric current is generated by the asymmetric part of the density of states $N_-(\varepsilon)$ and can only be non-zero for $P \neq 0$.

Equation (27) describes both the conductance of the junction and the thermoelectric current, so that it can be used for modeling both quantities. For small voltage excita-

tions $V$ and small thermal excitations $\delta T/\overline{T}$ equation (27) can be linearized to

$$I = gV + \eta\frac{\delta T}{\overline{T}} \tag{28}$$

where $\overline{T} = T + \delta T/2$ is the average temperature of the junction. The thermoelectric coefficient $\eta$ is related to the Seebeck coefficient by

$$S = \frac{\eta}{g\overline{T}}. \tag{29}$$

Note that the characteristic energy scale of the thermoelectric effects in superconductor/ferromagnet tunnel junctions is not the Fermi energy $\epsilon_\mathrm{F}$ anymore, but the energy gap $E_\mathrm{G}$, so that the Seebeck coefficients are expected to be large.

## 2.6 Proximity effect

### 2.6.1 Proximity effect in metals

So far, only superconductors with tunnel junctions to metallic materials were considered, a situation where the influence of both materials on each other is weak and can be neglected. When the superconductor is in good transparent contact with a normal metal, this changes. Near the interface the superconducting pair amplitude can penetrate into N, while at the same time the superconductivity is weakened. The phenomenon is denominated as proximity effect. The microscopic reason for its existence is the Andreev reflection [63] which describes the conversion of normal current into supercurrent at a normal-metal/superconductor interface [64]. Assuming an electron with wave vector $k_\mathrm{F} + \delta k$ and energy $\xi_k < E_\mathrm{G}$ moves towards the surface, the electron can only be transferred into the superconductor if it forms a Cooper pair with an electron of the other spin projection. To provide energy and momentum conservation a hole with wave vector $k_\mathrm{F} - \delta k$ and energy $-\xi_k$ is retro-reflected at the interface. By forming the Cooper pair the incoming electron and the reflected hole are correlated in phase. Thus, a pair amplitude forms in the normal metal. In dirty metals the pair correlation is destroyed on the length scale $\lambda_\mathrm{N} = \sqrt{\hbar D/2\pi k_\mathrm{B} T}$ with the diffusion constant $D = v_\mathrm{F} l/3$ where $l$ is the mean free path before scattering [65]. On the other hand the conversion of normal current into supercurrent happens on the length scale of the coherence length in S, so that single electrons can penetrate into S on this length scale and the superconductivity is weakened.

For a ferromagnet in good contact with a superconductor, the situation is similar but differs due to the spin-dependent DOS in the ferromagnet. In F the spin-up and spin-down bands are split due to the exchange energy $\varepsilon_\mathrm{ex}$(Fig. 2.1), so that a difference $\delta k_\mathrm{F} = k_{\uparrow,\mathrm{F}} - k_{\downarrow,\mathrm{F}}$ is induced for the Fermi wave vectors of spin-up and spin-down electrons. The decrease of the proximity-induced superconductivity now occurs on the

length scale $\lambda_{\mathrm{F},1} = \sqrt{\hbar D/\varepsilon_{\mathrm{ex}}}$ [6, 66] and additionally the order parameter oscillates on the same length scale $\lambda_{\mathrm{F},2} = \lambda_{\mathrm{F},1}$. As in conventional ferromagnetic metals the exchange energy $\varepsilon_{\mathrm{ex}} \approx 1$ eV, the superconductivity is suppressed on the ferromagnetic side of the contact on the length scale $\lambda_{\mathrm{F},1} \approx 1$ nm and hard to detect experimentally. Detailed reviews about the proximity effect in ferromagnetic superconductor heterostructures can be found in references [1, 6, 7, 66].

### 2.6.2 Magnetically active interfaces

Finally the superconductor is considered to be in contact with a ferromagnetic insulator (FI). Due to the band gap, Cooper pairs and quasiparticles have a short decay length in the FI layer. The finite magnetization there creates a difference in the potential barrier height for spin-up and spin-down charge carriers which results in different reflection phases at the interface. So, the ferromagnetic insulator acts as spin-active interface and scattering at the interface has to be described by the spin-dependent scattering matrix [67, 68]

$$S = \exp(-i\phi/2)\exp[-i(\theta/2)\hat{\boldsymbol{\mu}} \cdot \boldsymbol{\sigma}] \tag{30}$$

where $\hat{\boldsymbol{\mu}}$ is the direction of magnetization and $\boldsymbol{\sigma}$ is the vector of Pauli matrices. Besides inducing an overall phase factor $\phi$, the scattering matrix S also rotates the spin vector around $\hat{\boldsymbol{\mu}}$ by the angle $\theta$. Such angle $\theta$ can be interpreted as a spin-mixing angle. The presence of spin mixing has consequences for the Cooper pairs. By scattering, Cooper pairs in a coherence length near the interface experience a singlet-triplet mixing [7]

$$\uparrow\downarrow e^{i\theta} - \downarrow\uparrow e^{-i\theta} = \cos(\theta)|0,0\rangle + i\sin(\theta)|1,0\rangle \tag{31}$$

where $|0,0\rangle$ represents the conventional singlet state and $|1,0\rangle$ the $m = 0$ component of the triplet state. Superconductors in contact with ferromagnetic insulators are therefore promising candidates for the investigation of triplet supercurrent.

The quasiparticle density of states is also affected by the spin-active scattering at the interface. This manifests itself by an intrinsic exchange field which boosts the effective spin-splitting in the density of states additional to the applied magnetic field. Experimentally the exchange field was first measured by Tedrow et al. [34] for structures consisting of thin aluminum films in direct contact with the ferromagnetic insulator europium oxide.

# 3 Experimental methods

In order to observe the physical effects which were introduced in the preceding chapter samples of sufficient quality with suitable dimensions and properties had to be fabricated. The required fabrication process is presented in the beginning of this chapter. Afterwards, the measurement methods which were used in the experiments are described. As the signal strength was usually small and the relevant signals had to be distinguished from background noises, high sensitivity was required for the measurements.

## 3.1 Preparation of superconducting hybrid structures

The preparation of superconducting hybrid structures was done in the research unit "Electron Transport and Quantum Control" at the Institute of Nanotechnology. Here, the production of samples has been established in a standard way over the last years (see references [15, 33, 69]). First masks out of polymethylmethacrylate (PMMA) were fabricated on top of silicon wafers with the use of e-beam lithography. In the following step these PMMA masks were utilized to produce metallic structures by the use of shadow evaporation technique.

In Figure 3.1 the fabrication of a single resist layer PMMA mask is illustrated schematically. As substrates silicon(100) wafers with 1000 nm thick oxide layers on top were used. Cleaning with a soft oxygen plasma was followed by the spin coating of the PMMA resist and a bake-out step. Mainly, resist layers with heights of approximately 800 nm were used. To structure the mask the wafers were placed in a scanning electron microscope (SEM). Here, desired areas of the resist were exposed by the electron beam. After the lithography process was finished, the wafers were developed in a solution containing one part of MIBK and three parts of isopropanol for approximately 20 seconds.

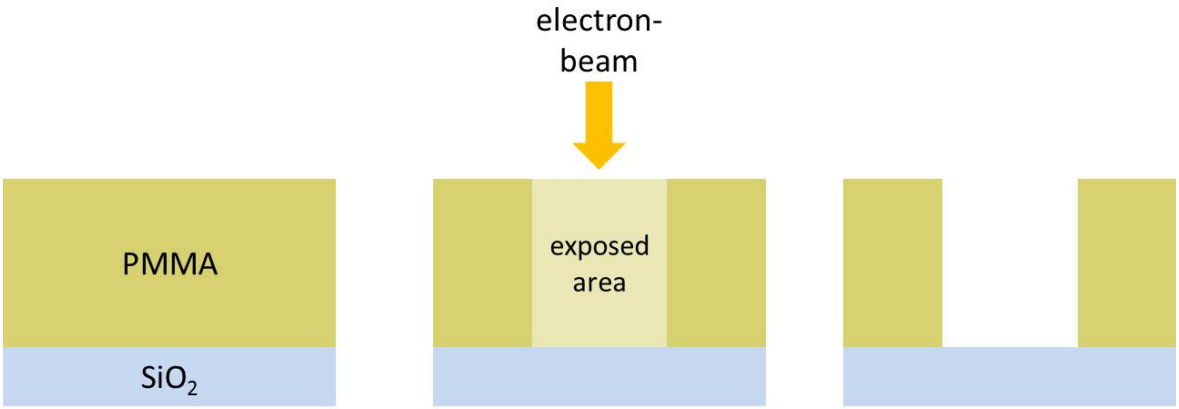


**Figure 3.1:** Schematic illustration of the fabrication of a PMMA mask.

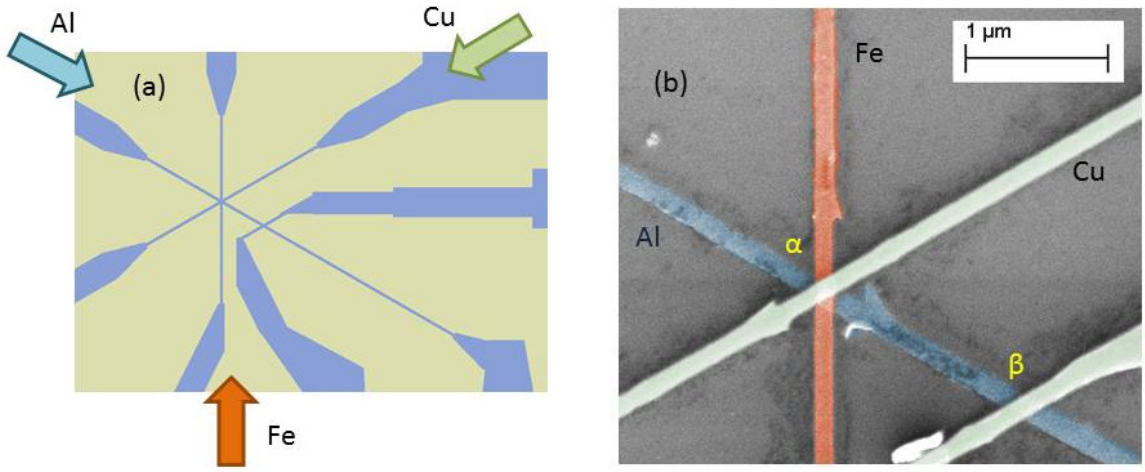


**Figure 3.2:** Schematic picture of the sample fabrication. (a) Design of the PMMA mask together with the evaporation directions of the metallic materials (arrows). (b) Colorized scanning electron microscope picture of the inner section of the sample after the evaporation.

During the development in the solution the exposed parts of the resist were washed away and only the unexposed parts stayed on the substrate forming the desired PMMA mask.

The wafers were clamped on a sample holder and mounted in an ultra-high vacuum evaporation system which consisted of a separate load lock and a main chamber that reached a base pressure down to $10^{-10}$ mbar. The main chamber of the system was equipped with a rotating and tilting support that enabled the evaporation of different materials from diverse angles. By choosing suitable rotation and tilt it was possible to fabricate metallic structures with the desired contacts while avoiding unwanted shorts at the same time. As an example, in the following the evaporation process of the samples used for the thermoelectric measurements is presented.

Figure 3.2 illustrates the appropriate evaporation process. In panel (a) the central part of the PMMA mask is depicted together with arrows that mark the direction from which the particular materials are evaporated. The exposed parts are colorized in blue, the remaining resist mask is colorized in beige. Onto a wafer with this mask the desired materials were evaporated in the following order. First, an aluminum strip with thickness $t_{\mathrm{Al}} \approx 20$ nm was evaporated. To form a thin tunnel barrier the sample was then transferred into the load lock and oxidized in-situ in a controlled oxygen atmosphere. Subsequently, the sample was transferred back into the main chamber and a ferromagnetic iron wire with thickness $t_{\mathrm{Fe}} \approx 20$ nm and two normal metal copper wires with thickness $t_{\mathrm{Cu}} \approx 50$ nm were evaporated. To improve the film qualities, especially that of the Al film, the wafers were cooled in the main chamber during the evaporation process to temperatures below $-100°\mathrm{C}$.

In panel (b) a false-color coded SEM picture of the inner part of a completed sample

is shown. The sample consists of a superconducting aluminum wire (blue) with two tunnel junctions. The junction $\alpha$ is a ferromagnetic tunnel junction formed by the aluminum wire and the iron wire (red). It is overlaid with an additional copper wire (green) which made it possible to measure the thermoelectric current across the tunnel junction while the ferromagnet is heated simultaneously. The junction $\beta$ is a normal metal tunnel junction formed by the aluminum wire and the second copper wire. It was used for control measurements throughout the experiments.

## 3.2 Preparation and characterization of europium sulfide films

In a later stage of this work, the thermoelectric effect was investigated also for samples which were fabricated on top of the ferromagnetic insulator europium sulfide (EuS). The preparation of EuS films was done in a different evaporation system at the "Physikalisches Institut" in Campus South with the help of Christoph Sürgers. The fabrication process of high quality EuS films has been established there for a longer time [70] and was reimplemented by Michael J. Wolf [33, 38]. Here, the basic steps are summarized briefly as the quality and the physical properties of the EuS-films depend sensitively on the evaporation conditions.

As substrates for the films silicon(111)-wafers were used. First, the wafers were cleaned in acetone, isopropanol and ethanol. For a proper cleaning the solutions were sonicated during the process. The cleaned substrates were etched in a buffered HF solution to remove the natural oxide and subsequently purged in double distilled water. Then, the wafers were mounted on a heatable sample holder and loaded in the evaporation system. The evaporation system used here consists of a main chamber which reaches base pressures down to $10^{-9}$ mbar and a top chamber, separated by a plate valve, which enables the sample exchange. After loading the sample into the system the top chamber was pumped separately and baked out over night with a heater band at $T \approx 120°C$ to improve the vacuum pressure. Then, both chambers were connected and the evaporation process started. Europium sulfide powder was evaporated from a tungsten crucible by $e$-beam evaporation. During the evaporation procedure the system pressure was in the range $10^{-7} - 10^{-6}$ mbar and the evaporation rate, checked with a quartz crystal monitor, was $0.1 - 0.2$ Å/s. To achieve better film quality the substrates were heated to $T_{\mathrm{sub}} \approx 700 - 800°\mathrm{C}$ as it is reported in the literature that under this condition better stoichiometry [71, 72] and magnetic properties [73] of the europium sulfide films are obtained. The temperature $T_{\mathrm{sub}}$ was controlled by a thermocouple which was spot-welded next to the sample on top of the tantalum foil that covered the heater.

After the deposition, the crystallographic texture of the films was checked by X-ray diffractometry. These measurements were done by Christoph Sürgers. Details of the full procedure are described in reference [33, chapter 4.1.2.]. Here we want to restrict the analysis of the X-ray diffractometry data to the $\Theta - 2\Theta$ scan. The X-ray photons

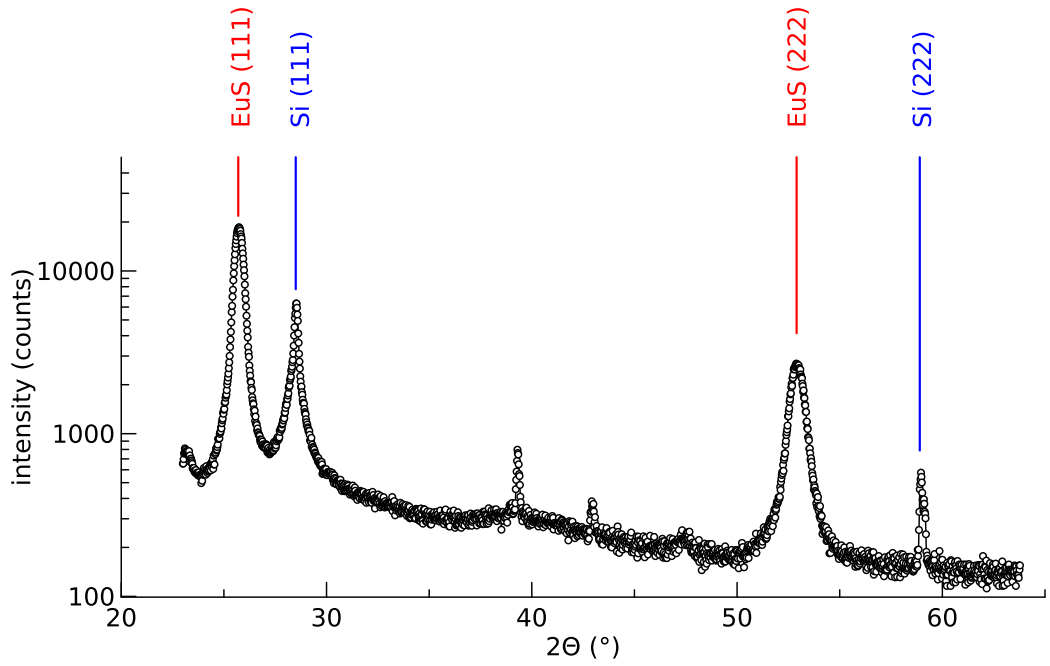


**Figure 3.3:** X-ray diffractometry data of the film EUS10-H. The intensity counts are plotted as a function of twice the scattering angel 2Θ.

were generated from the Cu-$K_\alpha$ line with a wavelength $\lambda = 1.54$ Å. Both sample and detector were rotated separately. An intensity peak occurs at the detector, if Bragg's law

$$2d_{\mathrm{hkl}} \sin(\Theta) = n\lambda \qquad \text{with } n \in \mathbb{N} \tag{32}$$

is fulfilled. Here, $d_{\mathrm{hkl}}$ is the distance of the crystal planes in direction (hkl) and Θ is the incidence angle between the X-ray beam and the plane of the sample. As in rotating the sample also the reflection angle of the beam changes, the detector angle has to be rotated simultaneously by 2Θ (which is the actual angle between the incident and the reflected beam). Figure 3.3 shows a $\Theta - 2\Theta$ scan that was done for the film EuS10-H. The intensity of the diffracted photons is plotted as a function of the detector angle 2Θ. Two kinds of Bragg reflections are found, they are marked by the colored lines. The blue lines indicate the peaks of the substrate Si(111) and Si(222), while the red lines indicate the peaks of the film EuS(111) and EuS(222). The additional peaks in Figure 3.3 which are not marked are most probably substrate peaks. They arise due to scattering of higher order as the sample is slightly tilted to suppress the strong Si(111) substrate peak [74]. Altogether, the X-ray diffraction data demonstrate high (111)-texture of the EuS films which implies that the films are of suitable quality for our purposes.

Furthermore, the magnetic properties of the EuS films were investigated before superconducting nanostructures were fabricated on top of them. For this purpose $5 \times 5$ mm$^2$ sized pieces of the EuS films were installed in a *SQUID* magnetometer (MPMS®from

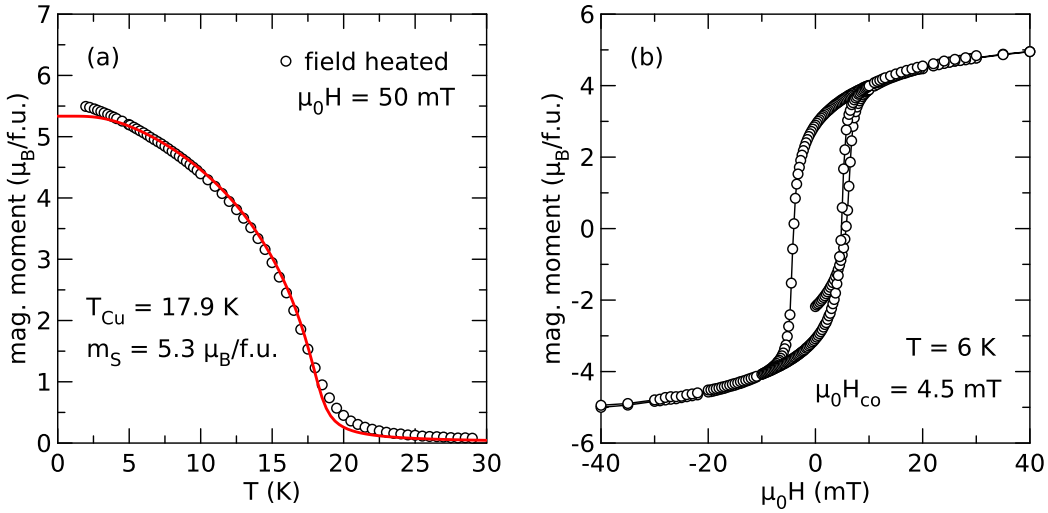


**Figure 3.4:** Magnetic properties of the film EuS10-H. (a) Magnetization measured as a function of the temperature $T$ while heating the sample in an applied field $\mu_0 H = 50$ mT. (b) Hysteresis curve measured at $T = 6$ K.

| film | $T_{\mathrm{sub}}$(°C) | $\mu_0 H_{\mathrm{co}}$(mT) | $T_{\mathrm{Cu}}$(K) |
|---|---|---|---|
| Eus10-G | 700 | 3.5 | 17.7 |
| EuS10-H | 830 | 4.5 | 17.9 |
| EuS10-I | 790 | 2.9 | 18.2 |

**Table 3.1:** Overview of the properties of the europium sulfide films fabricated for this work: Estimated substrate temperature during the evaporation $T_{\mathrm{sub}}$, coercive field $\mu_0 H_{\mathrm{co}}$ and Curie temperature $T_{\mathrm{Cu}}$.

Quantum Design, Inc.) so that the direction of the magnetic field was oriented in the plane of the film parallel to one of its edges. The *SQUID* measurements were done by Gerda Fischer at the "Physikalisches Institut".

Figure 3.4(a) shows the temperature dependence of the magnetization of film EuS10-H. The sample was first magnetized in the field $\mu_0 H = 50$ mT and then heated up while the field was kept constant. The data are fitted (solid red line) to the mean field model, equation (4), to extract the magnetic properties. For this sample the saturation magnetization $m_{\mathrm{S}} = 5.3 \mu_{\mathrm{B}}$/f.u. and the Curie temperature $T_{\mathrm{Cu}} = 17.9$ K are found. The values for the other prepared films are listed in Table 3.1. One observes that for all prepared films, the Curie temperature was slightly above the literature value $T_{\mathrm{Cu,lit}} = 16.5$ K [75]. Altogether, the magnetic properties of the films slightly vary compared to that one which were found by Michael Wolf [33, chapter 4.1.3.]. Probably, this is induced by small, unavoidable modifications of the sample holder that changed the evaporation conditions to which the magnetic properties of the EuS films are highly sensitive as mentioned above.

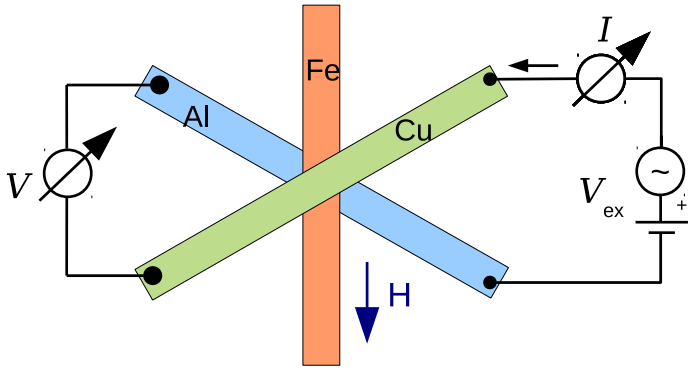


**Figure 3.5:** Sketch of the measurement scheme for the differential conductance measurements.

In Figure 3.4(b) a hysteresis curve of the magnetization which was measured at $T = 6$ K is shown. From the data one can extract the coercive field of the film $\mu_0 H_{\mathrm{co}} = 4.5$ mT. Similar coercive field were found also for the other films (Table 3.1).

## 3.3 Measurement methods

All measurements were done in a commercial $^3$He/$^4$He dilution refrigerator at base temperatures $T_0 = 50 - 500$ mK. The samples were fixed on a sample holder which was mounted in a shielded box that was thermally anchored to the mixing chamber of the dilution refrigerator. During the measurements the samples were placed in the center of a superconducting magnet which reaches magnetic fields $\mu_0 H$ up to 12 T. They were oriented in such a way that the magnetic field was always in-plane to the aluminum wire and mostly in parallel to the iron wire. Throughout this work the exact orientation of the field $H$ is indicated by an arrow whenever a measurement scheme is shown. The samples were contacted by eight measurement lines, consisting of twisted steel coax cables. To reduce the thermal noise as far as possible the measurement lines were fed through various filters at different temperature stages.

To characterize the tunnel junctions measurements of the differential conductance were done. Therefore low-frequency ($f = \omega/2\pi \approx 138Hz$) lock-in technique was used. The appropriate measurement scheme is sketched in Figure 3.5 for the example of the six-pole junction $\alpha$ of sample FIS1.

Across the tunnel junction a voltage excitation $V_{\mathrm{ex}}$ is applied consisting of a dc-part $|V_{\mathrm{dc}}| < 1$ mV and a small ac-part $V_{\mathrm{ac}} \approx 9\mu V$. The operation point is set by the dc-bias which is generated by a battery-powered voltage-divider circuit and set by a motor-controlled potentiometer. The superimposed ac-voltage is provided by a lock-in amplifier that is galvanically separated by a transformer. The ac-part of the resulting current $I$ is detected in the first harmonic of the lock-in amplifier. By a second lock-in amplifier also the first harmonic of the voltage $V$ across the junction is detected to ensure a four-probe measurement. From both quantities the differential conductance $g = dI/dV$ is inferred.

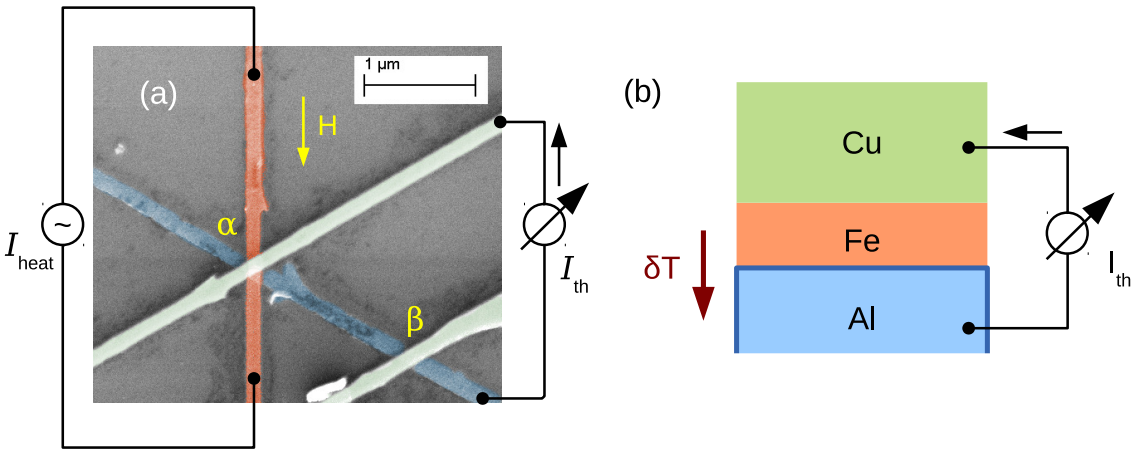


**Figure 3.6:** Sketch of the measurement scheme for the thermoelectric current measurements. (a) Colorized scanning electron microscopy image of junction $\alpha$ of sample EUS1 with the circuit diagram for the thermoelectric measurements. The heater current $I_{\text{heat}}$ is applied to the iron wire, while the resulting thermoelectric current $I_{\text{th}}$ is measured between the superconductor and an additional contact lead. (b) Schematic cross section of junction $\alpha$. The red arrow indicates the direction of the temperature gradient, pointing from the ferromagnet into the superconductor.

The thermoelectric currents were detected with a different measurement technique. In Figure 3.6(a) the measurement scheme is drawn in the SEM image of junction $\alpha$ of sample FIS1. The measurements were done in the following way. An ac-current excitation $I_{\text{heat}} = I_{ac}\sin(\omega t)$, provided by a lock-in amplifier, was applied to the iron wire to heat the contact. The heating current generated a heating power which created a thermal excitation $\delta T$ across the contact. The heating power follows

$$\begin{aligned} P_{\text{heat}} &\propto R_{\text{heat}} * I_{\text{ac}}^2 * \sin(\omega t)^2 \\ &\propto R_{\text{heat}} * I_{\text{ac}}^2 * \frac{1}{2}[1-\cos(2\omega t)] \\ &\propto P_{\text{eff}} * [1-\cos(2\omega t)]. \end{aligned} \tag{33}$$

So, the heating power itself and the resulting thermal excitation $\delta T$ are proportional to the second harmonic of the excitation frequency $\omega$ and the thermoelectric current $I_{\text{th}}$ generated by $\delta T$ can be detected in the second harmonic with the lock-in amplifier. As indicated in Figure 3.6(a), $I_{\text{th}}$ is measured between the superconductor and one of the normal metal leads of the contact. Thereby, current which flows from the ferromagnet into the superconductor is measured with a positive sign as indicated by the black arrow.

To illustrate where the heat difference across the contact is generated Figure 3.6(b) shows a schematic cross section of junction $\alpha$. By heating the iron wire a temperature difference $\delta T$ is generated between the Al and the Fe as indicated by the red arrow. The resulting current $I_{\text{th}}$ which flows across the junction is detected by using one of the aluminum leads and one of the copper leads.

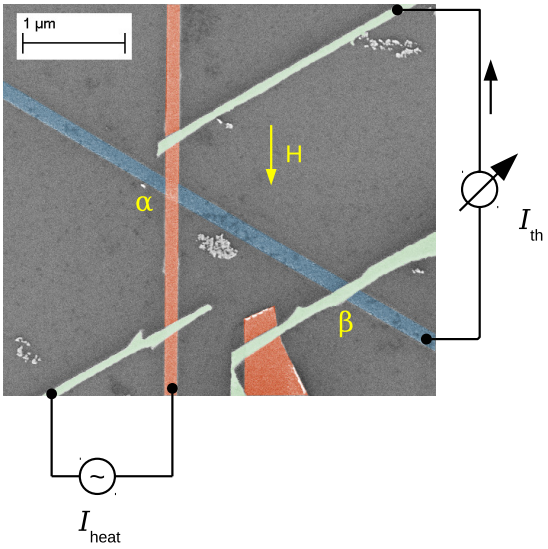


**Figure 3.7:** Colorized SEM image of sample FIS2 together with the circuit diagram for the thermoelectric measurements. The aluminum wire is given in blue, the iron wires in red and the copper wires in light green.

To avoid passing the heater current across the junction $\alpha$ one of the samples (FIS2) was fabricated with a modified layout. In Figure 3.7 a colorized scanning electron microscope image of FIS2 is shown together with a scheme of the appropriate measurement circuit. The copper wire (green) of contact $\alpha$ is split into two leads which both are only in contact with the iron wire, so that contact $\alpha$ is a pure FIS junction. As depicted, the heating of the ferromagnetic part of the tunnel junction happened indirectly here as the heater current $I_{\mathrm{heat}}$ was passed through one half of the iron wire and the attached copper lead. The resulting thermoelectric current $I_{\mathrm{th}}$ was measured between the aluminum wire and the copper lead on the other side of the contact. Note that in this configuration both circuits are completely separated.

# 4 Thermoelectric effect in FIS junctions on top of $SiO_2$

In this chapter the measurements of thermoelectric currents in ferromagnet/superconductor tunnel junctions are presented and discussed. First, differential conductance measurements of the ferromagnetic contact are shown. These serve for the characterization and the establishment of the junction parameters. Furthermore, conductance measurements were used for the calibration of the electronic temperatures of the ferromagnet and the superconductor while current was applied to heat the iron wire. Then, the actual measurements of the thermoelectric current are presented and compared to theoretical predictions. From the thermoelectric currents the thermoelectric coefficient $\eta$ and the Seebeck coefficient $S$ are inferred and compared for all samples. Finally, various control experiments are presented which were done to verify the experimental data.

## 4.1 Sample details and characterization measurements

First, some preliminary notes about the sample denomination should be given. Altogether the thermoelectric measurements were done on five different samples. Four of them had a superconductor-ferromagnet tunnel junction, they are denominated in the following as samples FIS1-4. For one sample the ferromagnetic wire was replaced by a normal metal one, this sample is denominated as NIS. The main results of this chapter are already presented in reference [76], based on measurements done for the samples FIS1,FIS2 and NIS. To maintain consistency these sample names are kept for this thesis. However, it should be mentioned that the samples FIS3 and FIS4 were measured at an earlier stage than the above mentioned samples. Hence, the whole measurement and data analysis procedure was not yet optimized for FIS3 and FIS4. Both samples had a slightly changed sample design as the 6-pole junction $\alpha$ was formed by a thinner copper wire with thickness $t_{\mathrm{Cu}} = 20$ nm compared to the later measured samples. Also the junction $\beta$ was formed by a second FIS junction instead of a NIS junction. During the data evaluation we found out that self-heating effects occurred due to the measurement itself which made the calibration of the heating more difficult. To prevent this, we changed the sample design to the ones which were described in the preceding chapter. Furthermore, the calibration measurements were done at zero magnetic field $\mu_0 H = 0$ for the samples FIS3 and FIS4. In this field the coherence peaks are found to be sharpened due to the way the differential conductance was measured (for details see reference [33, chapter 3.2.3.]). Hence the fits of the conductance curves which are used to evaluate the electronic temperatures are not as accurate as they are in high magnetic fields. The fit area had to be restricted to the sub-gap regime $e|V| \lesssim \Delta$ and the inner tails of the coherence peaks, to achieve acceptable results. Unfortunately, in this way it is difficult to extract the pair potential $\Delta$ which is required for estimating the electronic temperature $T_{\mathrm{S}}$ of the superconductor as we will see later. Thus, it was also not possible to check the heating of S for the samples FIS3 and FIS4 sufficiently.

Therefore, mostly the results of the samples FIS1, FIS2 and NIS are shown in this chapter. They are complemented by data of the samples FIS3 for one of the control measurements, the switching of the thermoelectric measurement configuration. Sample FIS4 is mentioned for completeness as it also showed a thermoelectric effect, but did not enable a proper data analysis which is essential for a reasonable comparison of the experimental results to the theory. Detailed information about all samples and the exact measurement periods are listed in Table A.1 in the appendix.

To characterize the junction $\alpha$ the differential conductance $g = dI/dV$ was measured as a function of the voltage $V$ as described in the previous chapter (see Figure 3.5 and description in the text). Figure 4.1(a) shows $g$ as a function of $V$ for sample FIS1. Here conductance curves are presented at different magnetic fields $\mu_0 H$ for the base temperature $T_0 = 50$ mK. In small fields, for example $\mu_0 H = 0.5$ T, the conductance vanishes for small voltages and has pronounced coherence peaks at the gap voltages $|V| = \Delta/e$ as it is expected from BCS theory for a high quality tunnel junction. In increasing fields the form of the conductance curve changes. The spin splitting of the quasiparticle density of state is visible as the coherence peaks split up into two subpeaks. In addition, the magnetic field also generates a pair breaking effect which leads to a broadening of the conductance curves in higher fields as it was described in section 2.3. Note that at $\mu_0 H = 1$ T the energy gap is already closed and quasiparticle states exist for $V = 0$ ($E = 0$), though the superconductivity is not completely suppressed at this field. This phenomenon is called "gap-less superconductivity" and emphasizes the importance of the distinction between the energy gap $E_G$ and the pair potential $\Delta$.

In Figure 4.1(a) fits which were done according to equation (27) are indicated as solid lines. They are found to be in good agreement with the measured data. Here the order of the fit procedure was as follows. First, the conductance curves measured in high magnetic field were fitted to extract the polarization of the junction. The values found for all ferromagnetic samples were in the range $P \approx 0.06 - 0.08$, which is reasonable for junctions with an ultra-thin aluminum oxide tunnel barrier [77]. Due to the small value of $P$ the asymmetry in the heights of the inner conductance peaks is hardly visible here. The spin-orbit scattering strength $b_{so}$ was adjusted to an appropriate value, also in high magnetic fields. As the fits were not sensitive enough to $b_{so}$, values of the order $b_{so} \sim O(0.01)$ were chosen which are in reasonable agreement with literature values reported for thin aluminum films [53]. Afterwards $P$ and $b_{so}$ were kept fixed and the conductance curves in smaller fields were fitted to extract the pair potential $\Delta$, the pair breaking parameter $\Gamma$ and the effective spin-splitting $B_{eff}$ as a function of the magnetic field $\mu_0 H$.

In Figure 4.1(b) the effective spin-splitting $B_{eff}$ normalized to the critical field $H_c$ is shown as a function of the applied field $H$ also normalized to $H_c$. A dashed line marks the expected value $B_{eff} = \mu_0 H$ which is equivalent to the Zeeman splitting induced by the applied field. The fit values for $B_{eff}$ follow this line in small fields for all samples, but show a deviation when $H$ approaches $H_c$ as they have reduced values there. The origin of this reduction lies in Fermi-liquid renormalization effects which result from

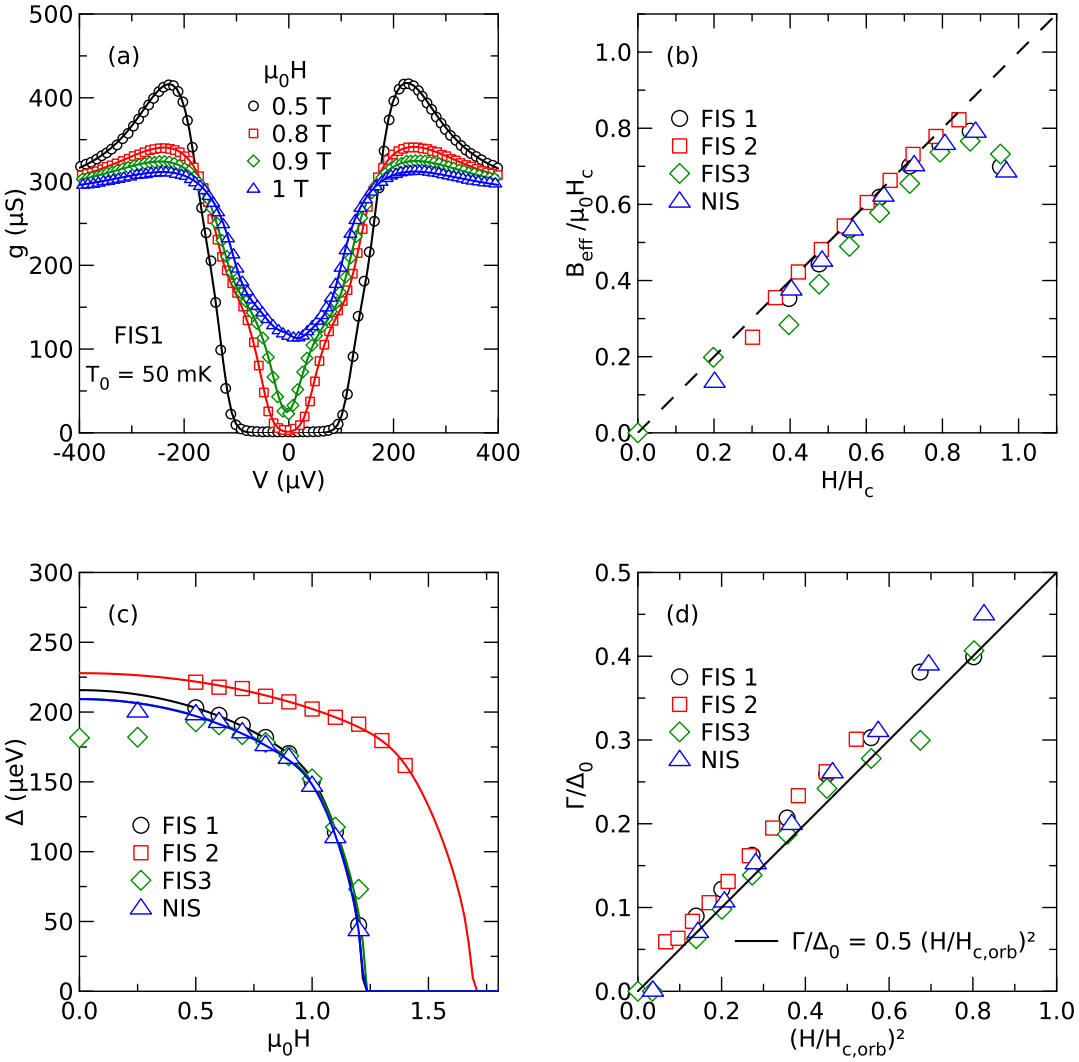


**Figure 4.1:** (a) Differential conductance $g$ of junction $\alpha$ as a function of the applied injector bias $V$ for different magnetic fields $\mu_0 H$. The data stem from sample FIS1. Panels (b) - (d) fit parameter for all four samples. (b) Effective spin-splitting field $B_{\mathrm{eff}}$ normalized to the critical field $H_{\mathrm{c}}$ as a function of $H/H_{\mathrm{c}}$. The dashed line marks $B_{\mathrm{eff}} = \mu_0 H$. (c) Pair potential $\Delta$ as a function of $\mu_0 H$ together with fits according to the self-consistency relation. (d) Normalized pair breaking parameter $\Gamma/\Delta_0$ as a function of $(H/H_{\mathrm{c,orb}})^2$ for all samples.

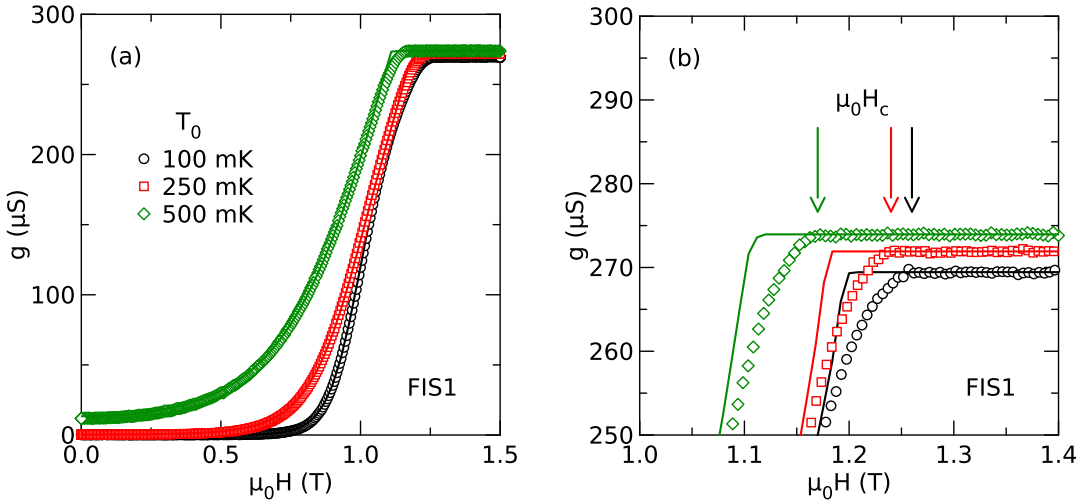


**Figure 4.2:** (a) Zero-bias conductance $g(V = 0)$ of junction $\alpha$ as a function of the magnetic field $\mu_0 H$ at bias $V = 0$ for different base temperatures $T_0$. The data in panels (a) and (d) stem from sample FIS1. (b) Magnification of panel (a) for the field regime near to the critical field. The arrows mark the values $\mu_0 H_c$ which are read from the zero bias conductance curve.

the interaction of the quasiparticles among each other. In the normal state of aluminum the effective spin-splitting field is

$$B_{\text{eff}} = \frac{\mu_0 H}{1 + G_0} \tag{34}$$

with the Fermi-liquid renormalization parameter $G_0 = 0.3$ [78, 79], so that the spin-splitting is reduced by the interaction. In the superconducting state the strength of the renormalization depends on the number of thermally excited quasiparticles. Near the critical field where many quasiparticles are excited a renormalization is found and the spin splitting is lowered. Contrary in small field where the quasiparticle states are not excited, no influence of Fermi-liquid effects is visible. A theory model which includes Fermi-liquid effects for describing superconductivity especially in high magnetic fields was developed by Alexander et al. [78]. This model will be used throughout this work for calculating $\Delta(T_S, H)$ and $B_{\text{eff}}(T_S, H)$ self-consistently for the fits of the field-dependent quantities later on.

In Figure 4.1(c) the pair potential $\Delta$ is plotted as a function of the magnetic field $\mu_0 H$ for all four samples. The solid lines show self-consistent fits for which Fermi-liquid renormalization was also included. From these fits we could extract the pair potential $\Delta_0 = \Delta(T = 0, H = 0)$ in zero field and at zero temperature and the orbital critical magnet field $H_{c,\text{orb}}$ which is the critical field in the absence of spin splitting.

In Figure 4.1(d) the pair breaking parameter $\Gamma$ normalized to $\Delta_0$ is plotted as a function of $(H/H_{c,\text{orb}})^2$ for all four samples. The solid line shows the theory model for the pair

| Sample | $G_T$ ($\mu$S) | $P$ | $b_{so}$ | $T_c$ (K) | $\mu_0 H_c$ (T) | $\Delta_0$ ($\mu$eV) | $\mu_0 H_{c,orb}$ (T) |
|---|---|---|---|---|---|---|---|
| FIS1 | 270 | 0.08 | 0.015 | 1.48 | 1.26 | 208 | 1.3 |
| FIS2 | 155 | 0.08 | 0.015 | 1.53 | 1.65 | 195 | 2.03 |
| FIS3 | 608 | 0.06 | 0.005 | 1.48 | 1.26 | 209 | 1.35 |
| NIS | 315 | - | 0.01 | 1.47 | 1.24 | 199 | 1.33 |

**Table 4.1:** Overview of the sample properties. Normal-state tunnel conductance $G_T$ and polarization $P$ of the junction $\alpha$, spin-orbit scattering strength $b_{so}$. Properties of the Aluminum wire: critical temperature $T_c$, critical magnetic field $\mu_0 H_c$, pair potential $\Delta_0$ and orbital critical field $\mu_0 H_{c,orb}$.

breaking in a thin film [55]:

$$\frac{\Gamma}{\Delta_0} = \frac{1}{2}\left(\frac{H}{H_{c,orb}}\right)^2 . \tag{35}$$

We see that for all samples $\Gamma$ follows the theoretic prediction which confirms the good quality of the fits. For the fits of field dependent quantities we will parametrize the pair breaking by $\Delta_0$ and $(H/H_{c,orb})^2$ and model it by equation (35).

Figure 4.2(a) shows the differential conductance at zero-bias $V = 0$ as a function of the applied magnetic field for three different base temperatures $T_0$. In small fields $g$ vanishes due to the freeze-out of the quasiparticle conductance. It starts to increase in higher fields once the energy gap is small enough. Above the critical field $\mu_0 H_c$ the normal tunneling conductance $G_T$ is reached and the conductance stays constant. For higher base temperatures the thermal broadening of the conductance is visible and the conductance is also non-vanishing in small fields. Modeling the data with equation (27) gave a second set of junction parameters. Here, the free parameters were the normal-state junction conductance $G_T$, the pair potential $\Delta_0$ in zero field and at zero temperature, the orbital critical field $\mu_0 H_{c,orb}$ and the electronic temperature $T = T_F = T_S$. The pair-breaking $\Gamma(H)$ was included by equation (35). To achieve better accordance between data and fits in small fields, a phenomenological life-time broadening parameter $\Gamma_{LT}$ (the so-called Dynes parameter [80]), was included. This is done by adding a small imaginary part to the energy, so that $\varepsilon \to \varepsilon + i\Gamma_{LT}$ in equation (22). Typically, small values $\Gamma_{LT} \approx 10^{-4}\Delta_0$ were found.

In table 4.1 the characteristic sample parameters are listed. The values for the spin-polarization $P$ and the spin orbit scattering strength $b_{so}$ were taken from the fits of the conductance curves $g(V)$, while the values for $G_T$, $\Delta_0$ and $\mu_0 H_{c,orb}$ were taken from the fits of the zero-bias conductance $g(H, V = 0)$ for $T_0 = 100$ mK. For the critical field $\mu_0 H_c$, the value was read from the zero-bias conductance curve where the conductance reaches the normal conducting value. These values are marked in Figure 4.2 (b) by the arrows for different base temperatures $T_0$, in Table 4.1 the value extracted for $T_0 = 100$ mK is listed for the different samples. In the same way, the

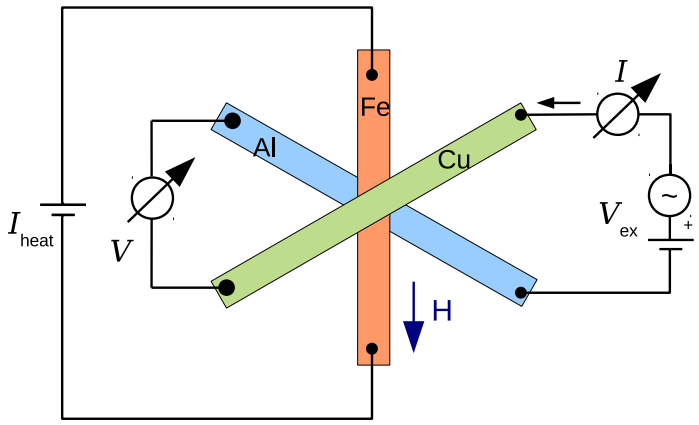


**Figure 4.3:** Scheme of the measurement configuration which was used to calibrate the electronic temperature of the ferromagnet against the applied dc-heater current $I_{\mathrm{heat}}$.

critical temperature $T_{\mathrm{c}}$ was read from the cooling curve $g(T)$ of the junction in zero-field.

## 4.2 Calibration of the temperature difference

In the following, the calibration of the electronic temperatures $T_{\mathrm{F}}$ of the ferromagnet and $T_{\mathrm{S}}$ of the superconductor as a function of the applied heater current is described. This step was necessary to determine the thermal excitation $\delta T = T_{\mathrm{F}} - T_{\mathrm{S}}$ across the tunnel junction which is created by a certain heater current flowing through the iron wire.

In Figure 4.3 the appropriate measurement scheme for this purpose is shown. Again the differential conductance $g$ of the junction is measured while this time an additional dc-heater current $I_{\mathrm{heat}}$ is applied to the ferromagnetic wire. Therefore, dc-current was generated in a second circuit by the voltage of a battery and set by a motor-controlled potentiometer.

Figure 4.4(a) shows the result of the calibration measurements. The differential conductance $g$ is plotted as a function of the voltage $V$ for different dc-heater currents $I_{\mathrm{heat}}$. Here, data of sample FIS1 measured at base temperature $T_0 = 100$ mK are shown. The magnetic field $\mu_0 H = 1$ T was chosen because at this field the thermoelectric current reached its maximum value as we will see later. As expected, one observes an increase of the thermal broadening of the conductance curves for higher heater currents $I_{\mathrm{heat}}$. This is reflected by the smoothing of the coherence peaks at the gap voltage and by the increase of the conductance at zero bias $V = 0$. By fitting the thermal broadening the electronic temperature $T_{\mathrm{F}}$ of the ferromagnet could be extracted. Initially, the conductance curve for $I_{\mathrm{heat}} = 0$ was fitted by equation (27) to extract the characteristic junction parameters. Then, these parameters were fixed, except for $T_{\mathrm{F}}$ which was left free and adjusted for every single curve.

The result of the calibration measurement is shown in Figure 4.4(b). Here, the electronic temperature $T_{\mathrm{F}}$ is plotted as a function of $I_{\mathrm{heat}}$ for different base temperatures $T_0$. To

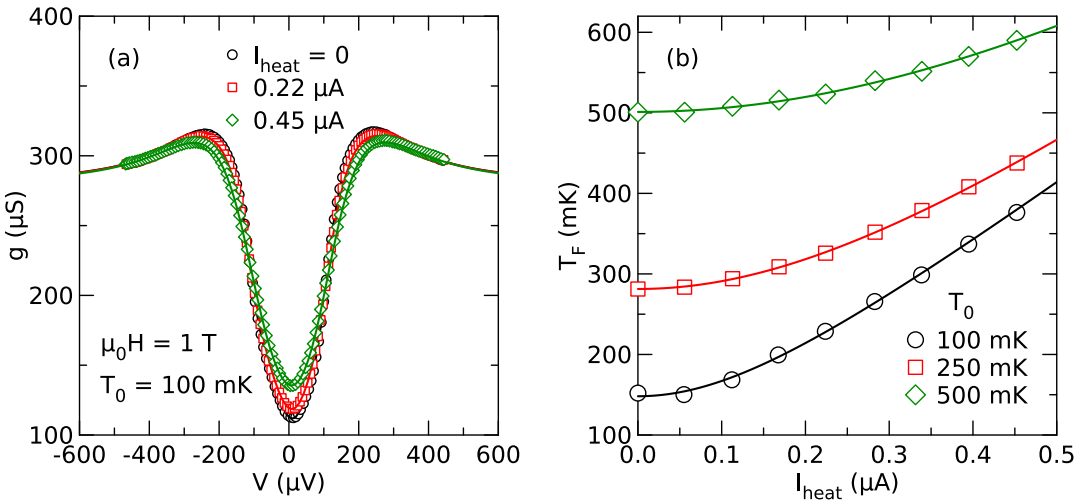


**Figure 4.4:** Calibration of the electronic temperature $T_\mathrm{F}$ of the ferromagnet. (a) Differential conductance $g$ as a function of voltage $V$ for different heater currents $I_\mathrm{heat}$. (b) Electronic temperature $T_\mathrm{F}$ as a function of the heater current $I_\mathrm{heat}$ for different base temperatures $T_0$.

describe the heating, the model of a mesoscopic wire in quasi-equilibrium with negligible electron-phonon scattering was used. This is appropriate for a metallic wire with a length of a few $\mu$m at sub-Kelvin temperatures [29]. Within this model the electronic temperatures in the middle of the wire is given by

$$T_\mathrm{F} = \sqrt{T^2 + \frac{R_\mathrm{heat}^2 I_\mathrm{heat}^2}{4L_0}} \tag{36}$$

where $R_\mathrm{heat}$ is the resistance of the heater wire, $L_0 = \pi^2 k_\mathrm{B}^2/3e^2$ is the Lorenz number and $T = T(I_\mathrm{heat} = 0)$ is the electronic temperature in the absence of any heater current. Fits according to equation (36) are plotted in Figure 4.4(b) as solid lines. Good agreement with the data can be observed and we will use the fits for an estimation of the thermal excitation in the thermoelectric experiments later on. For the heater wire resistance the fits yield $R_\mathrm{heat} \approx 230\ \Omega$, a value that is smaller than the 2-probe resistance $R_\mathrm{Fe} = 1350\ \Omega$ of the iron wire. We attribute this to the thick copper wire which lies on top of the ferromagnetic contact and acts as a cooling fin. Note here that the electronic temperature $T = T_\mathrm{F}(I_\mathrm{heat} = 0)$ is slightly increased over the bath temperature $T_0$, especially at low temperatures. The probable reason for this is the incomplete filtering of the thermal noise from higher temperature stages of the cryostat.

So far, possible heating of the superconductor due to the heating of the iron wire was not considered. Since superconductors are poor heat conductors at low temperatures, they can be heated easily. An increase of the electronic temperature of the superconductor $T_\mathrm{S}$ is harder to identify in the conductance curve of a tunnel junction as it affects the conductance only indirectly by reducing slightly the pair potential $\Delta$. To infer $T_\mathrm{S}$ as a function of the heating current $I_\mathrm{heat}$, it is therefore necessary to extract $\Delta(I_\mathrm{heat})$

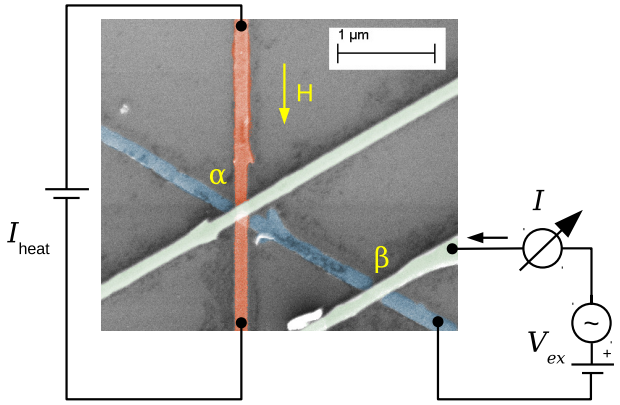


**Figure 4.5:** Measurement configuration which was used to estimate the heating of the superconductor for a dc-heater current $I_{\mathrm{heat}}$ applied to the iron wire. Here the differential conductance of junction $\beta$ is measured.

first. In principle, one could do this by adjusting $\Delta$ as free parameter in the fits of the conductance curves of contact $\alpha$ which were shown above. However, the changes in $\Delta$ are quite small so that they are dominated by the thermal smearing which originates from the temperature increase $\delta T_{\mathrm{F}}$. It is therefore better to separate both effects and to measure the differential conductance at contact $\beta$ while the superconductor is heated indirectly by applying heater current $I_{\mathrm{heat}}$ to the iron wire. The appropriate measurement configuration is sketched in Figure 4.5. As the distance between the contacts $\alpha$ and $\beta$ was $d \approx 1.5$ $\mu$m and earlier experiments done by Arutyunov et al. [81] showed that the length scale for the relaxation of the energy imbalance $\Lambda_{\mathrm{T}*} \approx 40$ $\mu m$ in superconducting aluminum at temperatures $T \ll T_{\mathrm{c}}$, it is reasonable to assume that the temperature $T_{\mathrm{S}}$ of the superconductor is nearly equal at both junctions $\alpha$ and $\beta$.

Figure 4.6 shows the results of the measurements and the following data analysis. Shown here are data of sample FIS2 where the most detailed measurements were done. Figure 4.6(a) shows the differential conductance $g$ of contact $\beta$ as a function of the voltage $V$ for different heater currents $I_{\mathrm{heat}}$. The base temperature here was $T_0 = 100$ mK and the applied field was $\mu_0 H = 1.3$ T where the thermoelectric signal reached its maximum value for sample FIS2 (shown in the following section). The conductance curves measured for zero current $I_{\mathrm{heat}} = 0$ and for moderate current $I_{\mathrm{heat}} = 0.43$ $\mu$A are almost matching in shape what indicates only a small heating of S. For a larger current $I_{\mathrm{heat}} = 2.27$ $\mu$A the energy gap is slightly reduced and moderate broadening of the curve is visible. The broadening of the curves is probably induced by an increase of the phenomenological life-time broadening parameter $\Gamma_{\mathrm{LT}}$ due to the heating of the superconductor [81]. For the quantitative analysis the conductance curves $g(V)$ were fitted by equation (27) again. First the curve for $I_{\mathrm{heat}} = 0$ was used to extract all junction parameters which were then fixed. For the other curves the pair potential $\Delta$ was adjusted as free parameter.

In Figure 4.6(b) the extracted pair potential $\Delta$ is shown as a function of $I_{\mathrm{heat}}$. In the whole range the change in $\Delta$ is only of the order of a few $\mu$eV with considerable scatter on this small scale. To reduce the scatter two adjacent points were averaged for calculating $T_{\mathrm{S}}$. We assumed $\delta T_{\mathrm{S}} = 0$ for $I_{\mathrm{heat}} = 0$ and calculated the pair potential $\Delta(T, H)$ for the first two points. For the other data points the temperature increase

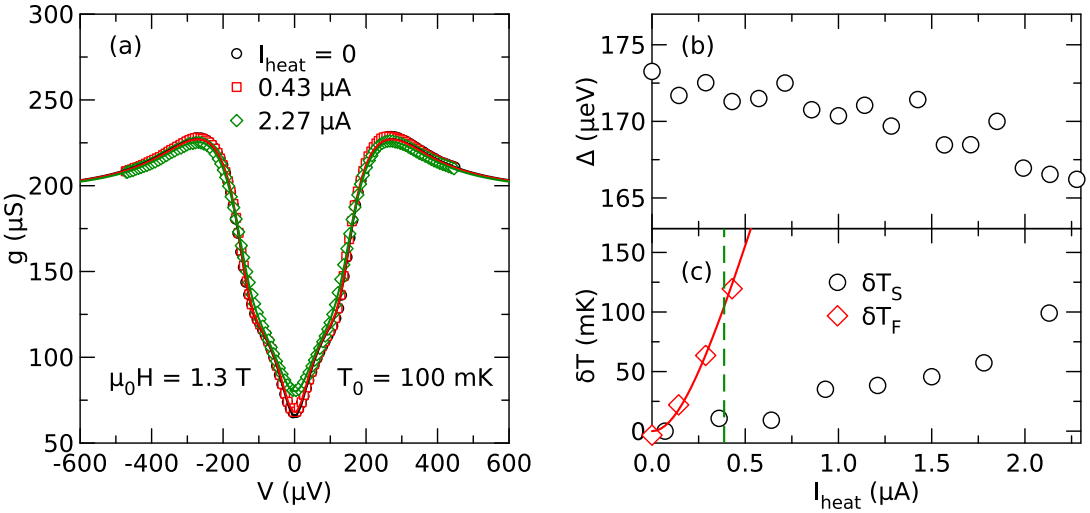


**Figure 4.6:** Calibration of the electronic temperature $T_S$ of the superconductor. (a) Differential conductance $g$ of junction $\beta$ as a function of the voltage $V$ for different heater currents $I_{heat}$. (b) Pair potential $\Delta$ as a function of the heater current $I_{heat}$ extracted by fits of the conductance shown in (a). (c) Increase $\delta T_S$ of the temperature of the superconductor as a function of the heater current $I_{heat}$ extracted by inverting $\Delta(T_S)$, together with $\delta T_F$.

$\delta T_S = T_S - T$ was extracted by the inversion of the self-consistency relation $\Delta(T + \delta T_S, H)$.

The resulting temperature increase $\delta T_S$ is shown in Figure 4.6(c) as a function of $I_{heat}$. For comparison, also the increase $\delta T_F$ of the electronic temperature of the ferromagnet, which was extracted at junction $\alpha$ before, is drawn here. We see that the temperature increase of the ferromagnet is larger than that of the superconductor, so that a temperature difference can be generated across the tunnel junction depending on $I_{heat}$. For clarification a dashed line marks the thermal bias $\delta T_F \approx 100$ mK which was usually used in the following thermoelectric experiments. At this value one observes a temperature increase $\delta T_S \lesssim 20$ mK of the superconductor. Hence, most of the thermal bias drops across the ferromagnetic tunnel junction under this condition.

## 4.3 Thermoelectric measurements

After extracting the junction properties and calibrating the thermal excitation, all requirements were fulfilled to measure the thermoelectric effect and to compare it to the theory model. The measurements were done by second harmonic detection technique in the configuration presented in Figure 3.6 for the samples FIS1, FIS3 and NIS, and Figure 3.7 for sample FIS2 respectively. The heater current $I_{heat}$ was adjusted with the help of the calibration curves so that a thermal excitation of $\delta T \approx 100$ mK was generated across the tunnel junction.

### 4.3.1 Thermoelectric current

Figure 4.7 shows the thermoelectric current $I_{\mathrm{th}}$ as a function of the magnetic field $\mu_0 H$ at different base temperature $T_0$. In panels (a),(c) and (e) data from sample FIS1 are shown, in panels (b),(d) and (f) data from sample FIS2. First of all, we want to discuss the data for $T_0 = 100$ mK in Figure 4.7(a) and Figure 4.7(b). The shape of both curves is similar. The current is vanishing in small magnetic fields and starts to rise in the field regime where the Zeeman splitting of the quasiparticle density of states occurs. With increasing fields the energy gap in the superconductor is reduced due to the rising Zeeman splitting and $I_{\mathrm{th}}$ increases further. In the field where the energy gap completely vanishes the thermoelectric current exhibits a maximum. For further increasing fields the inner spin-split bands of the DOS overlap and the current shrinks again until it vanishes completely once the critical field is reached. This behavior is observed for both samples but with a differing field range due to the different critical fields both samples had. For higher base temperature the signal keeps its shape but thermal broadening of the current is observable and the maximum value of the current shifts to a smaller field.

For modeling the current equation (27) was used together with the necessary junction parameter extracted so far. We observed that the junction parameter set derived from the fits of the zero-bias conductance $g(V = 0, H)$ gave better results than the parameter set derived from the conductance curves $g(V)$, so that we chose to use the first one here. These are the same parameters which are listed in table 4.1. Again, the pair potential $\Delta(T_{\mathrm{S}}, H)$ and the effective spin-splitting field $B_{\mathrm{eff}}(T_{\mathrm{S}}, H)$ were calculated self-consistently by the model of reference [78], so that Fermi-liquid renormalization effects are included. As the ferromagnet was heated by an ac-heater current $I_{\mathrm{heat}} = I_{\mathrm{ac}} \sin(\omega t)$ according to the heating model, equation (36), the electronic temperature of the ferromagnet was $T_{\mathrm{F}} = \sqrt{T^2 + \delta T^2 \sin(\omega t)^2}$ with $\delta T = I_{\mathrm{ac}} R_{\mathrm{heat}} / 4 L_0$ throughout the measurements. The nonlinearity of this relation was considered by modeling $I(t) = I(\delta T(t))$ and extracting the second harmonic by discrete Fourier analysis [82].

Now we can compare our results to the theoretical prediction. In Figure 4.7 three theoretical calculations are plotted in each panel which are differing only by the assumptions for the thermal excitation $\delta T$. First of all, the red dashed lines show calculations of $I_{\mathrm{th}}$ under the assumption that only the iron wire is heated by the heater current, so that $\delta T = \delta T_{\mathrm{F}}$. The calculated currents have the same shape as the data, but they overestimate the signal slightly. The green dash-dotted lines show the expected currents when heating of the superconductor is also regarded, so that the thermal excitation is $\delta T = \delta T_{\mathrm{F}} - \delta T_{\mathrm{S}}$ here. Under this assumption the data are usually underestimated a bit. Finally the blue solid lines show fits to the data with the thermal excitation as free fit parameter $\delta T = \delta T_{\mathrm{fit}}$. They show excellent agreement with the data and it is remarkable that the thermoelectric current can be described within the theory model by fit curves with only one free fit parameter.

For comparison the values for $\delta T_{\mathrm{fit}}$ are listed in table 4.2 for all samples and base

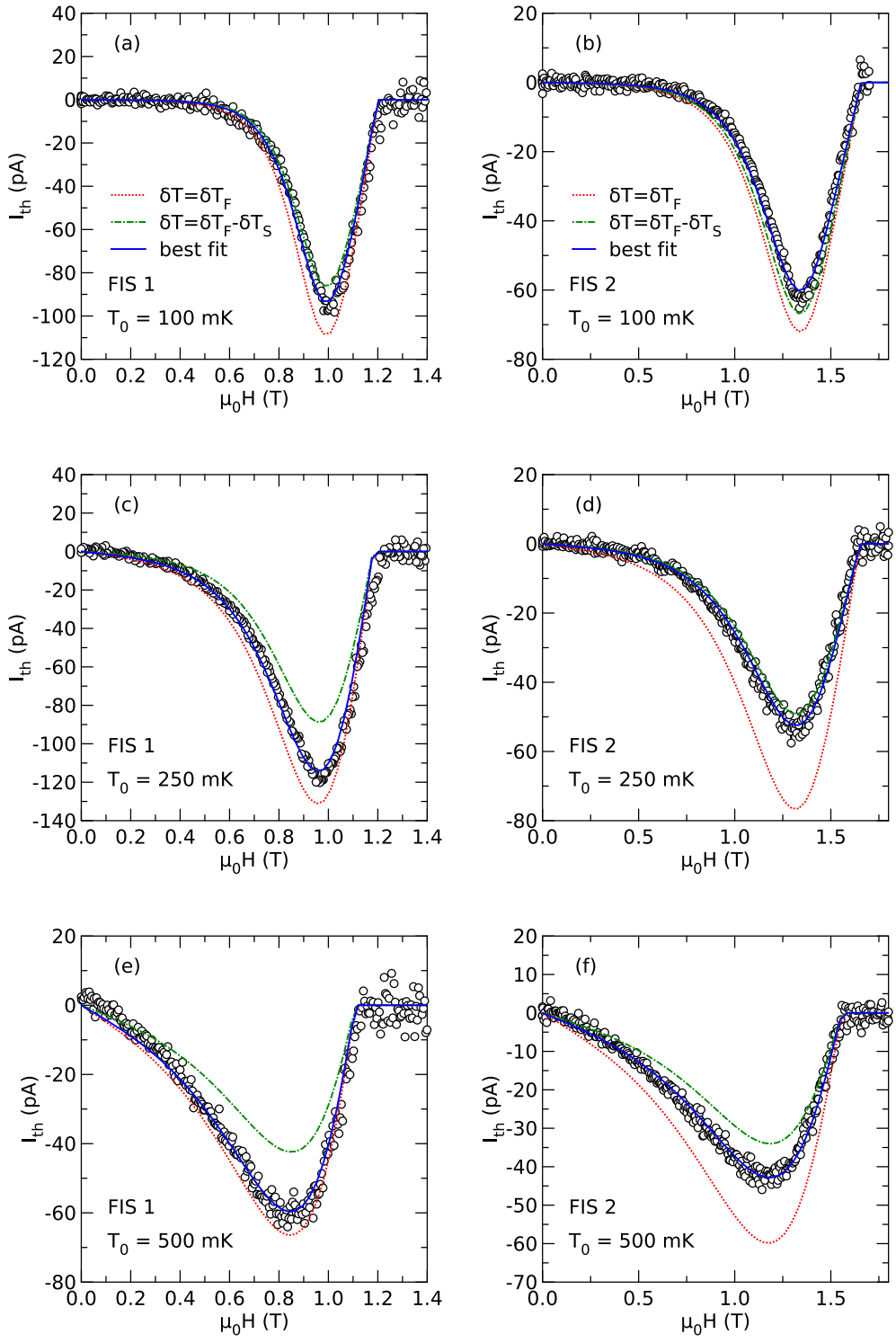


**Figure 4.7:** Thermoelectric current $I_{\mathrm{th}}$ as a function of the magnetic field $\mu_0 H$ for different base temperatures $T_0$ together with theoretical calculations. The data of panels (a),(c) and (e) stem from sample FIS1, the data in (b),(d) and (f) from FIS2.

| sample | $T_0$ (mK) | $\delta T_F$ (mK) | $\delta T_F - \delta T_S$ (mK) | $\delta T_{fit}$ (mK) |
|---|---|---|---|---|
| FIS1 | 100 | 100 | 80 | 86 ± 10 |
| FIS1 | 250 | 120 | 82 | 104 ± 19 |
| FIS1 | 500 | 80 | 50 | 72 ± 15 |
| FIS2 | 100 | 100 | 93 | 84 ± 8 |
| FIS2 | 250 | 100 | 64 | 68 ± 18 |
| FIS2 | 500 | 90 | 50 | 63 ± 20 |
| FIS3 | 100 | 135 | - | 87 ± 48 |
| FIS3 | 250 | 90 | - | 58 ± 32 |
| FIS3 | 500 | 42 | - | 30 ± 12 |

**Table 4.2:** Overview of the different assumptions for the heating excitations described in the text.

temperatures together with the estimated values $\delta T_F$ and $\delta T_F - \delta T_S$. In almost all cases $\delta T_{fit}$ fulfills the relation

$$\delta T_F > \delta T_{fit} > \delta T_F - \delta T_S, \tag{37}$$

so that we assume it to be reasonable. For the calculations of the thermoelectric coefficients which we will show next we will always use $\delta T = \delta T_{fit}$. The errors shown in table 4.2 together with $\delta T_{fit}$ reflect the uncertainty of $\delta T$. As for sample FIS3 the calibration measurements for $T_S$ were unreliable (due to the not yet optimized calibration measurements) the difference $\delta T_{fit} - \delta T_F$ is taken as uncertainty.

### 4.3.2 Thermoelectric coefficients

So far, only raw data of $I_{th}$ were shown. To compare the signal from sample to sample it is helpful to normalize $I_{th}$ to the heater excitation $\delta T$. Following equation (28), one can calculate the thermoelectric coefficient

$$\eta = I_{th} * \frac{\overline{T}}{\delta T} \tag{38}$$

where $\overline{T} = T + \delta T/2$ is the average temperature of the junction. Figure 4.8(a) shows $\eta$ normalized to the junction conductance $G_T$ and the pair potential $\Delta_0$ as a function of the magnetic field $\mu_0 H$ for different base temperatures. As for the calculation of $\eta$ from $I_{th}$ only constant values are used, the shape of $\eta$ is the same as that of $I_{th}$. For higher base temperatures the broadening of the curves as well as the magnitude of $\eta$ increase. We can now compare the coefficient $\eta$ to the theoretic predictions. In reference [21] Ozaeta et al. calculated the coefficient $\alpha = \eta/P$ (the polarization $P$ is a constant for the FIS samples, but $P = 0$ for sample NIS) for different base temperatures (see Fig.2 in [21]). Similar to our observation, they also predicted sharp signals for low temperature, while for higher temperatures they predict broadening and an increase

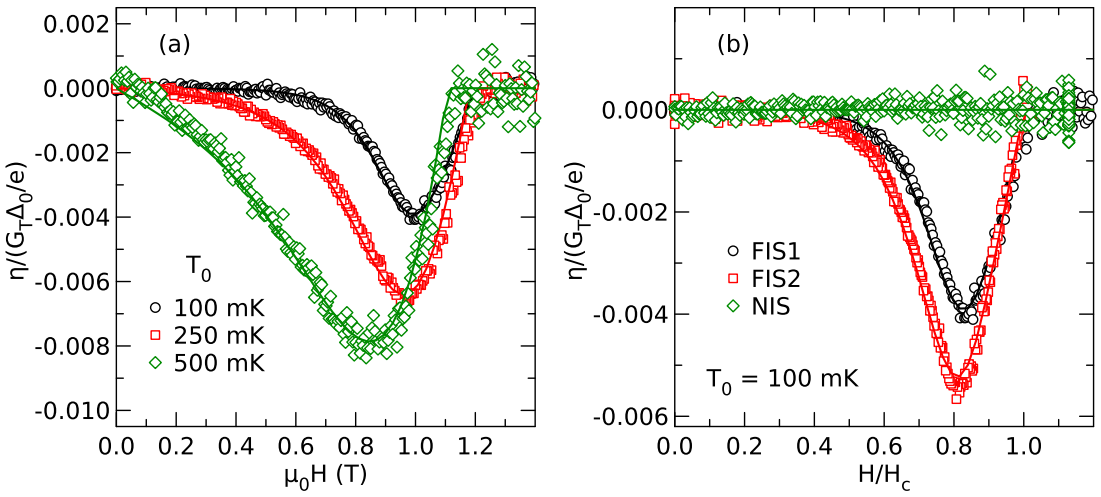


**Figure 4.8:** (a) Thermoelectric coefficient $\eta$ as a function of the magnetic field $\mu_0 H$ for sample FIS1 at different base temperatures $T_0$. (b) Thermoelectric coefficient $\eta$ as a function of the normalized magnetic field $H/H_c$ for sample FIS1,FIS2 and NIS at base temperatures $T_0 = 100$ mK.

of the strength of the coefficient. Hence, also here we observe good agreement between our results and the theory.

In Fig. 4.8(b) $\eta$ is shown for the samples FIS1, FIS2 and NIS as a function of the normalized field $H/H_c$ at $T_0 = 100$ mK. For both ferromagnetic samples $\eta$ exhibits the typical dip shape with a maximum at $H \approx 0.8 H_c$ and both show a thermoelectric effect in the range $0.5 < H/H_c < 1$. In contrast to the ferromagnetic samples, the data of the sample NIS do not show thermoelectric current and thus $\eta = 0$ in the whole field range. To guarantee a sufficient comparability also for sample NIS the whole measurement program was done including all characterization and calibration measurements. The comparison of the three samples directly demonstrates the necessity of the spin-polarization $P$ for the creation of the thermoelectric effect in a superconductor/metal tunnel junction.

From the thermoelectric current, it was possible to infer the Seebeck coefficient $S$. It is given by

$$S = \frac{\eta}{g \cdot \overline{T}} = \frac{I_{\mathrm{th}}}{g \cdot \delta T}. \tag{39}$$

and can be calculated directly from the data of $I_{\mathrm{th}}$ and the zero bias conductance $g(V = 0, H)$. Figure 4.9 shows the Seebeck coefficient $S$ of sample FIS1 as a function of the magnetic field $\mu_0 H$ for different base temperatures $T_0$. The shape of $S$ is similar to that of $\eta$, but it shows a faster increase in small fields and also its maximum value is observed in a smaller field. In contrast to $\eta$, the Seebeck coefficient is larger for smaller base temperature $T_0$. This is induced by the freeze-out of the junction conductance

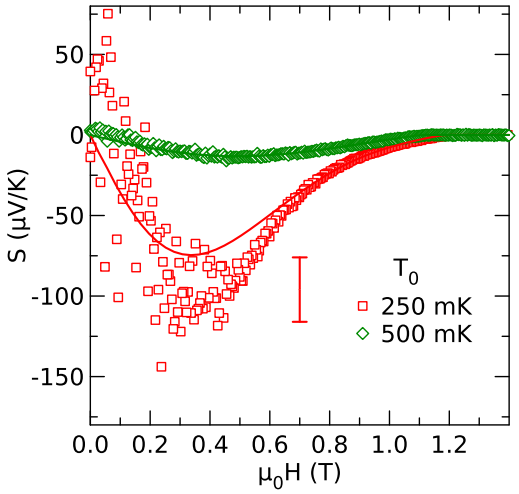


**Figure 4.9:** Seebeck coefficient $S$ of sample FIS1 as a function of $\mu_0 H$ for different $T_0$. The bar indicates the systematic error for $T_0 = 250$ mK.

| sample | $T_0 = 250$ mK | $T_0 = 500$ mK |
|---|---|---|
| FIS1 | $-96 \pm 3 \pm 17_{(\delta T)}$ | $-13.5 \pm 0.2 \pm 2.8_{(\delta T)}$ |
| FIS2 | $-85 \pm 9 \pm 22_{(\delta T)}$ | $-19.5 \pm 0.2 \pm 6.2_{(\delta T)}$ |
| FIS3 | $-46 \pm 4 \pm 16_{(\delta T)}$ | $-9 \pm 0.3 \pm 2.6_{(\delta T)}$ |

**Table 4.3:** Maximum Seebeck coefficient extracted from the data together with error (in $\mu$V/K).

$g$ which shows up in the denominator of equation (39). Thus, also the scatter of $S$ is amplified in the field regime were $g(V = 0, H)$ is nearly zero, well visible in the data for $T_0 = 250$ mK. For $T_0 = 100$ mK the scatter was so large that the data became unreliable, so that they are not shown here. For a better orientation the solid line shows the Seebeck coefficient calculated from the best fits of $I_{\text{th}}$ and $g$. We find good agreement between the data and the fits at $T_0 = 500$ mK. At $T_0 = 250$ mK there is a larger deviation in small fields what again is a consequence of the freeze-out of the quasiparticle conductance. As we divide by the small conductance, even slight deviations between the data and the fit of $g$ result in a large deviation between the data and the fit for $S$.

The maximum values found for the Seebeck coefficient are surprisingly large. At $T_0 = 250$ mK we found $S \approx -100\,\mu$V/K for sample FIS1. An overview of all maximum values for the different samples and the different base temperatures is given in Table 4.3. Here, $S$ was averaged in a field region of 200 mT around the maximum to reduce the scatter of the data. The increase of $S$ for lower $T_0$ is surprising, but a non-monotonic behavior is actually predicted by the theory (see [21, equation (8)]). The standard deviation and the systematic error which occurs due to the uncertainty of the thermal excitation $\delta T$

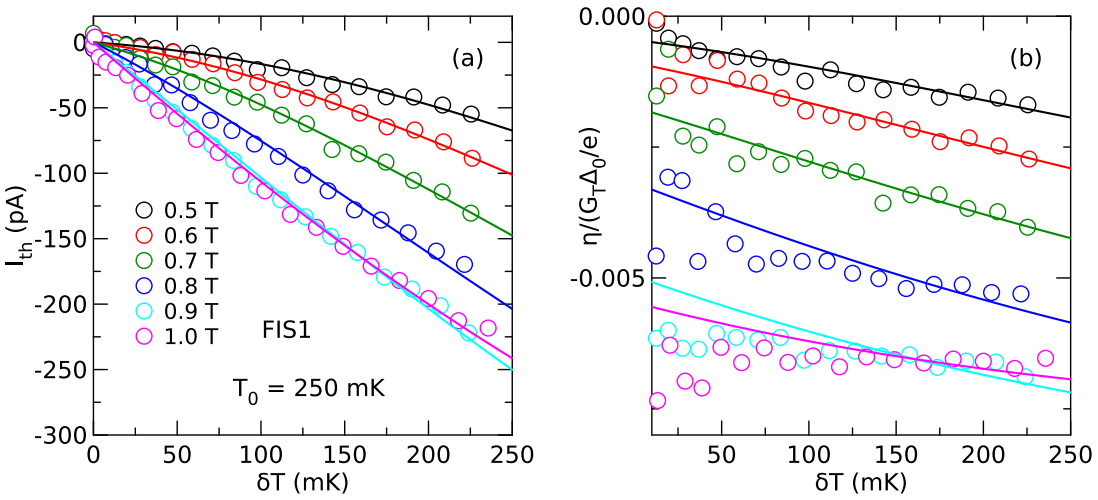


**Figure 4.10:** (a) Thermoelectric current $I_{\mathrm{th}}$ as a function of the thermal excitation $\delta T$ for different magnetic fields $\mu_0 H$. (b) Thermoelectric coefficient $\eta$ as a function of $\delta T$ for the same fields. In both panels data from sample FIS1 are shown for $T_0 = 250$ mK.

are also shown in the table.

### 4.3.3 Dependence on the thermal excitation

In the following, the dependence of the thermoelectric current on the magnitude of the thermal excitation $\delta T$ is discussed. For this purpose, measurements of the thermoelectric current $I_{\mathrm{th}}$ were done at various fixed magnetic fields as a function of the applied heater current $I_{\mathrm{heat}}$ as well as measurements of $I_{\mathrm{th}}$ a function of the magnetic field for different fixed thermal excitations.

In Figure 4.10 data of $I_{\mathrm{th}}$ are shown as a function of $\delta T$ for different magnetic fields $\mu_0 H$. The data stem from sample FIS1 and were measured at base temperature $T_0 = 250$ mK. For the analysis of the data the heater current was initially converted into the thermal excitation $\delta T_{\mathrm{F}}$ with the help of the calibration curves. Then, the data were fitted by the theory model for thermoelectric current, equation (27), and the reduction of the actual thermal excitation was accounted by setting $\delta T = a_0 \cdot \delta T_{\mathrm{F}}$ with $a_0$ as free fit parameter. This resulted in $a_0 \approx 0.93$ for all fits and the corrected thermal excitation $\delta T$ was used for the plot. In Figure 4.10(a) one first notes that the thermoelectric current is increasing for higher magnetic fields which is consistent with the results of the field dependent measurements of $I_{\mathrm{th}}$ (see Fig. 4.7). Furthermore, the current dependence on the thermal excitation is linear in magnetic fields around $\mu_0 H = 1$ T, while in small fields it has a nonlinear dependence on the thermal excitation.

This behavior can be understood by the following considerations. In the ferromagnet the occupation of the states is given by the Fermi distribution, equation (17), which

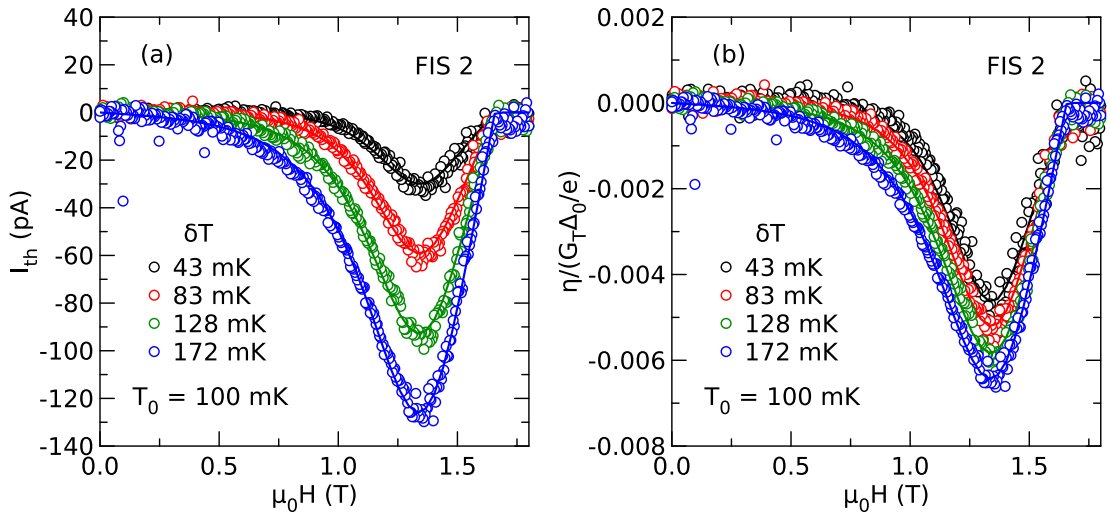


**Figure 4.11:** (a) Thermoelectric current $I_{\mathrm{th}}$ as a function of the magnetic field $\mu_0 H$ for several thermal excitations $\delta T$. (b) Inferred thermoelectric coefficient $\eta$ as a function of $\mu_0 H$ for the same $\delta T$. In both panels data from sample FIS2 are shown at $T_0 = 100$ mK and fit values were used for $\delta T$.

itself depends on the the electronic temperature $T_{\mathrm{F}} = T + \delta T$ of the ferromagnet. A higher thermal excitation $\delta T$ broadens the Fermi distribution, so that states with higher energy are excited in the ferromagnet. On the other hand, the density of states in the superconductor exhibits a non-vanishing energy gap in small magnetic fields which is reflected e.g. in the conductance spectra $g(V)$ (Figure 4.1(a)). Consequently, in the small field regime only the tail of the electrons in the ferromagnet which have energies above the energy gap can participate to the thermoelectric current. As the Fermi distribution has an exponential energy dependence on the temperature itself, the dependence of the current on the thermal excitation is also found to be nonlinear. By increasing the magnetic field the energy gap closes, so that now all electrons near the Fermi level can participate to the thermoelectric current. Therefore $I_{\mathrm{th}}$ increases and the nonlinearity in the dependence on the thermal excitation vanishes.

In Figure 4.10(b) the coefficient $\eta$, normalized to $G_{\mathrm{T}}$ and $\Delta_0/e$, is plotted as a function of $\delta T$ together with fits (solid lines) to equation (27). It is derived by equation (38) from the raw data of panel (a) and the best fit value for $\delta T$. One can see that it reflects the behavior of the raw data. In small fields $\eta$ shows a weak dependence on the thermal excitation as it slightly rises with increasing $\delta T$, thereby illustrating the nonlinearity of $I_{\mathrm{th}}$. The larger the magnetic field is, the smaller becomes the dependence on the thermal excitation. At $\mu_0 H = 1$ T, where the maximum for $I_{\mathrm{th}}$, was found $\eta$ finally is almost constant. Thus, this field regime, where the superconductivity is gap-less, looks promising for the detection of the electronic temperature of the ferromagnet as it can provide linear response for small changes of the electronic temperature.

In Figure 4.11(a) $I_{\mathrm{th}}$ is shown as a function of the magnetic field $\mu_0 H$ for different

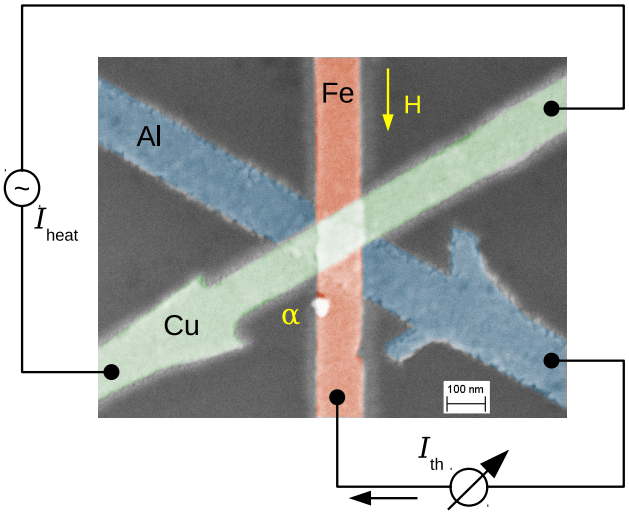


**Figure 4.12:** Colorized scanning electron microscope image of junction $\alpha$ of sample FIS3. Also depicted is the configuration for measuring the thermoelectric current $I_{\mathrm{th}}$, while creating the thermal excitation by heating the copper wire with the heat current $I_{\mathrm{heat}}$.

heater excitations $\delta T$. The data were measured for sample FIS2 at base temperature $T_0 = 100$ mK. The shown $\delta T$ represent again best fit values. One observes an increase of the thermoelectric current as well as a rise of the current in smaller fields for higher thermal excitation. Thereby, again the nonlinearity of $I_{\mathrm{th}}$ in the small field regime is visible. Larger thermal excitation increases the broadening of the Fermi distribution in F and therefore the energy interval $k_{\mathrm{B}}(T+\delta T)$ around the Fermi level in which electronic states are excited. So, also in small fields where the energy gap is still pronounced electrons have enough energy to tunnel and to contribute to the thermoelectric current.

In Figure 4.11(b) the resulting thermoelectric coefficient $\eta$ is shown as a function of the magnetic field $\mu_0 H$. One observes that $\eta$ has a slight dependence on $\delta T$ in the whole field range. As expected the dependence is more pronounced in small fields and smaller near the critical field where the energy gap is reduced in the superconductor.

### 4.3.4 Heating the copper wire

For the samples with the 6-pole junction $\alpha$ it was possible to switch the measurement configuration. The ferromagnet is then heated by applying the heater current $I_{\mathrm{heat}}$ to the copper wire and the resulting thermoelectric current $I_{\mathrm{th}}$ is directly measured between the aluminum wire and the iron wire. The appropriate measurement scheme is depicted in Figure 4.12 in a colorized SEM image of junction $\alpha$ of sample FIS3. For estimating the thermal excitation which is generated by a certain heater current $I_{\mathrm{heat}}$ the calibration measurements were repeated, this time by measuring the differential conductance $g(V)$ of the junction while the dc-heater current was applied to the copper wire.

The results of the copper heating experiments are summarized in Figure 4.13. In panel (a) the electronic temperature $T_{\mathrm{F}}$ extracted from the calibration measurements is shown

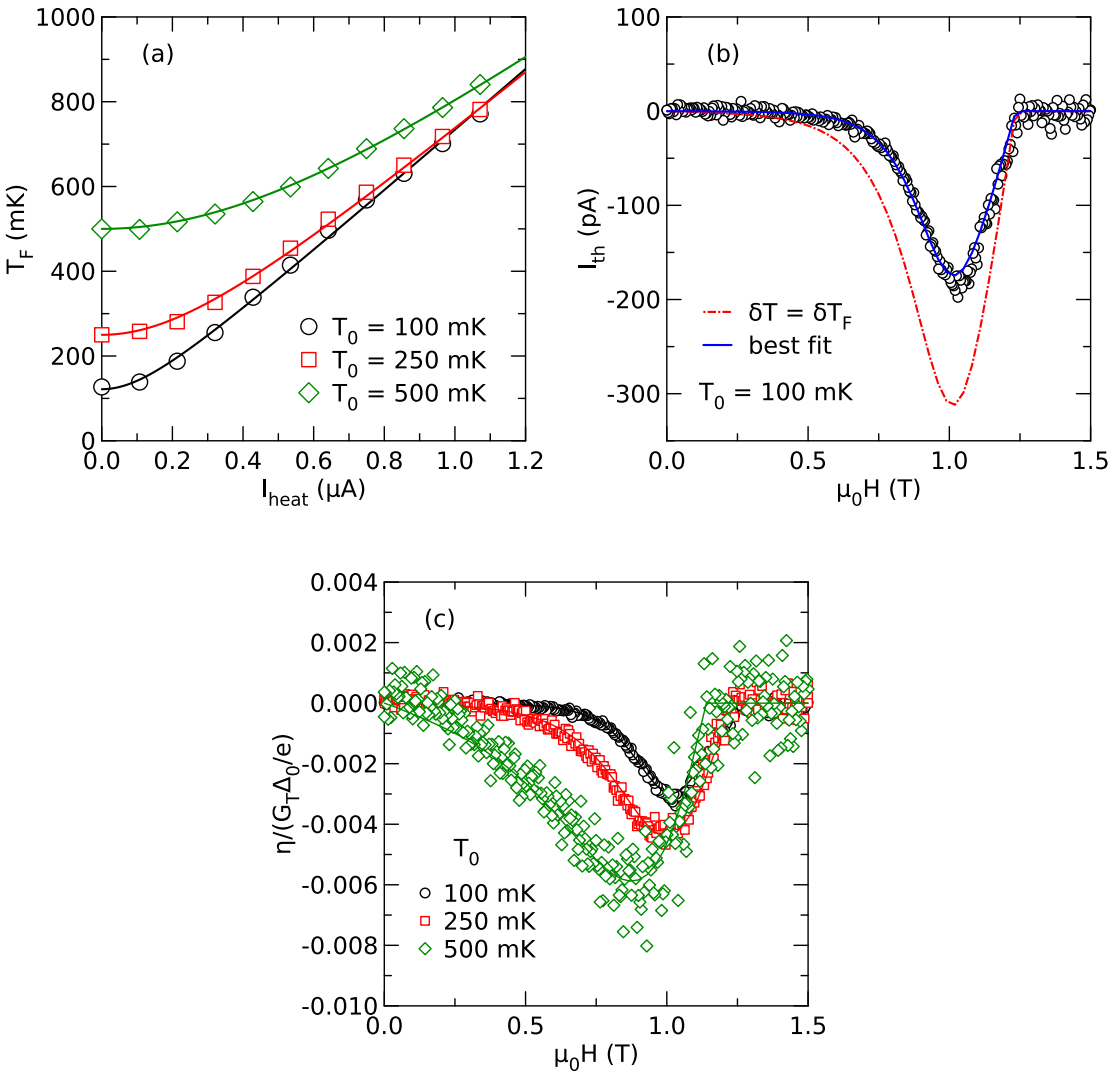


**Figure 4.13:** Overview of the measurements done at sample FIS3 to calibrate and measure the thermoelectric effect while heating the copper wire. (a) Calibration of the electronic temperature $T_\mathrm{F}$ of the ferromagnet while dc-heater current $I_\mathrm{heat}$ was applied to the copper wire. (b) Thermoelectric current $I_\mathrm{th}$ as a function of the magnetic field $\mu_0 H$ for $T_0 = 100$ mK. The solid and the dash-dotted lines show theoretical calculations which are described in the text. (c) Resulting thermoelectric coefficient $\eta$ as a function of $\mu_0 H$ for different base temperatures $T_0$.

as a function of the heater current $I_{\mathrm{heat}}$. One observes a similar result as for the calibration measurements shown earlier (Fig. 4.4(b)). The electronic temperature $T_{\mathrm{F}}$ of the ferromagnetic part of the contact was fitted again according to the heating model, equation (36). From the fits (solid lines) the heater resistance $R_{\mathrm{heat}} \approx 220\ \Omega$ is extracted which is similar to the two-probe resistance $R_{\mathrm{Cu}} = 390\ \Omega$ of the copper wire. The good agreement of both values reflects the fact that the cooling effect of the thin iron wire is smaller than that of the thick copper wire (for comparison see section 4.2). The extracted calibration curves were used to estimate the thermal excitation $\delta T_{\mathrm{F}}$ which was applied for the thermoelectric measurements.

In Figure 4.13(b) the resulting thermoelectric current $I_{\mathrm{th}}$ is shown as a function of the magnetic field $\mu_0 H$ for $T_0 = 100$ mK. It is visible that the switching of the measurement configuration had no impact on the qualitative behavior of the thermoelectric signal. As for the other measurement configuration, $I_{\mathrm{th}}$ vanishes in small fields and rises together with the Zeeman splitting of the density of states. In the field where the energy gap closes the current has its maximum value and then goes back to zero as the magnetic field approaches the critical field. Here, two theoretical calculations of the thermoelectric current are plotted. They were done according to equation (27) with the use of the characteristic junction parameters. The red dotted line shows a estimation done under the assumption $\delta T = \delta T_{\mathrm{F}} = 166$ mK which is extracted from the calibration measurement, while the blue solid line shows a fit that results $\delta T_{\mathrm{fit}} = 94$mK. In the larger deviation of both values it is reflected that the temperature calibration for this sample was not yet as accurate as it was for the later measured (and previously discussed) ones. As a reliable calibration measurement for $T_{\mathrm{S}}$ was unfortunately not done for sample FIS3, the modeled curve for the assumption $\delta T = \delta T_{\mathrm{F}} - \delta T_{\mathrm{S}}$ is missing here.

In Figure 4.13(c) the thermoelectric coefficient $\eta$ is plotted as a function of $\mu_0 H$ for different base temperatures $T_0$. In principle, it shows the same behavior as for the measurements where the iron wire was heated. Note that the measurements were done with the same heater current $I_{\mathrm{th}}$ applied for all base temperatures while the thermal excitation was calibrated afterwards. As at $T_0 = 500$ mK the heating is less effective, $\delta T$ is smaller at this base temperature and thus the scatter of $\eta$ is blown up. (For the later measured sample we adjusted the heater current according to the calibration curves to generate the thermal excitation $\delta T \approx 100$ mK for all base temperatures.)

Altogether, we found no serious deviations of the measurement results for both heating configurations, and as heating by applying current through the higher resistive iron wire turned out to be more effective, in the main part of this work the results of measurements with the iron heating configuration are shown.

### 4.3.5 Possible spurious effects

Several control experiments were done to confirm that the thermoelectric signals presented so far are real and not generated by spurious effects which are induced by

parasitic contributions due to the measurement setup. As described above, the thermoelectric measurements were performed in such a way that only the thermal excitation $\delta T$ dropped across the ferromagnetic junction (see Figure 3.6). However spreading resistance of the iron/copper wires on top of the FIS junction (only samples FIS1, FIS3 and NIS) or crosstalk in the cryostat wiring (all samples) can produce a parasitic voltage excitation $V_{\mathrm{par}}$ across the junction when heater current is applied. The parasitic voltage itself produces a signal that mimics the thermoelectric current signal. This is shown in Figure 4.14(a) where the current $I_{2\omega}$ which is proportional to the second harmonic of the excitation frequency $\omega$ is plotted as a function of the magnetic field $\mu_0 H$. It was measured by using second harmonic detection technique simultaneously with the zero-bias conductance. Here, a peak to peak ac-voltage excitation $V_{\mathrm{ac}} \approx 9\ \mu$V was applied across the junction and the thermal excitation was $\delta T = 0$.

One observes that $I_{2\omega}$ which is proportional to the derivative of the junctions conductance $g_2 = d^2I/dV^2$ exhibits the same shape as the thermoelectric signal. This is not surprising as according to Mott's relation, equation (26), the thermoelectric effect itself is proportional to the derivative of the conductance $g$. The red line in the panel shows an estimation for $I_{2\omega}$ which was done by using the junction parameters and the excitations $V_{\mathrm{ac}} \approx 9\ \mu$V and $\delta T = 0$. The good agreement with the data shows that the observed signal is caused by the voltage excitation. So, we see that a parasitic contribution of voltage, caused by spreading resistance or crosstalk effects, can mimic the thermoelectric effect and can not be excluded a priori.

However, a possible parasitic voltage $V_{\mathrm{par}}$ can be estimated by measuring the part of the current $I(V,T)$ which is proportional to the third harmonic. In order to understand this, it is useful to expand the current $I(V,T)$ across the junction under the assumption that the thermal excitation $T(t) = T_0 + T_{\mathrm{ac}} \sin^2(\omega t)$ and the voltage excitation $V(t) = V_0 + V_{\mathrm{ac}} \sin(\omega t)$ are applied together. One obtains (expanded up to the second order in V and up to the first order in T)

$$\begin{aligned} I(t) &= I(V_0,T_0) + g_2 \frac{V_{\mathrm{ac}}^2}{4} + i_{\mathrm{T}} \frac{T_{\mathrm{ac}}}{2} \\ &+ \left( g V_{\mathrm{ac}} + g_{\mathrm{T}} \frac{3 T_{\mathrm{ac}} V_{\mathrm{ac}}}{4} \right) \sin(\omega t) \\ &- \left( g_2 \frac{V_{\mathrm{ac}}^2}{4} + i_{\mathrm{T}} \frac{T_{\mathrm{ac}}}{2} \right) \cos(2\omega t) \\ &- g_{\mathrm{T}} \frac{T_{\mathrm{ac}} V_{\mathrm{ac}}}{4} \sin(3\omega t) \end{aligned} \tag{40}$$

where $g = dI/dV, g_2 = d^2I/dV^2, g_{\mathrm{T}} = dg/dT = d^2I/dVdT$ are the conductance and its derivatives, and $i_{\mathrm{T}} = dI/dT$ is the thermoelectric current. With the help of equation (40) it is possible to discuss the lowest order spurious effect caused by $V_{\mathrm{ac}}$.

In Figure 4.14(b) the third harmonic part of the current $I_{3\omega}$ is plotted as a function

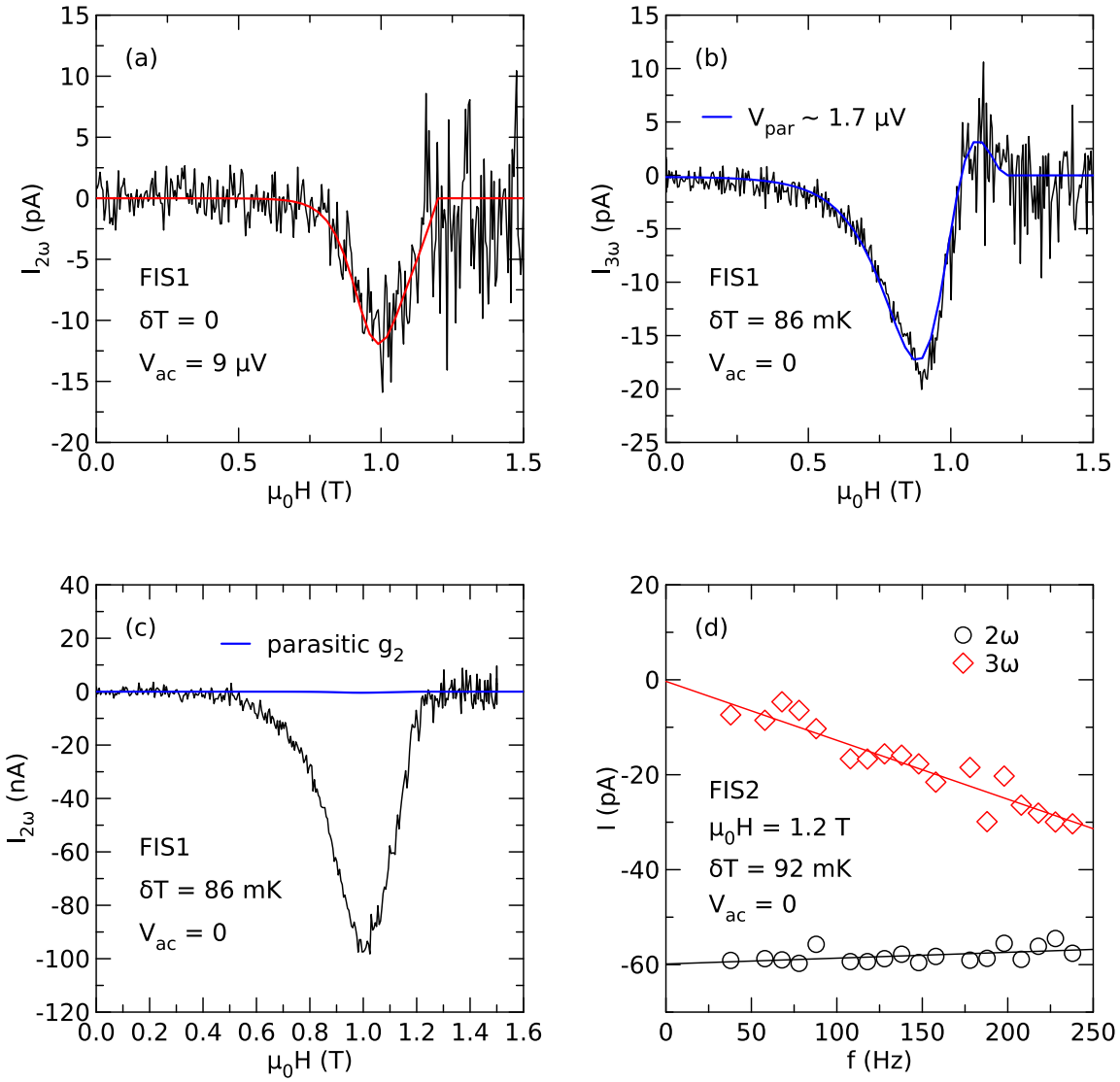


**Figure 4.14:** (a) Second derivative of the current $g_2$ measured on sample FIS1 at $T_0 = 100$ mK as a function of the magnetic field $\mu_0 H$. (b) Third harmonic measured with a thermal excitation $\delta T = 86$ mK and no intentional bias excitation. The fit estimates the parasitic voltage excitation $V_{\mathrm{par}} \sim 1.7$ $\mu$V. (c) Second harmonic measured under the same condition. The fit estimates the parasitic contribution of $g_2$ to the signal, derived from the measurement in (b). (d) Second and third harmonic as a function of the frequency $f = \omega/2\pi$ for sample FIS2 at $\mu_0 H = 1.2$ T. Lines are linear fits. The data of all panels were taken at the base temperature $T_0 = 100$ mK.

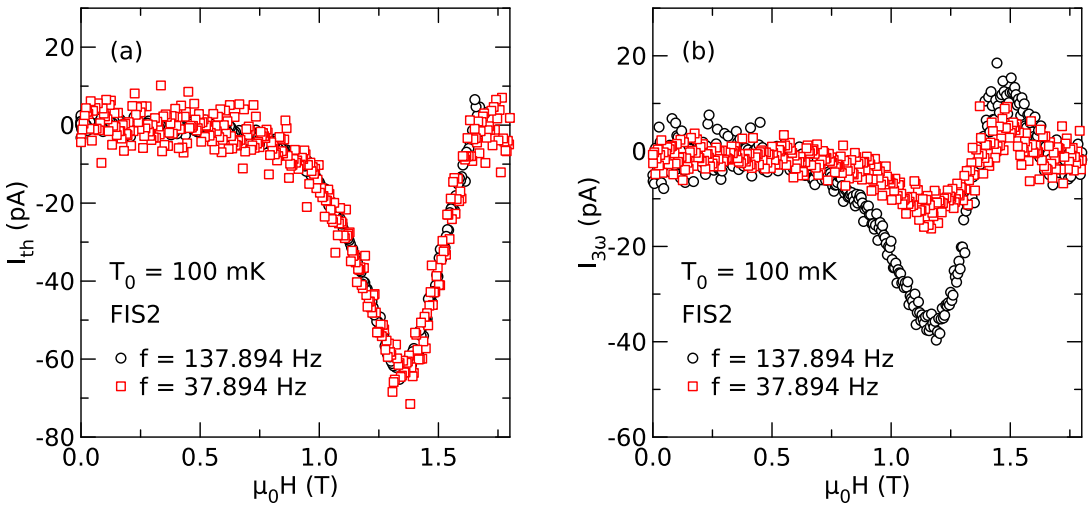


**Figure 4.15:** Frequency dependence of (a) the thermoelectric current $I_{\mathrm{th}}$ and (b) the third harmonic part $I_{3\omega}$ of the current. Both quantities are plotted as a function of the magnetic field $\mu_0 H$ and were measured for sample FIS2 at the base temperature $T_0 = 100$ mK.

of the magnetic field $\mu_0 H$. It was measured simultaneously with the thermoelectric current. We therefore know from our previous analysis (see Fig. 4.7(a) and table 4.2) that the thermal excitation for this measurement was $\delta T = 86$ mK while the intended voltage excitation was $V_{\mathrm{ac}} = 0$. From a fit, depicted as blue solid line in the panel, with the characteristic junction parameters we can infer the parasitic voltage $V_{\mathrm{par}} \approx 1.7\ \mu$V. Now, we are able to estimate the contribution of $g_2$ to $I_{2\omega}$. The solid blue line in Figure 4.14(c) shows the current that one can expect for $V_{\mathrm{par}} = 1.7\ \mu$V and $\delta T = 0$. For comparison, the black line shows the measured curve. On can observe that the parasitic contribution is around two orders of magnitudes smaller than the measured signal and can therefore be considered as negligible.

For sample FIS2 the frequency dependence of the thermoelectric signal was measured to check further influences of crosstalk. In Figure 4.14(d) the second and third harmonic parts of the current $I(V,T)$ are shown as a function of the excitation frequency $f = \omega/2\pi$ at $T_0 = 100$ mK. The data are shown for the magnetic field $\mu_0 H = 1.2$ T where the thermoelectric signal reached its maximum value for this sample (see Figure 4.7(b)). We observe that the second harmonic is nearly independent of the frequency as it is expected for a thermoelectric signal driven by ohmic heating. On the other hand the third harmonic signal is proportional to the frequency which indicates that it is generated by crosstalk. As guide for the eyes linear fits are plotted here as solid lines.

In Figure 4.15(a) the thermoelectric current $I_{\mathrm{th}}$ is plotted as a function of the magnetic field $\mu_0 H$ for two different frequencies. Data which were measured with the usually used excitation frequency $f = 137.894$ Hz are compared to data which were measured at lower frequency $f = 37.894$ Hz. There are no deviations between both curves in

the whole field range observable, so that the current can be assumed to be frequency independent. For comparison in Figure 4.15(b) the third harmonic $I_{3\omega}$ is plotted as a function of $\mu_0 H$ for the same frequencies. Here we find a clear deviation of the amplitudes of both curves.

Altogether, the control experiments demonstrate that the observed thermoelectric current is real. It was neither mimicked by parasitic voltage contributions nor altered by crosstalk.

# 5 Thermoelectric effect in FIS junctions on top of EuS

In this chapter further studies of the thermoelectric effect are presented for structures where the superconductor is in direct contact with a ferromagnetic insulator. In the literature [12,34–37] it is reported that in these systems an intrinsic exchange field $B^*$ is induced in S. This exchange field boosts the spin splitting of the quasiparticle density of states in addition to the applied field $\mu_0 H$. Here, the ferromagnetic insulator europium sulfide (EuS) is used as the fabrication of nanoscale superconducting hybrid structures on top of this substrate was established recently [33] in our group. The aim of this chapter is to discuss in how the exchange field $B^*$ influences the thermoelectric effect. The main results of the chapter are submitted and can also be found in reference [83].

## 5.1 Preparation of the sample

The fabrication process was done in a two-stage process. First plain europium sulfide films were evaporated separately as described in chapter 3.2. On top of these films samples for thermoelectric measurements were structured by the following fabrication process.

The plain EuS films were purged in acetone- and isopropanol-baths before a PMMA layer was spin coated on top of them. The following lithography and evaporation processes were in principal the same as for the samples which were structured on oxidized silicon wafers. Additionally, an argon(Ar) ion milling step was included before the evaporation of the metallic structure, with the intention to remove PMMA residues from the EuS surface. This step was required in order to improve the EuS/Al interface as even small residues there can destroy the generation of the exchange field.

The samples were mounted in the evaporation system and first cooled in the main chamber below $-100$°C for around an hour to prevent the resist from melting during the Ar milling step. The cooled samples were transferred into the load lock where the Ar milling was done. By a needle valve the flux of argon ions into the load lock was regulated to achieve a constant pressure $p \approx 1 \cdot 10^{-4}$ mbar. The $Ar^+$ ions were accelerated by applying a voltage $U = 1$ kV. The stability of the plasma during the sputter process was checked by measuring the current flowing through the metallic sample holder. Here, typically values $I_{\text{ion}} \approx 60\mu$A were found. Under these conditions the EuS etching rate is expected to be approximately 0.75 nm/min [33]. Determining the right duration of the Ar milling step is crucial as too short processes would not remove all residues, while too long processes probably damage the EuS surface. In both cases the properties of the exchange field are affected and it might be suppressed. As a compromise, throughout this work a duration of $t = 3$ min was chosen. After the Ar ion milling step was completed, the samples were transferred back into the main

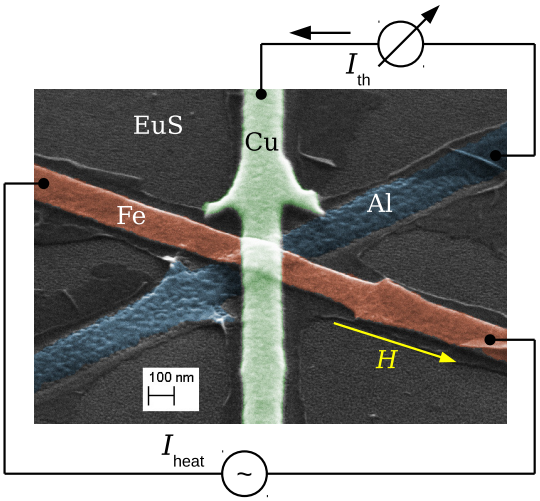


**Figure 5.1:** False-color coded scanning electron microscopy image of junction $\alpha$ of sample EUS2. Additionally depicted is the scheme for the thermoelectric measurements.

chamber and metallic structures were fabricated by the usual evaporation process (see chapter 3.1).

Altogether three thermoelectric samples on top of europium sulfide were measured for this work. They are labeled as samples EUS1-EUS3 and all of them had the same layout as sample FIS1 (compare to Figure 3.2(b)). Figure 5.1 shows a false-color coded image of sample EUS2 together with the measurement scheme for thermoelectric measurements. The samples consisted of an aluminum wire (blue) with the FIS junction $\alpha$, which was overlaid by an additional copper wire (green), and the NIS junction $\beta$. In the picture only the main part, the ferromagnetic junction $\alpha$ is shown. As ferromagnetic metal, again iron (red) was used. In the background of the SEM image, one recognizes the granular europium sulfide substrate film. For a better comparison to the previous samples, the thicknesses of the materials were again chosen to be $t_{\mathrm{Al}} \approx 20$ nm, $t_{\mathrm{FE}} \approx 20$ nm and $t_{\mathrm{Cu}} \approx 50$ nm. The measurement program was the same as established in the last chapter. First conductance measurements were done to characterize and extract the properties of junction $\alpha$, followed by calibration measurements for the estimation of the thermal excitation $\delta T$. Finally, the thermoelectric measurements were done.

## 5.2 Proximity induced exchange field

We want to start the discussion of the measurement results with the conductance spectra of junction $\alpha$. Figure 5.2(a) shows the differential conductance $g$ as a function of the voltage $V$ for different applied magnetic fields $\mu_0 H$. The data were measured for sample EUS1 at base temperature $T_0 = 50$ mK. For $\mu_0 H = 0$ one observes that $g(V)$ shows the behavior of a high-quality tunnel junction by the vanishing conductance at small voltages and the coherence peaks at the gap of the superconductor for positive

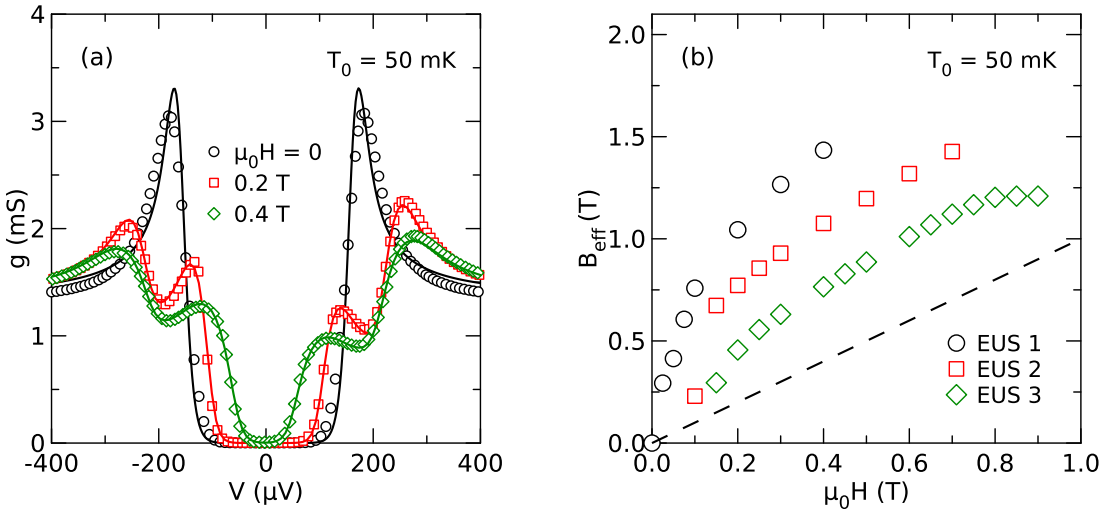


**Figure 5.2:** (a)Differential conductance $g$ of contact $\alpha$ of sample EUS1 as a function of the voltage $V$ for different magnetic fields $\mu_0 H$ at $T_0 = 50$ mK. Fits according to equation (27) are shown as solid lines. (b) Effective spin-splitting field $B_{\text{eff}}$ in the superconductor as a function of $\mu_0 H$ for the three EuS samples. The data were extracted by fits of the differential conductance as described in the text. The dashed line marks $B_{\text{eff}} = \mu_0 H$.

and negative voltages. In applied magnetic field one observes again a split-up of the coherence peaks due to the spin splitting of the quasiparticle DOS. We observe that the curve already exhibits a significant spin splitting for $\mu_0 H = 0.2$ T, while for sample FIS1 (fabricated without EuS substrate) the spin splitting was only visible for fields $\mu_0 H > 0.5$ T. The reason for this behavior is the additional intrinsic exchange field $B^*$ which is induced by the spin-active scattering of the quasiparticles at the interface to the ferromagnetic insulator.

To evaluate $B^*$ the conductance curves $g(V)$ were fitted again to the standard model for high-field tunneling, equation (27). The fits are plotted in Figure 5.2(a) as solid lines and we see that they are in good agreement with the data. First, the spin polarization $P$ of the tunnel junction was extracted from the fits of the conductance curves in high magnetic field, while for the spin-orbit scattering strength $b_{\text{so}}$ a suitable and reasonable value was chosen. For sample EUS1 these values are $P = 0.17$ and $b_{\text{so}} = 0.04$. Due to the larger polarization of the junction (compared to the samples shown earlier), the asymmetry of the peak heights for positive and negative voltages $V$ is clearly visible now. Then, $P$ and $b_{\text{so}}$ were fixed and the normal conductance of the junction $G_{\text{T}}$, the pair potential $\Delta$, the orbital pair-breaking $\Gamma$ and the effective spin-splitting field $B_{\text{eff}}$ were fitted for all fields.

The most interesting parameter here is $B_{\text{eff}}$ as the exchange field $B^*$ can directly be inferred from it. In Figure 5.2(b) $B_{\text{eff}}$ is plotted as a function for $\mu_0 H$ for the different EuS samples. The data in this panel stem from fits of the conductance curves which were measured at $T_0 = 50$ mK. Additionally, a dashed line marks $B_{\text{eff}} = \mu_0 H$. We see

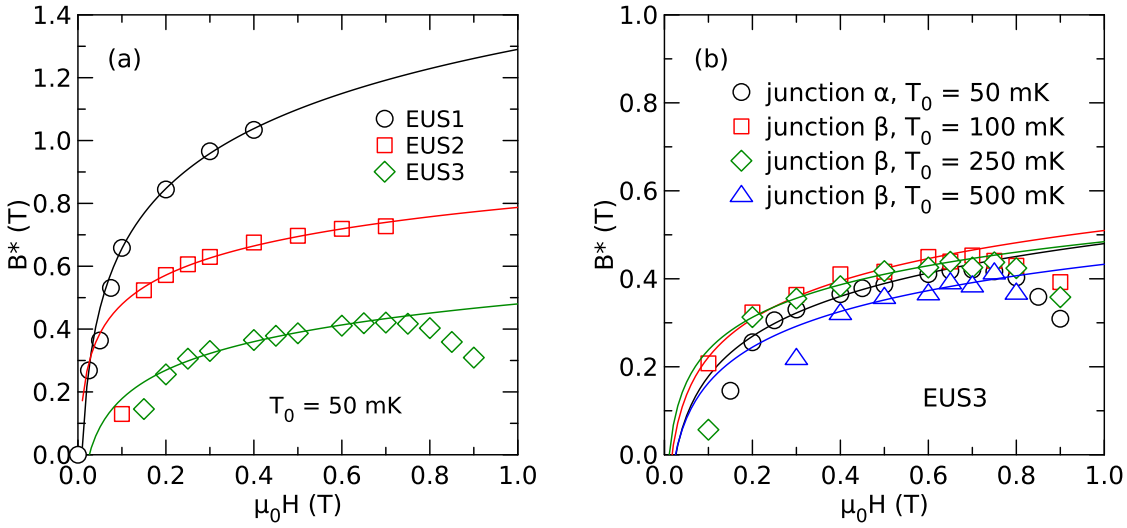


**Figure 5.3:** Exchange field $B^* = B_{\text{eff}} - \mu_0 H$ as a function of $\mu_0 H$ together with phenomenological fits according to Eq. (41). (a) Comparison of the data for all three samples. (b) $B^*$ at different base temperatures $T_0$ for sample EUS3.

that the actual spin splitting is larger for all samples than that one which is expected from the pure Zeeman splitting due to the applied field. We account this boost to the intrinsic exchange field $B^*$ and analyze it by calculating the difference between $B_{\text{eff}}$ and $\mu_0 H$. For example, at $\mu_0 H = 0.2$ T we find $B_{\text{eff}} = 1.06$ T for sample EUS1. So, the main part of the spin splitting is generated by the exchange field $B^* = B_{\text{eff}} - \mu_0 H = 0.86$T here.

In Figure 5.3(a) the exchange field $B^*$ is plotted in the whole magnetic field range for all three samples. For the further progress of this work it was necessary to find a sufficient phenomenological description of $B^*(H)$ in order to model the effective spin-splitting field as a function of the magnetic field. This is required later for the description of the field dependence of the thermoelectric current. First attempts were done, following the work of Michael Wolf [33], by fitting the data to a Brillouin function. However, with this model we found a discrepancy between the data and the fits. Next, we tried a logarithmic field dependence which is known from a study of Xiong et al. [37] for the EuS/Al proximity system. In Figure 5.3(a) fits according to

$$B^* = a \cdot \ln(H/H_0) \tag{41}$$

with the phenomenological fit parameter $a$ and $H_0$ are drawn as solid lines. We see that this model provides sufficient agreement between the fits and the data, especially in the field range 0.1 T $< \mu_0 H <$ 1 T. The deviations in small fields (samples EUS2 and EUS3) are tolerable as the thermoelectric current occurs mainly in high fields, a region where the logarithmic fits show adequate agreement. Therefore, we included the

intrinsic exchange field described by equation (41) in the model which we use to predict the thermoelectric current. The effective spin-splitting field is then described by

$$B_{\text{eff}} = \mu_0 H + a \cdot \ln(H/H_0). \tag{42}$$

As seen for the samples without EuS, $B_{\text{eff}}$ is renormalized near the critical field (here only visible for sample EUS3) due to the interaction of the quasiparticles, so that it approaches to the normal state value

$$B_{\text{eff}} = \frac{\mu_0 H + B^*}{1 + G_0}. \tag{43}$$

For sample EUS3 we checked the dependence of the exchange field on the base temperature since reference [37] revealed that $B^*$ is weakened for higher $T_0$. As at junction $\alpha$ the analysis of the exchange field is influenced by the presence of the fringing field of the iron wire, the temperature dependence was measured at the non-magnetic junction $\beta$. In Figure 5.3(b) the exchange field $B^*$ is plotted as a function of $\mu_0 H$ for different base temperatures $T_0$. While for junction $\beta$ data for the base temperatures which were usually used for the thermoelectric experiments are shown, for junction $\alpha$ data for $T_0 = 50$ mK which was the usual temperature for the measurement of the conductance spectra are used. We observe that the general field dependence of the data is similar for all $T_0$ and that they show only slight deviations from each other. Supporting the observations of reference [37], a slight reduction of $B^*$ is found for $T_0 = 500$ mK. However, due to the thermal smearing for this temperature the extraction of the effective spin-splitting field $B_{\text{eff}}$ from the conductance curves $g(V)$ is also less reliable. As also deviations of $B^*$ from contact to contact cannot be excluded and the temperature dependence is found to be rather small, we decided to neglect it and to use directly the exchange field measured at junction $\alpha$ for $T_0 = 50$ mK.

One should note here that the field dependence of $B^*$ showed a clear deviation of the field dependence of the magnetization $M_{\text{EuS}}$ of the EuS film (compare to Figure 3.4(b)). All films themselves had coercive fields $H_{\text{co}} \lesssim 5$ mT, so that their magnetization was fully saturated above this field. In a simple picture one expects $B^*$ to be coupled to the magnetization of the EuS film. However, the data show a discrepancy between both and the exchange field exhibits a slower increase especially in small fields. This observation is consistent with the studies of Michael Wolf [33]. As reason for the different behavior of $M_{\text{EuS}}$ and $B^*$ the difference between bulk magnetism (tested in the magnetization measurements) and the surface magnetism (tested in the conductance experiment) seems feasible [12]. This suggestion is supported by the fact that the strength of the exchange field varied from sample to sample. We account this observation to the problem that during the two stage fabrication process the surface of the EuS film might be damaged by the Argon milling step, so that the proximity coupling is modified. To achieve further clarity, studies of EuS/Al proximity systems with samples fabricated in a one-stage process would be of great use.

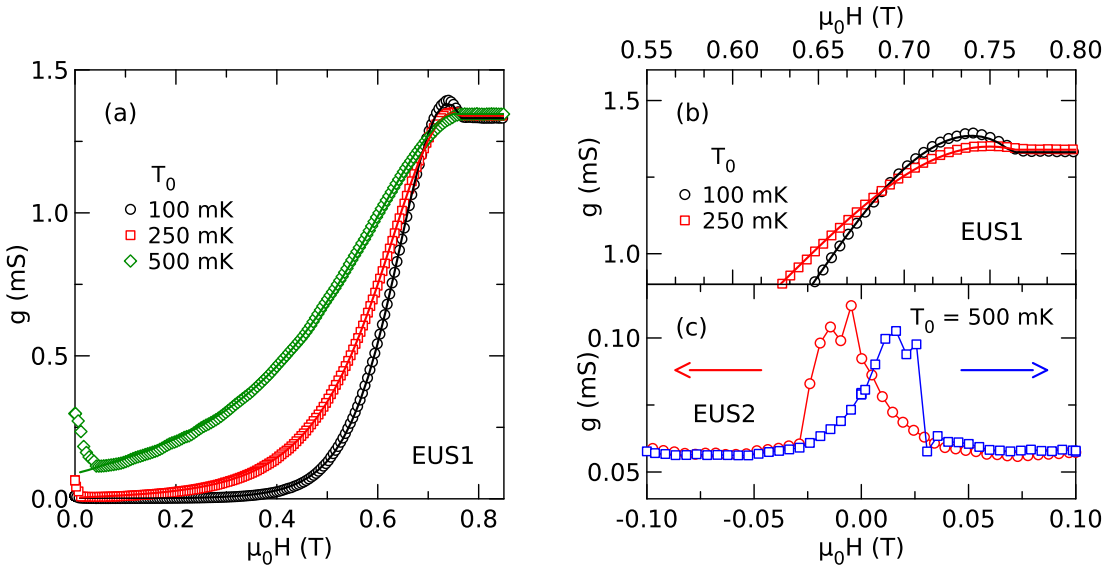


**Figure 5.4:** (a) Differential conductance $g$ as a function of the magnetic field $\mu_0 H$ at $V = 0$ for different base temperatures $T_0$. Data stem from sample EUS1 and are shown together with fits according to equation (27). (b) Magnification of $g$ near the critical field. (c) Hysteresis measurements of $g$ in small magnetic fields. Data were measured for sample EUS2 at $T_0 = 500$ mK. The arrows indicate the direction of the field sweep.

## 5.3 Characterization and calibration measurements

For extracting the characteristic junction parameters which are necessary for modeling the thermoelectric current later on again fits of the field dependent zero-bias conductance $g(V = 0, H)$ were used. In Figure 5.4(a) data for $g(V = 0)$ are shown as a function of $\mu_0 H$ for different base temperatures together with the fits (solid lines) according to equation (27).

One observes that the field dependence of the zero bias conductance is similar as for the samples without EuS, but that the critical field $\mu_0 H_c$ (and hence the whole field range) is reduced due to the additional exchange field. The fits are again in good agreement with the data which indicates a reliable quality of our model which now also includes the phenomenological magnetic field dependence of the intrinsic exchange field.

As a further trial to improve the fits, here, the Fermi-liquid parameter $G_0$ was adjusted by fitting $g$ in the field region close to the critical field. In Fig. 5.4(b) a magnification of the zero-bias conductance near the critical field is shown. One observes an enhancement of the conductance above the normal state value $G_\mathrm{T}$ just below $\mu_0 H_c$ for base temperatures $T_0 = 100$ mK and $T_0 = 250$ mK. Such conductance enhancement was also observed in earlier studies on thin aluminum films [84]. It is sensitive to $G_0$ as many quasiparticles are thermally excited in this field regime, so that the interaction amongst them is strong. We extracted the values $G_0 = 0.21$ for sample EUS1 and $G_0 = 0.26$

| sample | $t_{\mathrm{Al}}$ (nm) | $G_{\mathrm{T}}$ (mS) | $P$ | $b_{\mathrm{so}}$ | $T_{\mathrm{c}}$ (K) | $\mu_0 H_{\mathrm{c}}$ (T) | $\Delta_0$ ($\mu$eV) | $\mu_0 H_{\mathrm{c,orb}}$ (T) | $G_0$ |
|---|---|---|---|---|---|---|---|---|---|
| EUS1 | 20 | 1.33 | 0.15 | 0.04 | 1.4 | 0.76 | 198 | 1.1 | 0.21 |
| EUS2 | 22 | 0.66 | 0.17 | 0.02 | 1.43 | 0.96 | 192 | 1.23 | 0.26 |
| EUS3 | 20 | 0.78 | 0.185 | 0.005 | 1.47 | 1.01 | 190 | 1.16 | 0.26 |

**Table 5.1:** Overview of sample properties for the samples on top of EuS. Thickness $t_{\mathrm{Al}}$ of the aluminum wire extracted from AFM measurements, normal-state tunnel conductance $G_{\mathrm{T}}$ and polarization $P$ of the FIS junction, spin-orbit scattering strength $b_{\mathrm{so}}$. Properties of the aluminum wire: critical temperature $T_{\mathrm{c}}$, critical magnetic field $\mu_0 H_{\mathrm{c}}$, pair potential $\Delta_0$, orbital critical field $\mu_0 H_{\mathrm{c,orb}}$ and Fermi-liquid renormalization parameter $G_0$.

for sample EUS2. For sample EUS3 the zero-bias conductance did not exhibit the enhancement peak, so that fitting of $G_0$ was not successful and $G_0 = 0.26$ was set. Both values are in the range of the literature values for thin aluminum films, $G_0 = 0.17$ [85] and $G_0 = 0.3$ [79] and therefore reasonable, so that we used them for calculating the self-consistent quantities for the samples with EuS.

In small fields $\mu_0 H < 50$ mT an unusual increase of the conductance $g$ was observed. It was found for all temperatures and was most pronounced for $T_0 = 500$ mK. In Figure 5.4(c) a detailed measurement of the conductance in the field region around zero is shown for this base temperature. The data here stem from sample EUS2. The field was swept in both directions, arrows indicate the sweep direction. One observes hysteretic behavior of $g$. Coming from high fields, first the conductance increases while crossing zero field. In negative field, it reaches a maximum, then suddenly exhibits a jump back to a smaller value at $\mu_0 H = -30$ mT. The same happens in the reverse field direction. This effect was not observed for the samples on top of $SiO_2$ (see Fig. 4.2(a)), we attribute it to the inhomogeneous magnetization of the europium sulfide in small magnetic fields. This may either induce an out-of plane stray field or an inhomogeneous exchange field which both would weaken the superconductivity. In fields above 20 mT the magnetization of the EuS film becomes homogeneous again and the conductance flips back to its usual value. Due to the small field range of this effect, it had no impact on the thermoelectric signal and is just mentioned here for completeness.

The characteristic properties of the samples are summarized in Table 5.1. All parameters were extracted in the same way as it was described in chapter 4.1.

For the samples with EuS the electronic temperatures $T_{\mathrm{F}}$ of the ferromagnet and $T_{\mathrm{S}}$ of the superconductor also had to be calibrated against the heater current $I_{\mathrm{th}}$. The procedure followed the same principle as for the samples without EuS and is discussed here only briefly. In Figure 5.5(a) the conductance $g$ is shown as a function of the voltage $V$ applied across the contact for different heater currents $I_{\mathrm{heat}}$ at base temperature $T_0 = 100$ mK. The magnetic field $\mu_0 H = 0.75$ mT was set as the thermoelectric current reached its maximum value there (next section). Again, one observes that the

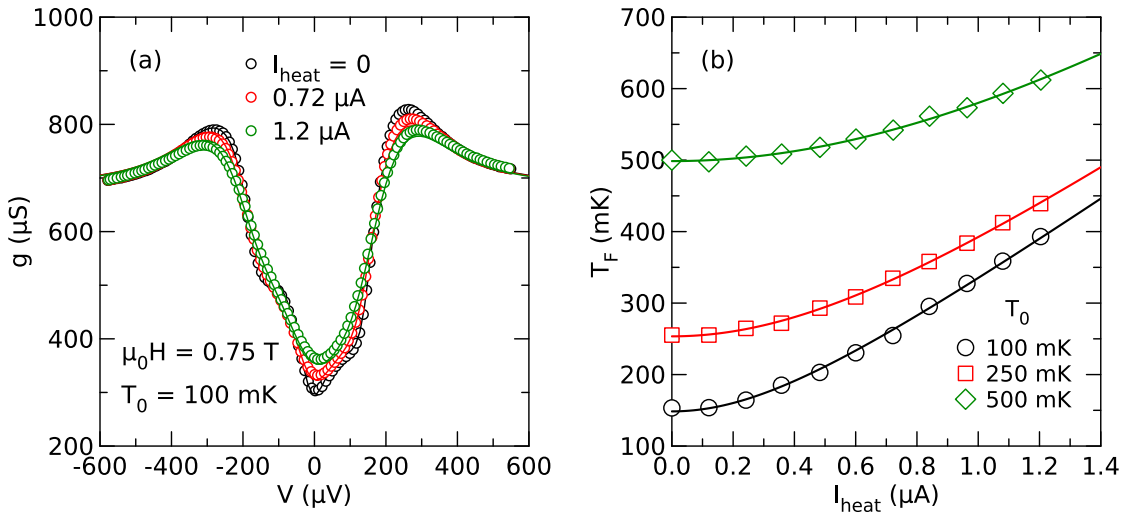


**Figure 5.5:** Calibration of the electronic temperature $T_\mathrm{F}$ of the ferromagnet for sample EUS2. (a) Differential conductance $g$ as a function of voltage $V$ for different heater currents $I_\mathrm{heat}$. (b) Electronic temperature $T_\mathrm{F}$ as a function of the heater current $I_\mathrm{heat}$ for different base temperatures $T_0$.

heater current leads to thermal broadening of the conductance, visible in particular by the increase of $g$ at zero voltage $V = 0$. By fitting the conductance curves for the different heater currents the electronic temperature $T_\mathrm{F}$ of the ferromagnet could be extracted. The result is shown in Figure 5.5(b) where $T_\mathrm{F}$ is plotted as a function of the heater current $I_\mathrm{heat}$ for different base temperatures $T_0$. The heating is described again by the model of a mesoscopic wire in quasi-equilibrium, equation (36). The fits here result in the resistance $R_\mathrm{heat} = 94\ \Omega$. Again this resistance is reduced due to the cooling effect of the thick copper wire with respect to the two probe resistance of the iron wire $R_\mathrm{Fe} = 527\ \Omega$. The extracted fit curves were used to adjust the thermal excitation $\delta T$ for the thermoelectric experiments.

The control measurements done to check the impact of the heating on the temperature of the superconductor were performed in the same way as described in the second part of chapter 4.2 for the samples without EuS. The conductance of junction $\beta$ was measured as a function of $V$ for different heater currents $I_\mathrm{heat}$. Then, the pair potential $\Delta$ was fitted as a function of $I_\mathrm{heat}$. From $\Delta$ the temperature of the superconductor was inferred. Altogether no significant differences were found compared to the samples shown earlier. Again, a temperature increase $\delta T_\mathrm{S} \lesssim 20$ mK of the superconductor temperature was found for a thermal excitation $\delta T_\mathrm{F} \sim 100$ mK of the ferromagnet.

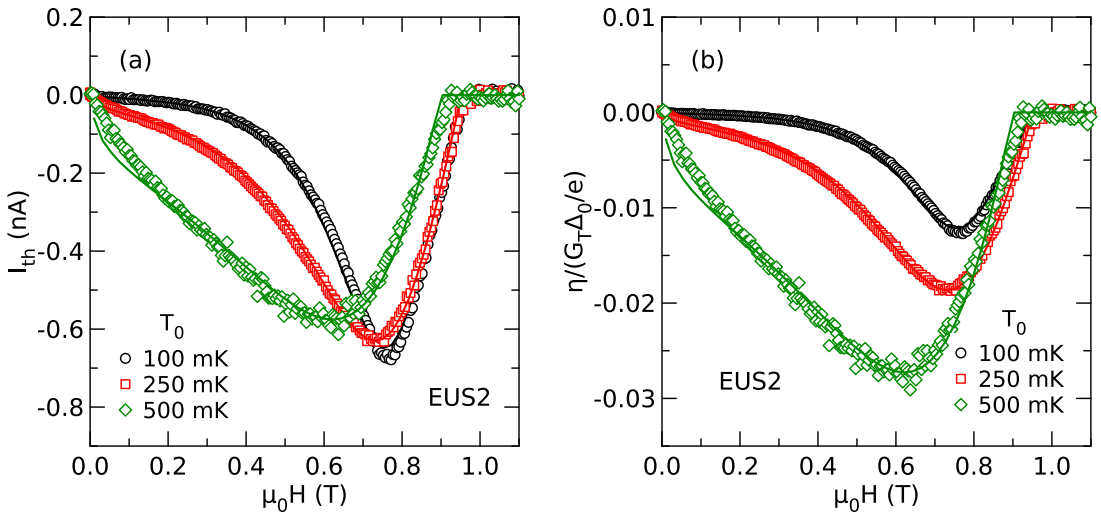


**Figure 5.6:** (a) Thermoelectric current $I_{\mathrm{th}}$ as a function of the applied magnetic field $\mu_0 H$ for different base temperatures $T_0$. Data stem from sample EUS2 and are shown together with fits according to equation (27). (b) Thermoelectric coefficient $\eta$ as a function of $\mu_0 H$. Data are inferred from the thermoelectric current.

## 5.4 Thermoelectric effect

Figure 5.6(a) shows the thermoelectric current $I_{\mathrm{th}}$ as a function of the applied field $\mu_0 H$ for different base temperatures $T_0$. The data in this panel were measured for sample EUS2. For all base temperatures we applied a thermal excitation $\delta T \approx 100$ mK which was set by adjusting the heater current $I_{\mathrm{heat}}$ according to the calibration curve. The thermoelectric current exhibits the familiar signal, however, one can identify the influence of the exchange field. For $T_0 = 100$ mK the current vanishes again in small fields. But then it starts rising already around $\mu_0 H \approx 0.3$ T until it reaches its maximum value at $\mu_0 H \approx 0.75$ T. In higher fields, the signal goes back to zero while it is approaching the critical field. One observes that the whole field regime in which the thermoelectric current is measured shifts to a smaller range compared to the samples without EuS. At higher temperatures the thermoelectric signal is thermally smeared again, so that its maximum value is reduced but it has a larger contribution in small fields.

The solid lines in Figure 5.6(a) show fits to the data which were done with equation (27) and the junction parameters listed in Table 5.1. The exchange field is included in the model described by equation (41) as mentioned earlier. In the panel this time only fits for which the thermal excitation $\delta T_{\mathrm{fit}}$ was adjusted are shown. For all three samples we found $\delta T_{\mathrm{fit}} \sim 0.8 - 0.9\ \delta T_{\mathrm{F}}$ which is consistent with the calibration measurements and the observations for the samples without EuS. In general, excellent agreement between the data and the fits can be observed also for all samples on top of EuS, demonstrating again that the measured current is described well by the theory model [20, 21]. It also

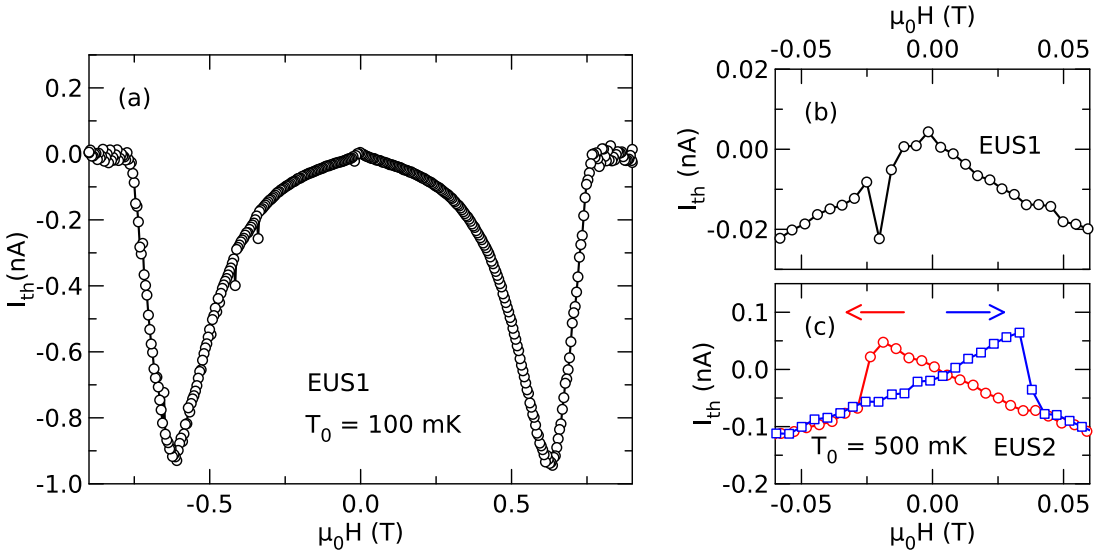


**Figure 5.7:** (a) Thermoelectric current $I_{\mathrm{th}}$ as a function of $\mu_0 H$, both in positive and negative field, at temperature $T_0 = 100$ mK. The data stem from sample EUS1. (b) Magnification of the data of panel (a) in the regime around zero field. (c) Hysteresis of the thermoelectric current around $\mu_0 H = 0$ for $T_0 = 500$ mK. Here the data stem from sample EUS2.

demonstrates that the exchange field can be included into the model by an appropriate phenomenological description. This is not surprising in so far as the theory only demands the presence of a spin-splitting field but does not specify its origin. Thus, adequate proximity structures might also enable the flow of thermoelectric current without the presence of an applied magnetic field.

In Figure 5.6(b) the thermoelectric coefficient $\eta$, normalized to $G_{\mathrm{T}}$ and $\Delta_0/e$, is plotted as a function of $\mu_0 H$. Here, $\eta$ is inferred from the raw data of $I_{\mathrm{th}}$, the electronic temperature $T$ and the thermal excitation $\delta T = \delta T_{\mathrm{fit}}$ by equation (38). Again the theoretically predicted behavior (Figure 2 in reference [21]) is observed. The signal is sharpest for $T_0 = 100$ mK and both broadens and increases in magnitude for higher $T_0$. Also a shift of the maximum value to lower fields is found for higher base temperatures.

As for the samples without EuS we observed that the thermoelectric current crosses zero in small fields (see Figure 4.7 (e) and (f)), further investigations on the magnetic field dependence were done for the samples with EuS. In Figure 5.7(a) the thermoelectric current $I_{\mathrm{th}}$ is shown as a function of the magnetic field $\mu_0 H$, this time both in positive and negative field. The data stem from sample EUS1 and were measured at $T_0 = 100$ mK. In a large majority of the field range we do not observes any influence of the sign of the magnetic field on the thermoelectric signal.

A closer look in the regime around zero field is given in Figure 5.7(b) where a magnification of the data of panel (a) is shown. One sees that in a small range below zero field the current has a positive sign. More pronounced the effect is found again for

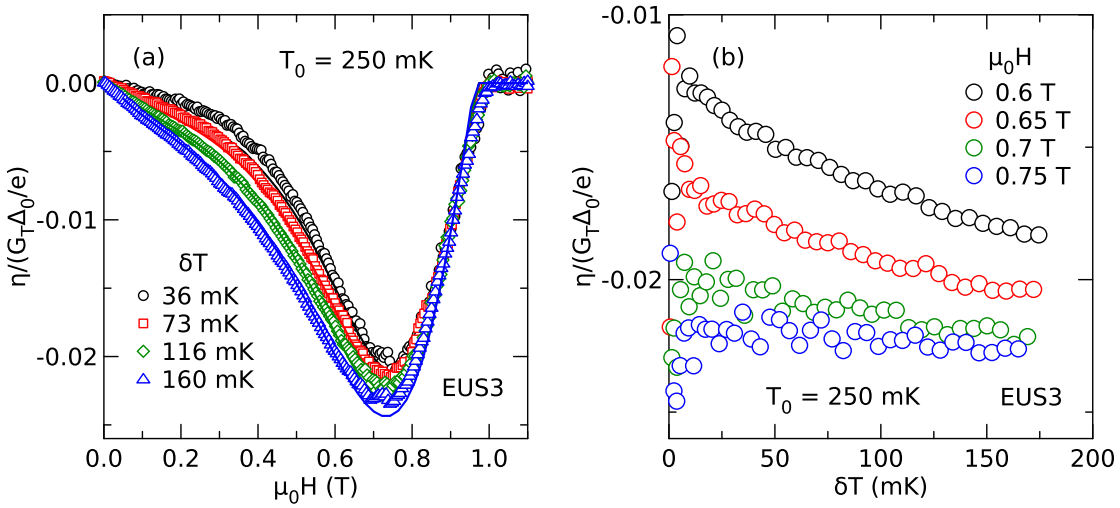


**Figure 5.8:** Dependence of the thermoelectric coefficient $\eta$ on the thermal excitations $\delta T$. The data were measured for sample EUS3 at $T_0 = 250$ mK. (a) $\eta$ normalized on $G_\mathrm{T}$ and $\Delta_0/e$ as a function of the magnetic field $\mu_0 H$ for different $\delta T$. (b) $\eta$ normalized on $G_\mathrm{T}$ and $\Delta_0/e$ as a function of $\delta T$ for several $\mu_0 H$.

higher base temperature. In Figure 5.7(c) a hysteresis measurement of $I_\mathrm{th}$ is shown for $T_0 = 500$ mK. Here, the direction of the particular field sweep is marked with an arrow in the same color. Coming from high fields $I_\mathrm{th}$ first crosses zero and continues to rise until it exhibits a jump back to negative values at $\mu_0 H \approx -30$ mT which is a typical switching field of the iron wire. The same happens in the other field direction. The change of the current sign can be understood as follows. After crossing zero the direction of the field is reversed while at the same time the sign of the magnetization of the iron wire (and therefore also the sign of the polarization $P$) is not changed. Both are therefore antiparallel to each other and the sign of the current changes. When the field is large enough to flip the magnetization of the wire, the field and the polarization are parallel again and the current sign flips back to the usual negative sign.

For the samples with EuS substrates also the dependence of the thermoelectric signal on the size of the thermal excitation $\delta T$ was measured. In Figure 5.8(a) the thermoelectric coefficient $\eta$, normalized to $G_\mathrm{T}$ and $\Delta_0/e$, is plotted as a function of $\mu_0 H$ for several $\delta T$ (which represent the best fit value) at base temperature $T_0 = 250$ mK. One observes a slight dependence of the signal on the magnitude of $\delta T$, especially in small fields. The dependence of $\eta$ on the thermal excitation $\delta T$ for fixed magnetic fields, shown in Figure 5.8(b), also underlines this behavior. The signal is increasing for higher magnetic fields in consistency with the behavior of the signal seen in the field dependent measurements. In smaller fields $\eta$ shows a slight dependence on the thermal excitation, reflecting the nonlinearity of the thermoelectric current in this field regime. In contrast, in the field regime near the maximum, $\eta$ is found to be constant and therefore independent of the thermal excitation. Hence, the thermoelectric current is linear again at fields where the energy gap vanishes in the superconductor. Altogether we find

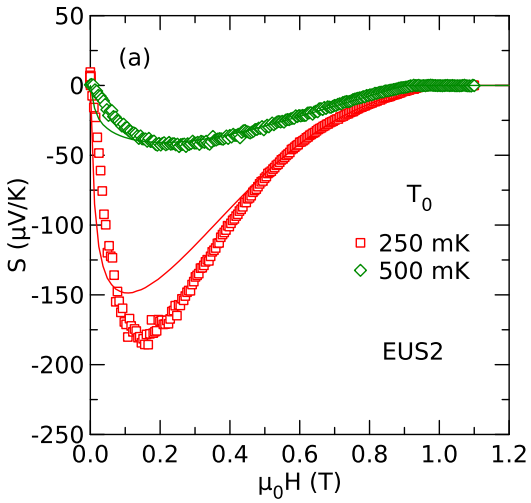


**Figure 5.9:** Seebeck coefficient $S$ as a function of the magnetic field $\mu_0 H$ for different base temperatures $T_0$. The data in this panel stem from sample EUS2. Solid lines correspond to the value extracted from the fits of $I_{\mathrm{th}}$ and $g$.

| sample | $T_0 = 250$ mK | $T_0 = 500$ mK |
|---|---|---|
| EUS1 | $-136 \pm 3 \pm 14_{(\delta T)}$ | $-39.8 \pm 0.3 \pm 0.7_{(\delta T)}$ |
| EUS2 | $-176 \pm 1 \pm 14_{(\delta T)}$ | $-42 \pm 0.2 \pm 2.4_{(\delta T)}$ |
| EUS3 | $-165 \pm 1 \pm 31_{(\delta T)}$ | $-36.3 \pm 0.1 \pm 2.6_{(\delta T)}$ |

**Table 5.2:** Maximum Seebeck coefficient extracted from the data together with error (in $\mu$V/K).

a similar dependence on the thermal excitation here as for the samples without EuS.

In Figure 5.9(a) the Seebeck coefficient $S$ is plotted as a function of the magnetic field $\mu_0 H$ for different base temperatures $T_0$. It was inferred from the thermoelectric current $I_{\mathrm{th}}$, the zero-bias conductance $g$ and the thermal excitation $\delta T$ (best fit value) by equation (39). Again, the shape of $S$ is similar to the shape of $I_{\mathrm{th}}$ itself, but $S$ shows a faster increase in small fields. The maximum value is reached in a relatively small field, afterwards $S$ goes slowly back to zero. Only the data for $T_0 = 250$ mK and $T_0 = 500$ mK are shown here as the Seebeck coefficient found for $T_0 = 100$ mK was unreliable again. The signals are of the same order, but slightly larger than for the samples without EuS which might be induced by the larger spin polarization of the tunnel junction that was found for the EuS samples. An overview of the maximum values of the Seebeck coefficients for all samples and base temperatures is given in Table 5.2. Here, $S$ was averaged in a field region of 200 mT around the maximum.

At the end of this chapter, the thermoelectric signals of the samples with EuS are compared to each other and to the signal of sample FIS1 which had the same sample design. In Figure 5.10 the normalized thermoelectric coefficient $\eta$ is plotted as a

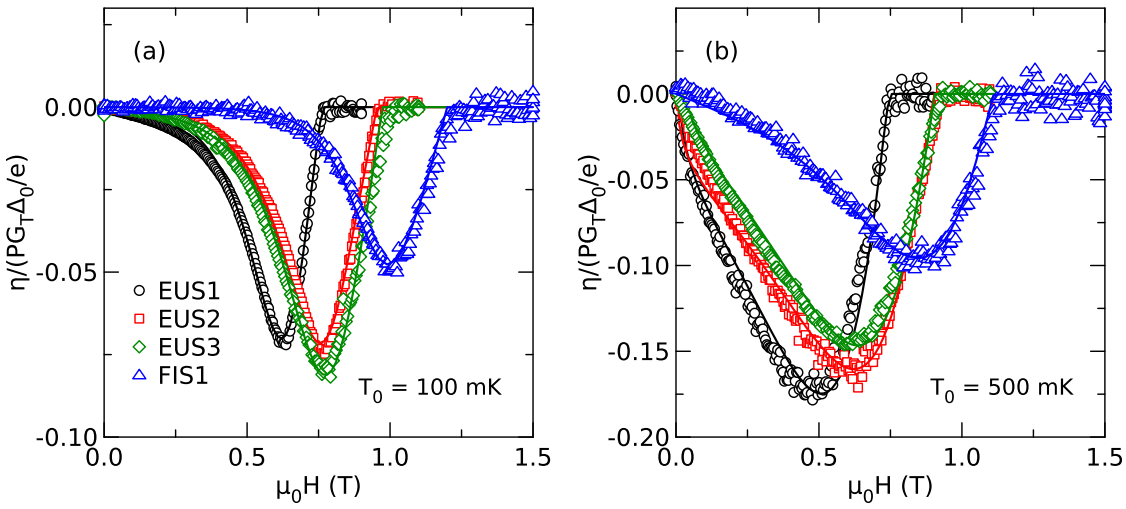


**Figure 5.10:** Comparison of the thermoelectric coefficient $\eta$ for the samples structured on top of EuS with sample FIS1. Shown is the normalized coefficient $\eta/(PG_{\mathrm{T}}\Delta/e)$ as a function of the magnetic field $\mu_0 H$ for base temperature (a) $T_0 = 100$ mK and (b) $T_0 = 500$ mK.

function of the magnetic field $\mu_0 H$ for all samples at $T_0 = 100$ mK (panel (a)) and at $T_0 = 500$ mK (panel (b)). To obtain comparable signals, $\eta$ had to be additionally normalized to the junction polarization $P$ here. First, it is noteworthy that the shape of the thermoelectric signal is similar for all samples. However, for the samples on top of EuS the overall signal amplitude is larger and the signals show up in a smaller magnetic field range compared to the sample FIS1. Thus, the contribution to the thermoelectric current in small fields is larger for the samples on top of EuS. This is especially visible at $T_0 = 500$ mK where the thermoelectric signals of the EuS samples are clearly larger in the small field region than that of FIS1. A slight deviation of the current is also observable for the different EuS samples, depending on the strength of the exchange field they had.

In conclusion, the main change that was induced by the europium sulfide substrates is the larger thermoelectric signal in the small field regime. The experiments show that with a further improvement of the EuS/Al interface, which probably also would improve the development of the exchange field, it might be possible to achieve large thermoelectric currents even near zero external field. This might eliminate the need to apply large magnetic fields and is therefore a further step towards sensitive thermometry of the electron temperature as well as towards efficient micro-refrigeration.

# 6 Nonlinear thermoelectric effects

In the following chapter the thermoelectric effect is studied in the nonlinear regime. Therefore, a voltage $V$ is applied to the junction in addition to the thermal excitation and the thermoelectric current is measured as a function of this voltage. Furthermore, generalized Onsager relations are introduced that allow us to relate the experimentally measured thermoelectric current to the heat current flowing across the junction. In this way the cooling power of the FIS junction can be evaluated and its performance can be compared to superconducting microrefrigerators based on NIS tunnel junctions [29, 31, 32]. The chapter is based on reference [86] where the data presented here are already published.

## 6.1 Generalized Onsager relations for the nonlinear regime

In the linear regime the Seebeck coefficient which relates the thermovoltage to the temperature difference and the Peltier coefficient which relates the heat flow to the current flow are linked to each other by Onsager relations [87, 88]. In the nonlinear regime, this is not the case anymore. To evaluate the heat transport in the nonlinear regime nevertheless, new theory was developed by Peter Machon and Wolfgang Belzig in which the Onsager relations are generalized. For this purpose, we have to come back to equation (27) which describes the charge current $I_\mathrm{T}$ into the superconductor. The heat current flowing out of the ferromagnet is related to $I_\mathrm{T}$ by

$$\begin{aligned} I_\mathrm{Q}(V,T,\delta T) &= I_\varepsilon(V,T,\delta T) - V I_\mathrm{T}(V,T,\delta T) \\ &= \frac{G_\mathrm{T}}{e^2}\int \left[N_+(\varepsilon) + P N_-(\varepsilon)\right](\varepsilon - eV)\left[f_0(\varepsilon - eV, T+\delta T) - f_0(\varepsilon, T)\right] d\varepsilon. \end{aligned} \tag{44}$$

Because the charge current is now regarded as a nonlinear function of $\delta T$ and $V$, it is also useful to generalize the thermoelectric coefficient $\eta$ to

$$\eta(V,T,\delta T) = \overline{T}\frac{\partial I_\mathrm{T}}{\partial \delta T}. \tag{45}$$

The physics of the nonlinear thermoelectric effect which is generated due to the additional voltage $V$ can be understood by looking at the scheme depicted in Figure 6.1. As we saw before the linear thermoelectric effect is a consequence of the breaking of the electron-hole symmetry. Applying a finite bias $V$ across a superconducting tunnel junction also creates an asymmetry between forward and backward flowing currents as it shifts the chemical potential in the metallic electrode with respect to the Fermi level. Hence, the resulting net current is temperature dependent and a thermal excitation $\delta T$ across the junction leads to thermoelectric effects. It should be noted that the nonlinear effect is also visible in a normal metal superconductor tunnel junction as the polarization is not crucial anymore for the symmetry breaking.

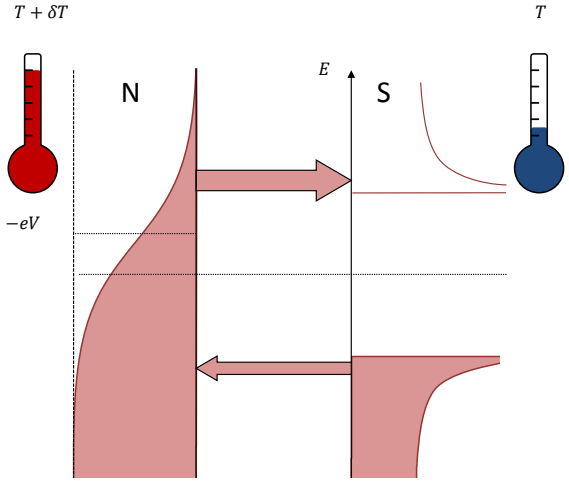


**Figure 6.1:** Scheme of the generation of the nonlinear thermoelectric effect in a NIS (or FIS) junction.

To understand the relation of the experimental accessible $\eta(V)$ to the thermal transport in superconductor hybrid structures the heat current $I_\mathrm{Q}$ has to be evaluated. It is related to $\eta$ by (a more detailed derivation can be found in reference [86])

$$I_\mathrm{Q}(V,T,0) = \int \left[\eta(V,T,0) - I_\mathrm{T}(V,T,0)\right] dV. \tag{46}$$

By using equation (46) we can directly evaluate the experimental data.

## 6.2 Experimental results

In Figure 6.2 $\eta$ is plotted as a function of the voltage $V$ at $T_0 = 100$ mK for several magnetic fields $\mu_0 H$. As described above, the nonlinear thermoelectric effect is observed in the ferromagnetic samples (panel (a)) as well as in the nonmagnetic sample (panel (b)). Here, the scale of $\eta$ is around two orders of magnitude higher than for the linear case $\eta(V = 0)$. Therefore, the contribution of the linear effect at $V = 0$ can not be resolved in Figure 6.2 and the signals behave equally for both samples.

The signals exhibit peaks near the gap voltage $E_\mathrm{G}/e$ which are largest in zero magnetic field. This observation is in contrast to the linear effect where the signals exhibited their maximum value at high magnetic fields, but becomes clear by looking again at Figure 6.1. As the energy asymmetry is driven by the voltage $V$ now, it becomes largest just when the chemical potential is tuned near the energy gap. Thus, the largest signals are found under this condition and the effect is largest for $\mu_0 H = 0$ where the DOS in the superconductor is sharpest. In higher magnetic fields the peaks of $\eta$ are broadened due to pair breaking effects and exhibit a double peak structure due to the Zeeman splitting both for positive and negative voltages.

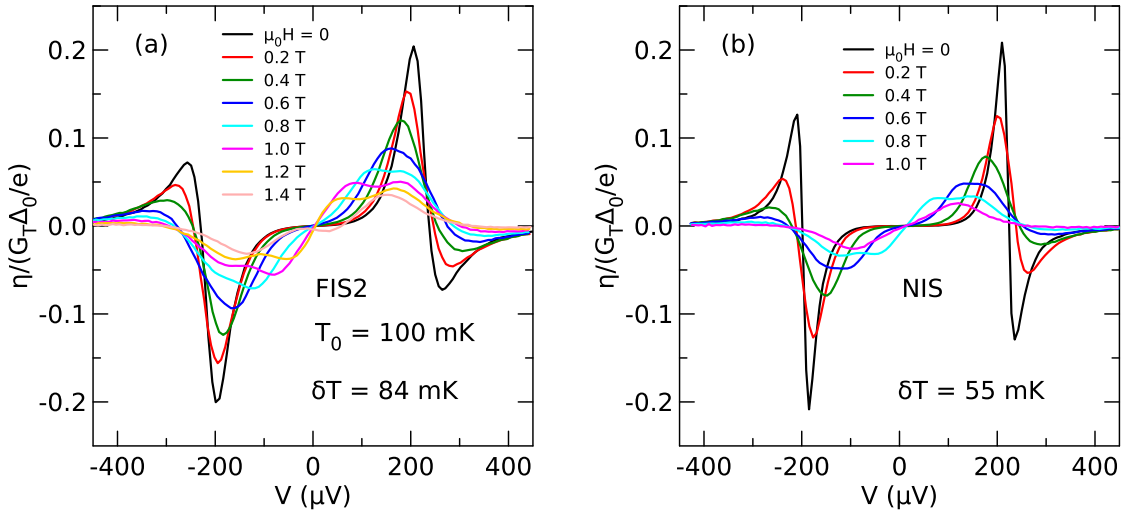


**Figure 6.2:** Thermoelectric coefficient $\eta$ as a function of the voltage $V$ applied across the contact for different magnetic fields $\mu_0 H$. The base temperature here was $T_0 = 100$ mK. Shown are data from sample (a) FIS2, (b) NIS.

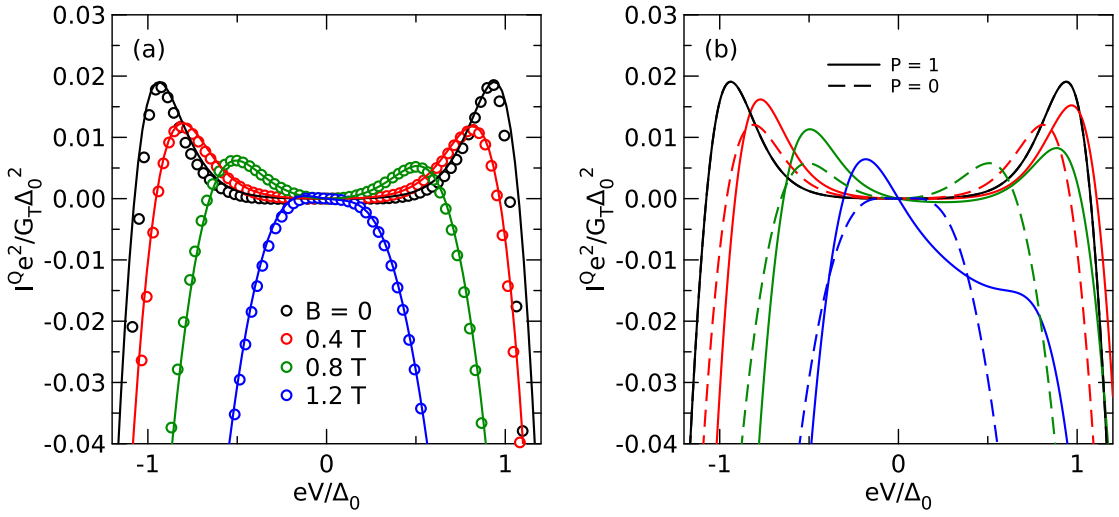


**Figure 6.3:** (a) Normalized cooling power $I_{\mathrm{Q}} e^2/G_{\mathrm{T}}\Delta_0^2$ as a function of the normalized voltage $eV/\Delta_0$ for several magnetic fields $\mu_0 H$. (b) Theoretical cooling power for the same device assuming $P = 0$ (non-magnetic junction) and $P = 1$ (perfectly polarized junction).

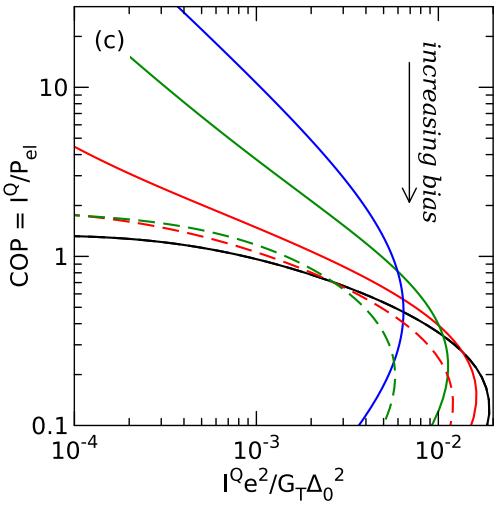


**Figure 6.4:** Predicted coefficient of performance $COP$ as a function of the normalized cooling power for the same parameters as in Figure 6.3(b) and $V < 0$.

We can now evaluate the heat current. In Figure 6.3(a) the prediction for the normalized cooling power $I_{\mathrm{Q}}$ is plotted. It is calculated from the thermoelectric coefficient $\eta(V, 0)$ and the dc current $I_{\mathrm{T}}(V, 0)$ of sample FIS2 by equation (46). The experimental data are represented by symbols, while the solid lines are fits to equation (44) directly. The good agreement of the data and fits shows that it is possible to infer the heating power from the experimentally determined coefficient $\eta$. It should be mentioned that the analysis predicts the cooling power for $\delta T = 0$, while the actual cooling power under finite $\delta T$ will be smaller due to the back-flow of heat via the thermal conductance of the junction. In zero field $\mu_0 H = 0$, the cooling power has the typical bias dependence of a NIS microrefrigerator [28]. The cooling power is positive near the gap voltage and reaches a maximum for $eV \approx \Delta_0$ (in zero field and at low temperature $\Delta_0 \sim E_{\mathrm{G}}$). In higher fields, the maximum of the cooling power decreases and shifts to smaller voltages until it vanishes completely. The cooling effect due to the linear thermoelectric effect at $V = 0$ is too small to be resolved due to the small polarization $P = 0.08$ of the junction.

To evaluate the potential of FIS tunnel junctions as microrefrigerators, in Figure 6.3(b) the cooling power is plotted for an idealized ferromagnetic junction with $P = 1$. All other parameters were taken from the fits in panel (a). For comparison also the expected power for a NIS cooler ($P = 0$) with the same properties is plotted as dashed line for each magnetic field. As expected, there is no difference between the NIS and the FIS cooler for $\mu_0 H = 0$. At finite magnetic field, the FIS cooler exhibits a contribution from the linear effect, so that it outperforms the NIS cooler at smaller bias.

By following reference [89], one can define the coefficient of performance for a cooler

as the ration

$$COP = \frac{I_{\mathrm{Q}}}{P_{\mathrm{el}}} = \frac{I_{\mathrm{Q}}}{I_{\mathrm{T}} V} \tag{47}$$

of the cooling power and the electric input power of the device. It is plotted in Figure 6.4 as a function of the cooling power, calculated with the parameters of Figure 6.3(b) for $V < 0$. We see that the FIS cooler has a better efficiency over a wide range of cooling powers. So, with an increase of polarization it seems possible to build improved cooling devices. For this purpose, the use of spin-filter tunneling barriers [35] seems promising and the linear thermoelectric effect might become useful for cooling applications.

# 7 Hanle effect

In this section, first attempts of an experiment which is based on the spin transport measurements of Florian Hübler [9] and Michael Wolf [11] are presented. As known from these experiments, in a spin-split superconductor the spin imbalance which is generated at a certain contact has a surprisingly large relaxation length and can be detected in a nonlocal measurement geometry by a spin-polarized detector contact over distances of several $\mu m$. So far, the spin transport has been investigated experimentally [9–11, 13] only for the case of parallel alignment of the magnetization $\mathbf{M}$ of the electrodes and the applied magnetic field $\mathbf{H}$. Here, we also want to expand the study of the spin transport for the case of perpendicular alignment of $\mathbf{M}$ and $\mathbf{H}$. The chapter starts with a brief summary of recent theory [39] for the case of noncollinear magnetization alignment. Then follows a description of the sample design and the measurement technique used here. The results of the spin transport measurements are divided into two sections. One in which measurements in the normal state of the aluminum are discussed and one in which results derived in the superconducting state of the aluminum are presented. In both cases, measurements in the perpendicular magnetic configuration $\mathbf{M} \perp \mathbf{H}$ are compared to measurements with parallel alignment $\mathbf{M} \parallel \mathbf{H}$.

## 7.1 Introduction

The spin Hanle effect is generated when the spin quantization axis of a charge carrier and the applied magnetic field have a noncollinear orientation. In the extreme case when both have a perpendicular orientation to each other the spin orientation will precess around the magnetic field orientation with the Larmor frequency

$$\omega_{\mathrm{L}} = \frac{g_{\mathrm{J}} \mu_{\mathrm{B}} \mu_0 H}{\hbar} \tag{48}$$

where $g_{\mathrm{J}}$ describes the Land'e factor of the magnetic moment $J$. The effect was demonstrated for electronic charge carriers in metallic structures by Johnson and Silsbee [40] in 1985 by studying the nonlocal resistance of a spin valve geometry. Since that time it has been established in several experiments and different materials [41–44] for testing the spin coherence. However, so far the effect has not been demonstrated in superconducting structures yet, although it is interesting here in so far as superconductors provide long spin relaxation times in the presence of a spin-splitting field [9–11, 13].

For theoretical studies it is necessary to express the spin imbalance in the superconductor mathematically. This is done in analogy to the charge and energy imbalance which is created by the unpolarized injection of quasiparticles. Like in a normal metal, the spin-polarized current of a ferromagnet creates a difference in the occupation of spin-up and spin-down states in the quasiparticle density of states. Hence, it is necessary to introduce different occupation numbers $f_\sigma$ for each spin kind. Similar to the energy

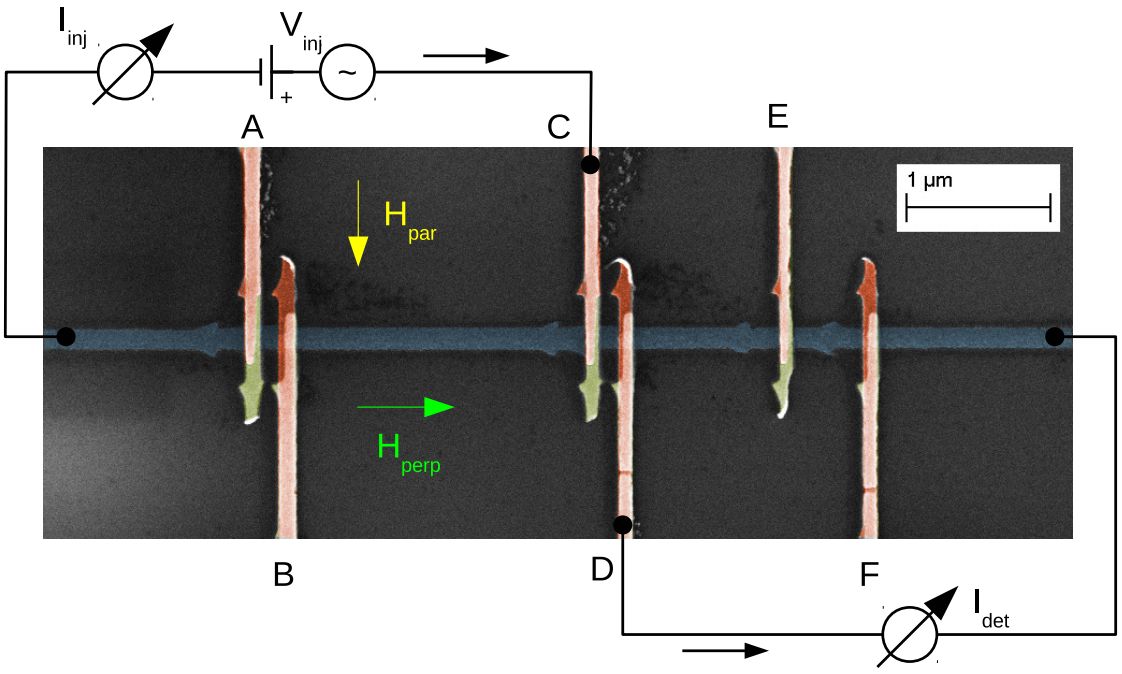


**Figure 7.1:** Colorized scanning electron microscopy image of sample FIS5. The aluminum strip is colored in blue while the iron electrodes are colored in dark red. To reduce the film resistance the iron electrodes are covered by a copper film (light red areas). The artifacts of bare copper are colored in green. Additionally, the schemes for the measurements of the differential local conductance $g_{\mathrm{loc}} = dI_{\mathrm{inj}}/dV_{\mathrm{inj}}$ and for the differential nonlocal conductance $g_{\mathrm{nl}} = dI_{\mathrm{det}}/dV_{\mathrm{inj}}$ are depicted in the SEM picture.

imbalance where the nonequilibrium can be expressed by a effective temperature $T^*$ (see section 2.4), the inequality of the occupation numbers can be described by the change of the chemical potentials $\mu_\uparrow$ and $\mu_\downarrow$ for spin-up and spin-down quasiparticles respectively [90]. It is expressed by additional transverse and longitudinal spin imbalance modes [91, 92]. For the case of noncollinear magnetization, two modes for every Cartesian axis exist [39] which follow coupled differential equations. One expects the spin Hanle oscillations to be visible in the nonlocal signal which was used by Florian Hübler [15] and Michael J. Wolf [11] for studying the spin relaxation in superconducting aluminum.

## 7.2 Sample design and measurement setup

The samples were again fabricated with the use of e-beam lithography and shadow evaporation technique as it was described in section 3.1. To study the spin transport the design of them was changed compared to the thermoelectric samples. Figure 7.1 shows a colorized scanning electron microscopy image of the inner part of sample FIS5 which was used for the spin Hanle measurements. The sample consists of an aluminum wire (blue) with a film thickness $t_{\mathrm{Al}} \approx 25$ nm and six iron electrodes (dark red) with

a thickness $t_{\mathrm{Fe}} \approx 20$ nm in various distances $d = 0.15 - 4.3$ $\mu$m from each other. To reduce the lead resistance, the iron electrodes were covered with a thin copper layer with thickness $t_{\mathrm{Cu}} \approx 25$ nm. Overlaying copper artifacts which formed due to the use of shadow evaporation technique are colorized in green. In the following the six contacts shall be denominated as contact A-F, starting with A from left to right.

Additionally depicted in Figure 7.1 is the scheme for the measurements of the differential conductance. The local differential conductance $g_{\mathrm{loc}} = dI_{\mathrm{inj}}/dV_{\mathrm{inj}}$ was measured with standard lock-in technique as described in chapter 3.3. The nonlocal current $I_{\mathrm{det}}$ was detected simultaneously by a second circuit with an additional lock-in amplifier. It is considered as positive for current flowing from the superconductor into the ferromagnet. From the ac part of $I_{\mathrm{det}}$ and $V_{\mathrm{inj}}$ the differential nonlocal conductance $g_{\mathrm{nl}} = dI_{\mathrm{det}}/dV_{\mathrm{inj}}$ was calculated. To characterize the sample, first the spin transport experiment [9] with the parallel magnetic configuration $\mathbf{M} \parallel \mathbf{H}$ was repeated. The direction of the in-plane field for this configuration is indicated in the SEM image by the yellow arrow $H_{\mathrm{par}}$. Subsequently, the sample was warmed up, the sample holder was turned by 90° and the sample was cooled down again. Thus, the magnetic field now was in parallel to the aluminum wire and perpendicular to the electrodes, this is indicated by the green arrow $H_{\mathrm{perp}}$ in the SEM image. So the magnetic field direction was perpendicular to the magnetization of the iron electrodes $\mathbf{M} \perp \mathbf{H}$.

As depicted in Figure 7.1 the circuits for local and nonlocal measurements were completely separated with the intention to avoid parasitic contributions. However, this led to the disadvantage that the local conductance had to be measured in a two-probe fashion with the resistance of the leads in series. But since the typical wire resistances were in the range of a few 100 Ω, they were one order of magnitude smaller than the contact resistance and we can assume that the main part of the voltage drops across the junction and that we still mainly measure the conductance of the junction with this measurement setup.

In the normal state of the aluminum, the measurements were done with an ac-resistance bridge which provided a better signal to noise ratio. Here the local $R_{\mathrm{loc}} = V_{\mathrm{inj}}/I_{\mathrm{inj}}$ and nonlocal $R_{\mathrm{nl}} = V_{\mathrm{det}}/I_{\mathrm{inj}}$ resistances were measured directly.

## 7.3 Spin transport in the normal state

First, the spin transport in the normal state is discussed. For the measurements the sample was cooled down to liquid helium temperature $T_0 = 4.2$ K. In the parallel magnetic field configuration ($\mathbf{M} \parallel \mathbf{H}$) spin valve experiments were done in the nonlocal measurement configuration. The technique was developed by Johnson and Silsbee [40] and further established by Jedema et al. [41, 42]. A spin-polarized current $I_{\mathrm{inj}}$ was applied at the injector electrode, so that a difference of the chemical potentials for electrons of both spin kinds was induced in the normal metal [40, 93, 94]. The spin

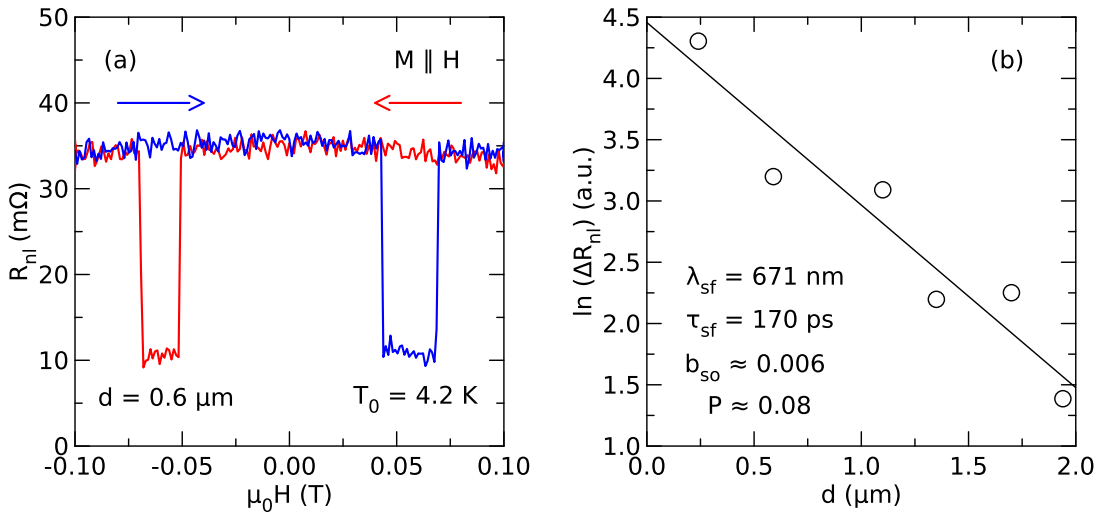


**Figure 7.2:** Nonlocal resistance $R_{\mathrm{nl}}$ at $T_0 = 4.2$ K with the magnetic field $H$ applied in parallel to the electrodes. (a) $R_{\mathrm{nl}}$ as a function of $\mu_0 H$ for both sweep directions (indicated by the arrows) and a contact distance $d = 0.6$ $\mu$m. (b) Logarithm of $\Delta R_{\mathrm{nl}}$ as a function of the contact distance $d$. The solid line shows a fit according to equation (49).

imbalance then diffused along the wire and was detected by measuring the resulting voltage $V_{\mathrm{det}}$ at the detector electrode.

In Figure 7.2(a) the nonlocal resistance $R_{\mathrm{nl}} = V_{\mathrm{det}}/I_{\mathrm{inj}}$ is shown as a function of the applied magnetic field $\mu_0 H$ for the contact distance $d = 0.6$ $\mu$m. The magnetic field was aligned in parallel to the iron electrodes and magnetic field sweeps were done with directions from negative to positive fields (blue curve) and reverse (red curve). One observes that after crossing zero field the resistance exhibits first a jump to a smaller value at $|\mu_0 H| \approx 50$ mT and another jump back to the original value at $|\mu_0 H| \approx 70$ mT. These jumps can be identified with a switch of the magnetization of both iron electrodes from the parallel state into the antiparallel one and vice versa. From the curves the difference $\Delta R_{\mathrm{nl}}$ of the nonlocal resistance for both states can be extracted.

In Figure 7.2(b) the logarithm of $\Delta R_{\mathrm{nl}}$ is plotted as a function of the contact distance $d$. The solid line shows a fit to the model of Jedema et al. [42] for the resistance difference in a mesoscopic spin valve structure with tunnel junctions

$$\Delta R = P^2 \frac{\lambda_{\mathrm{sf}}}{\sigma \mathcal{A}} \exp(-d/\lambda_{\mathrm{sf}}) \tag{49}$$

with the spin polarization $P$, the spin-flip length $\lambda_{\mathrm{sf}}$, the conductivity $\sigma$ and the cross section $\mathcal{A}$ of the aluminum wire. By the fit we extracted $P = 0.08 \pm 0.02$ and $\lambda_{\mathrm{sf}} = 671 \pm 105$ nm. The value for the spin polarization of the junction is consistent with the values for the spin polarization extracted by local conductance measurements in the superconducting state which we showed in the preceding chapters. Also the value

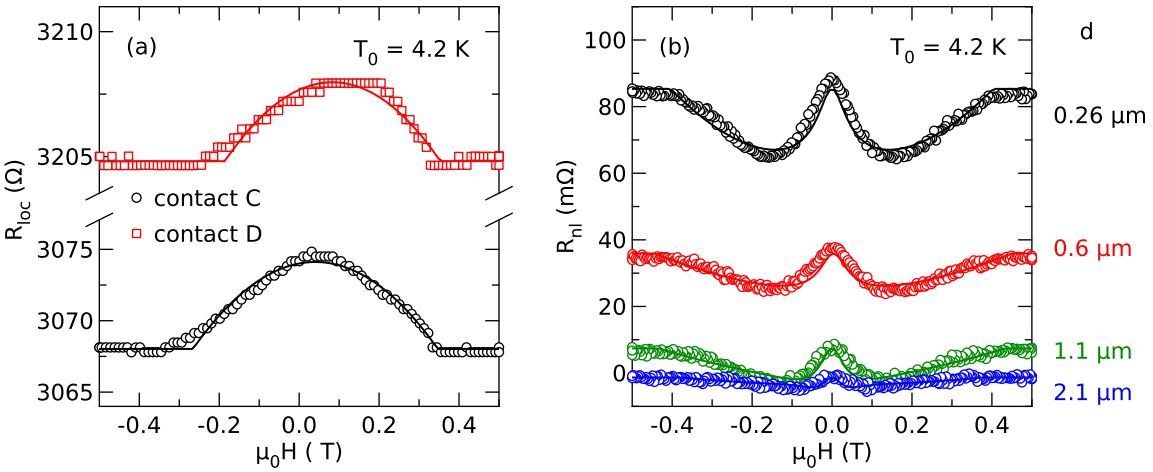


**Figure 7.3:** Resistance measurement in the perpendicular configuration $\mathbf{M} \perp \mathbf{H}$ at $T_0 = 4.2$ K. (a) Local resistance $R_{\mathrm{loc}}$ of contact C and D as a function of the magnetic field $\mu_0 H$. (b) Nonlocal resistance $R_{\mathrm{nl}}$ as a function of $\mu_0 H$ for several contact distances $d$.

for the spin diffusion length is in reasonable agreement with literature values [9, 42] for aluminum structures of similar dimensions. From this value we were able to infer the spin-flip time $\tau_{\mathrm{sf}} = \lambda_{\mathrm{sf}}^2/D = 170$ ps and the spin-orbit strength $b_{\mathrm{so}} \approx \hbar/(3\tau_{\mathrm{sf}}\Delta_0) \approx 0.006$. This value for $b_{\mathrm{so}}$ is also consistent with the values found for the thermoelectric samples (compare to Table 4.1 and Table 5.1).

Next, we turn to the perpendicular magnetic configuration ($\mathbf{M} \perp \mathbf{H}$). In this configuration measurements of the anisotropic magnetoresistance (AMR) were done. The AMR was discovered in the middle of 19th century by William Thomson [95]. It describes the change of the resistance of a ferromagnetic material [96]

$$R(\phi) = R_{\perp} + (R_{\parallel} - R_{\perp}) \cdot \cos^2(\phi). \tag{50}$$

depending on the angle $\phi$ in between of the magnetization direction of the material and the current direction, so that it is a tool to investigate the direction of the magnetization as a function of the magnetic field. Under the assumption that the iron wire has a homogeneous magnetization, the angle $\phi$ can be calculated within the Stoner-Wolfarth model [97]. This model describes the competition of the anisotropy of a ferromagnet which prefers magnetization in a certain direction and the applied field which tries to align the magnetization direction into the field direction. For the case $\mathbf{M} \perp \mathbf{H}$, $\phi$ is given by

$$\phi = \arccos\left(\frac{H - H_{\mathrm{off}}}{H_{\mathrm{sat}}}\right) \tag{51}$$

where $H_{\mathrm{off}}$ is the offset of the field due to the magnetic hysteresis of the ferromagnetic wire and $H_{\mathrm{sat}}$ is the saturation field above which $\mathbf{M}$ is completely rotated in direction of $\mathbf{H}$.

In Figure 7.3(a) AMR measurements for the contacts C and D in the middle of the sample (see Figure 7.1) are shown. The local resistance $R_{\mathrm{loc}}$ is plotted as a function of the magnetic field $\mu_0 H$. Due to the sample design it had to be measured in a 3-probe fashion. Thereby, the resistance of the iron wire was measured in series with the resistance of the complete lead and the resistance of the tunnel junction, so that the total resistance is three orders of magnitude higher than the AMR signal. As expected, a maximum is visible at zero field where $\mathbf{M}$ is parallel to the current direction. When $H$ is increased the resistance slightly decreases while the magnetization is turned into the field direction by the increasing field. A constant value is reached for $H > H_{\mathrm{sat}}$ when the magnetization is aligned completely within the field and therefore in perpendicular to the current direction. The fit according to equation (50) exhibits a small offset $H_{\mathrm{off}} \approx 0.06$ T and the saturation field $\mu_0 H_{\mathrm{sat}} \approx 0.3$ T. If we neglect the hysteresis effect, we can say that strictly speaking $\mathbf{M} \perp \mathbf{H}$ is only valid for $H = 0$.

Next, we investigated the spin Hanle effect in the normal state. Therefore, the nonlocal measurement configuration was used. In Figure 7.3(b) the nonlocal resistance $R_{\mathrm{nl}}$ is plotted as a function of the magnetic field $\mu_0 H$ for several contact distances $d$. For all distances the signal exhibits a maximum at $\mu_0 H = 0$ and one dip at $|\mu_0 H| \approx 0.15$ T in positive and negative field respectively. The dip occurs at the field where the spin projection of the injected electrons is rotated in the opposite direction just at the detector electrode, in this case it is antiparallel to the magnetization of the detector electrode. As the spin imbalance relaxes with increasing contact distance, the signal of the Hanle oscillations decreases. Following the work of Jedema et al. [42], we can model the nonlocal resistance

$$R_{\mathrm{nl}}(H_{\mathrm{perp}}) = \frac{P^2 D}{\sigma \mathcal{A}} \int_0^\infty P(t) \cos(\omega_{\mathrm{L}} t) \exp(-t/\tau_{\mathrm{sf}}) dt \tag{52}$$

where the distribution function

$$P(t) = \frac{1}{\sqrt{4\pi D t}} \exp[-L^2/(4Dt)] \tag{53}$$

is introduced. This function is proportional to the number of electrons that, once injected, arrive at the detector after the diffusion time $t$. Note that equation (52) reduces to equation (49) for the case $\omega_{\mathrm{L}} = 0$. In Figure 7.3 (b) fits to equation (52) are shown which were calculated by using the parameters extracted from the spin valve measurements. The only free fit parameter here was the saturation field which was extracted to be $\mu_0 H_{\mathrm{sat}} = 0.4$ T. By adjusting this parameter we found good agreement between the data and the fits.

## 7.4 Spin transport in the superconducting state

Now we turn to the measurement in the superconducting state which were done at base temperature $T_0 = 50$ mK. Since the strength of the nonlocal signals depends on

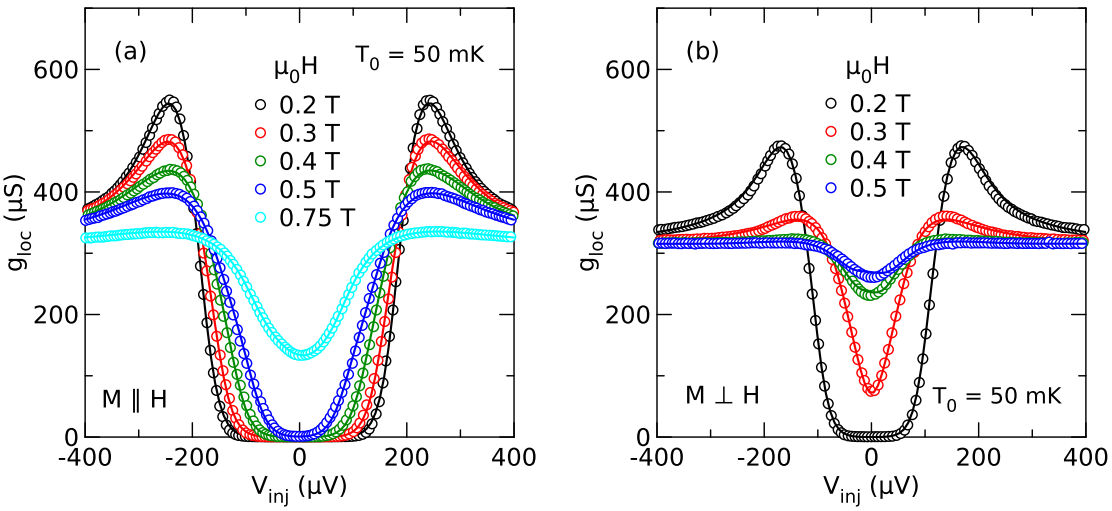


**Figure 7.4:** Local conductance $g_{\mathrm{loc}}$ of contact C as a function of the injector bias $V_{\mathrm{inj}}$ for several magnetic fields $\mu_0 H$ at base temperature $T_0 = 50$ mK. Shown are data measured in (a) parallel $\mathbf{M} \parallel \mathbf{H}$ and (b) perpendicular $\mathbf{M} \perp \mathbf{H}$ field alignment. The solid lines are fits according to equation (54).

the contact distance here only data of the contacts C and D which formed the closest contact pair are presented. A detailed study of the distance dependence of the nonlocal spin imbalance signal can be found elsewhere [9, 11].

First, measurements of the local conductance $g_{\mathrm{loc}}$ which enable the extraction of the characteristic junction properties are discussed. In Figure 7.4, $g_{\mathrm{loc}}$ is shown as a function of the injector voltage $V_{\mathrm{inj}}$ for several magnetic fields $\mu_0 H$. The data in panel (a) were measured for $\mathbf{M} \parallel \mathbf{H}$. By the voltage dependence in small fields we can identify the good quality of the tunnel junction as the conductance shows the form one expects from BCS theory. Noteworthy is that in high fields the Zeeman splitting is not visible in the conductance here, in contrast to the conductance measurements which were presented so far. The reason is the larger thickness of the aluminum wire here, so that the pair breaking effect of the field dominates over the spin-splitting effect. To fit the data the series resistance $R^F_{\mathrm{inj}}$ of the injector electrode had to be taken into account due to the two probe measurement configuration. So, the bias which actually dropped across the junction was $V_{\mathrm{T}} = V_{\mathrm{inj}} - I_{\mathrm{inj}} R^F_{\mathrm{inj}}$ and the implicit equation

$$I_{\mathrm{inj}} = I_{\mathrm{T}} \left( V_{\mathrm{inj}} - I_{\mathrm{inj}} R^F_{\mathrm{inj}} \right) \tag{54}$$

had to be solved. Here, $I_{\mathrm{T}}(V)$ is given by equation (27). Since simultaneous fits of the normal conductance $G_{\mathrm{T}}$ of the junction and $R^F_{\mathrm{inj}}$ did not give proper values, the series resistance was estimated to be $R^F_{\mathrm{inj}} = 300\ \Omega$ which is a reasonable value for a short iron wire of this dimension overlaid with a thin copper film. For the fits the values $P = 0.08$ and $b_{\mathrm{so}} \approx 0.01$ extracted from the normal state measurements were used. The pair potential $\Delta$, the pair-breaking parameter $\Gamma$ and $G_{\mathrm{T}}$ were left as free fit parameters.

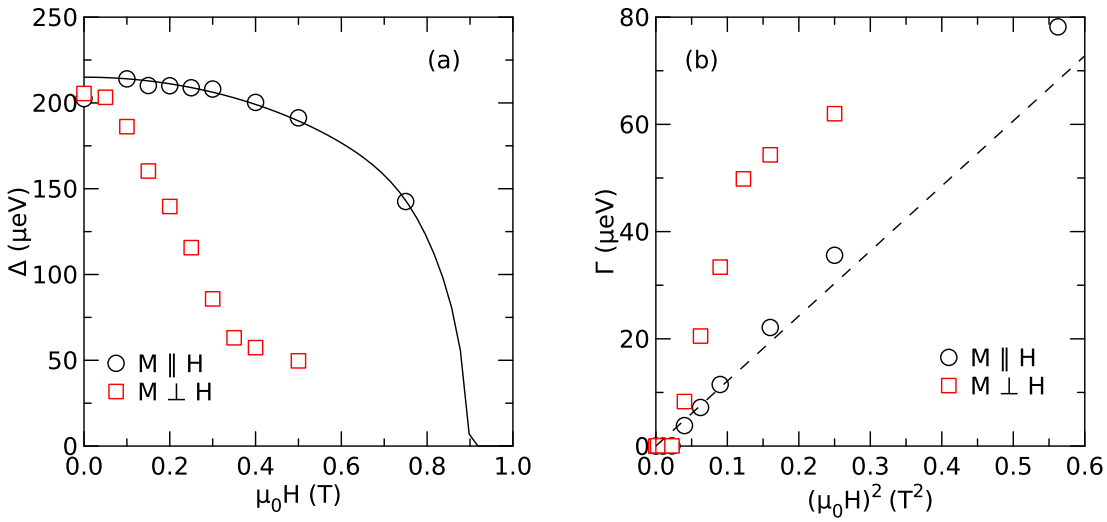


**Figure 7.5:** Fit parameter of the local conductance shown in Figure 7.4. (a) Pair potential $\Delta$ as a function of the magnetic field $\mu_0 H$. (b) Pair-breaking parameter $\Gamma$ as a function of $(\mu_0 H)^2$. The lines in both panels show fits described in the text.

In Figure 7.4(b) the local conductance of junction C is shown for the perpendicular case ($\mathbf{M} \perp \mathbf{H}$). A comparison to the parallel case in panel (a) shows that the superconductivity is destroyed much faster here. The energy gap is already clearly reduced for $\mu_0 H = 0.2$ T and even completely closed for $\mu_0 H = 0.4$ T. Fits according to equation (54) with $G_\mathrm{T}, \Delta$ and $\Gamma$ as free fit parameters are shown as solid lines.

The extracted parameters are plotted in Figure 7.5 for both magnetic configurations. In panel (a) the pair potential $\Delta$ is shown as a function of the magnetic field $\mu_0 H$. In the parallel case $\mathbf{M} \parallel \mathbf{H}$ one observes the usual field dependence. A fit (solid line) according to the self consistency equation is shown for a better orientation. From the fit the parameters $\Delta_0 = 215$ $\mu$eV and $\mu_0 H_{\mathrm{c,orb}} = 0.94$ T were extracted. The latter one which describes the critical field in the absence of spin splitting is in good agreement with the critical field $\mu_0 H_\mathrm{c} = 0.96$ T read from the zero-bias conductance. This illustrates that in aluminum wires of this thickness orbital effects of the magnetic field dominate over the spin-splitting effect. For the case $\mathbf{M} \perp \mathbf{H}$ one finds a different behavior for $\Delta$. Here the pair potential is reduced drastically even in small fields. At $\mu_0 H = 0.3$, where $\Delta$ is already strongly suppressed, the data exhibit a kink. Due to the strong suppression in small fields, it was not possible to fit $\Delta$ to the self consistent equation and one fails to determine $\mu_0 H_{\mathrm{c,orb}}$ for the perpendicular case.

The pair-breaking parameter $\Gamma$ is plotted in Figure 7.5(b) as a function of $(\mu_0 H)^2$. For $\mathbf{M} \parallel \mathbf{H}$ it follows the theory of pair breaking, equation (35), which is indicated by the dashed line. We see that for $\mathbf{M} \perp \mathbf{H}$ the pair breaking is strongly enhanced. By a close look at the data, one finds a kink in the data at $(\mu_0 H)^2 = (0.3\ \mathrm{T})^2 = 0.09\ \mathrm{T}^2$ also here.

So, both fit parameter show that the superconductivity is almost completely suppressed

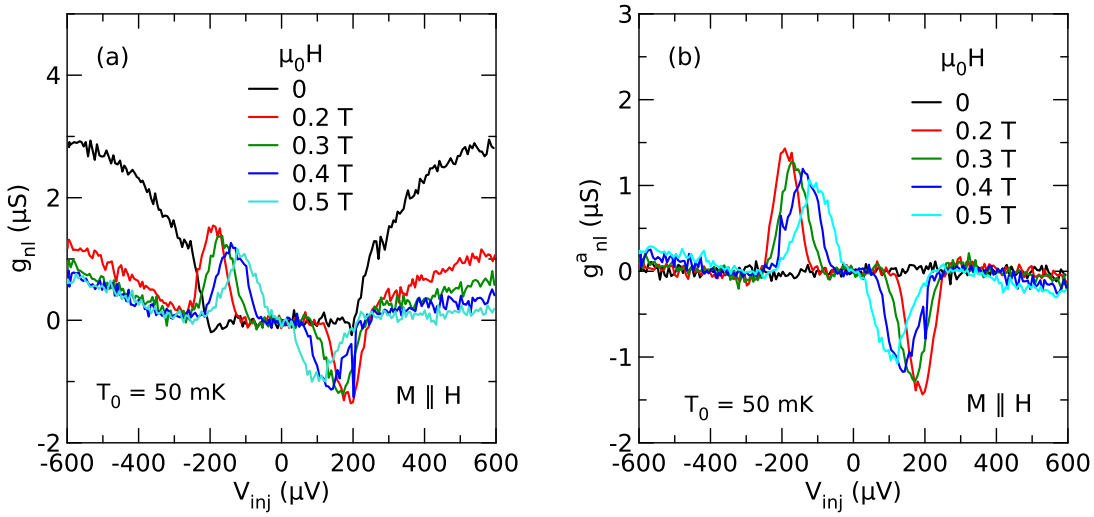


**Figure 7.6:** (a) Nonlocal differential conductance $g_{\mathrm{nl}}$ as a function of the injector voltage $V_{\mathrm{inj}}$ for several magnetic fields $\mu_0 H$ at base temperature $T_0 = 50$ mK. (b) Asymmetric part $g^a_{\mathrm{nl}}$ as a function of $V_{\mathrm{inj}}$. Both panels show measurements in the parallel magnetic field configuration. As injector contact C was used, as detector contact D.

on a field scale of 0.3 T for the perpendicular magnetic configuration. As we saw from the AMR measurements, this is exactly the field scale on which the magnetization of the electrode is rotated in parallel to the field direction. We therefore assume that the suppression of the superconductivity is induced by the pair breaking effects of the fringing fields of the iron electrodes. As the magnetization of the electrodes is rotated, these effects are strengthened and the superconductivity is suppressed. So, the field regime where the spin Hanle precession of the quasiparticle spin is detectable, is restricted to a small range.

Finally, the nonlocal conductance $g_{\mathrm{nl}}$ is discussed for both magnetic field configurations. In Figure 7.6(a) $g_{\mathrm{nl}}$ is shown as a function of the injector voltage $V_{\mathrm{inj}}$ for several magnetic fields in the parallel configuration $\mathbf{M} \parallel \mathbf{H}$. In zero field $\mu_0 H = 0$ the signal is zero in the sub-gap regime $|V_{\mathrm{inj}}| \lesssim 200\ \mu$V and shows a monotonic increase for higher voltages. This is induced by the charge imbalance (see section 2.4) and is symmetric in bias. In higher fields this part of the signal is decreasing. Instead, an asymmetric signal develops around $|V_{\mathrm{inj}}| \approx 200\ \mu$V with a positive conductance for negative voltages and vice versa. This part of the signal is caused by the spin imbalance in the superconductor and a closer look is provided by calculating the asymmetric part of the conductance

$$g^a(V) = \frac{1}{2} \cdot (g(V) - g(-V)). \tag{55}$$

This part is shown in Figure 7.6(b). The signal is largest for $\mu_0 H = 0.2$ T. In higher fields it slightly reduces and broadens. Additionally it is shifted towards smaller voltages

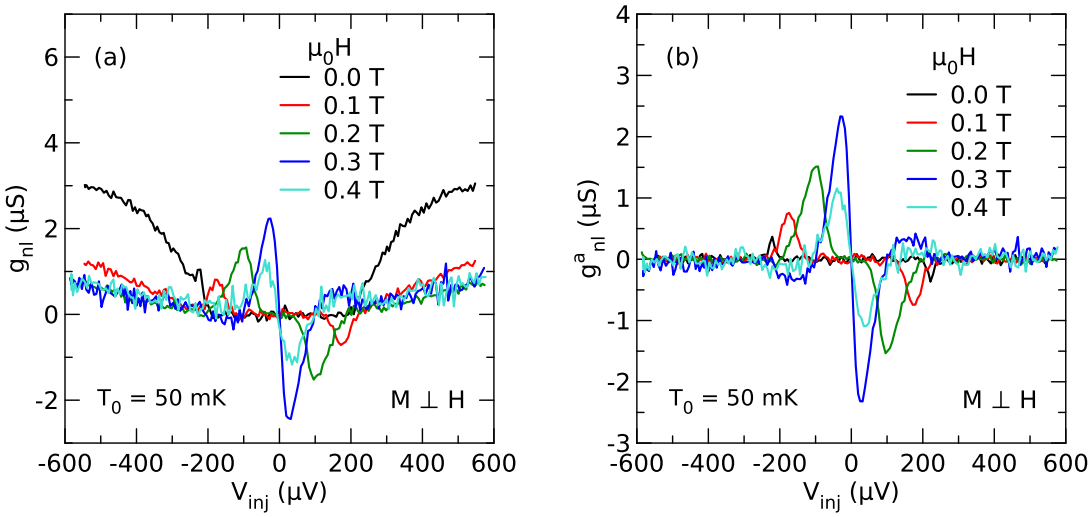


**Figure 7.7:** (a) Nonlocal differential conductance $g_{\mathrm{nl}}$ as a function of the injector voltage $V_{\mathrm{inj}}$ for several magnetic fields $\mu_0 H$ at base temperature $T_0 = 50$ mK. (b) Asymmetric part $g^a_{\mathrm{nl}}$ as a function of $V_{\mathrm{inj}}$. Both panels show measurements in the perpendicular magnetic field configuration. As injector contact C was used, as detector contact D.

as the energy gap also decreases. Altogether this is the behavior that was reported in the literature [9–11].

In Figure 7.7(a) the nonlocal differential conductance is plotted for the nonparallel configuration $\mathbf{M} \perp \mathbf{H}$. We first note that the charge imbalance signal at $|V_{\mathrm{inj}}| > 200\ \mu$V has the same behavior and the same quantity as in the parallel case. In Figure 7.7(b) the asymmetric part $g^a_{\mathrm{nl}}$ of the nonlocal conductance is plotted as a function of $V_{\mathrm{inj}}$. One also observes the asymmetric spin signal for $\mathbf{M} \perp \mathbf{H}$, but with a different magnetic field dependence. Here, the signal is small for small fields and it increases up to $\mu_0 H = 0.3$ T where it reaches its maximum. In higher fields it then decreases again. The behavior of the nonlocal signal can be explained as the detector electrode measures the spin projection in the direction of its magnetization $\mathbf{M}$. The nonlocal signal increases while the direction of $\mathbf{M}$ is rotated by the field for $\mu_0 H < 0.3$ T. So, we see that the asymmetric signal is dominated by the spin imbalance mode that lies in the direction of the magnetization of the electrodes.

Besides this effect, spin Hanle oscillation could not be identified in the nonlocal conductance for this sample. Further attempts are necessary and the use of europium sulfide substrates seems favorable for this purpose as these induce an exchange field. Thus, the spin splitting is boosted and one can avoid the need of large magnetic fields which destroy the superconductivity by the fringing field of the electrodes.

# 8 Summary

In the main part of this work the first experimental observations of thermoelectric effects in superconductor/ferromagnet tunnel junctions were treated.

For this purpose, samples were fabricated which had a six-probe tunnel junction, so that thermoelectric current could be measured simultaneously to the generation of a temperature gradient across the junction. For the measurements a second harmonic detection technique was established and during the experiments it was checked that the results derived by this technique were real and not induced by spurious contributions. The successful detection of thermoelectric currents showed that the breaking of the electron-hole symmetry of the conductance in spin-polarized superconductor tunnel junctions leads to large thermoelectric effects in the presence of a spin-splitting field and confirmed the theoretical predictions [20, 21]. By extracting the necessary junction parameters and the heater calibration from local conductance measurements, we were able to model the theoretically expected current quantitatively in applied magnetic field and observed excellent agreement between experiment and theory. The inferred Seebeck coefficients reached magnitudes around $-100$ $\mu$V/K, much larger than it is typically observed in metallic structures. The absence of the thermoelectric effect in a nonmagnetic sample of the same design showed that the spin polarization of the junction is crucial for the effect and that spin and heat currents are coupled in high-field superconductor hybrid structures. By measurements of the dependence of the thermal excitation on the thermoelectric current we observed that the thermoelectric signal has a slight nonlinearity in small fields, but is almost completely linear in the gapless region of the superconducting state. Hence, this regime seems promising for high-sensitive electron thermometry in improved devices [28]. Additionally, the direct proof of the thermoelectric effect supports recent theoretical explanations [16–19] for the large nonlocal spin transport signal in ferromagnet superconductor hybrid structures and is thus a further step towards a better understanding of the physics in these systems.

Subsequently, the experiments were extended to ferromagnetic tunnel junctions with superconductors coupled in proximity contact to a ferromagnetic insulator. For these samples we first studied the dependence of the intrinsic exchange field on the applied magnetic field. We could identify the influence of the exchange field on the effective spin-splitting in the superconductor, but observed a different magnetic field dependence than it is expected from the magnetization of the pure ferromagnetic film. The thermoelectric effect itself was measurable in the structures and by including the exchange field to our model we observed again excellent agreement between the measured data and the theoretically expected current. As a part of the spin splitting was now generated by the intrinsic field, the maximum values of the thermoelectric signals shifted to smaller magnetic fields and the samples on top of EuS showed higher signals in smaller applied fields in general. For improved proximity structures, it seems possible to replace the applied field almost completely by the intrinsic one. Hence, thermoelectric current might be generated without having the need of applying a large magnetic field, which would be a further step towards low-temperature thermoelectric devices.

By the use of generalized Onsager equations we were able to calculate the heat flow in the tunnel junctions in the nonlinear limit. To study the nonlinear regime experimentally, an additional voltage was applied across the junction while the thermoelectric signal was measured. Large signals were observed near the gap voltage for ferromagnetic and also for normal metal samples. The resulting heating power showed the behavior which is known from NIS microrefrigerators. We could show that by the use of an ideal ferromagnetic junction the FIS junction would outperform the NIS junction for smaller voltages due to the additional contribution of the linear thermoelectric effect.

Finally, the first measurements of an experiment which has the intention to study the Hanle precession of the quasiparticle spin projection in spin-split superconductors were presented. The experiment was based on previous spin transport measurements [9, 11], but here also the case of perpendicular magnetization between the ferromagnetic electrodes and the applied field was regarded. In the normal state of the aluminum, we performed spin valve measurements for the case of parallel magnetic alignment and we were able to measure Hanle precession of the electron spin for the case of perpendicular magnetic alignment. In the superconducting state of the aluminum, the situation differed. Here the spin transport measurements could be repeated for the case of parallel magnetic alignment. However, in the nonparallel case we noticed that the fringing field of the ferromagnetic electrodes destroys the superconductivity rapidly while its magnetization is rotated into the field direction. For further studies of the spin Hanle effect in superconductors it seems therefore recommendable to fabricate samples where the spin-splitting is boosted by an intrinsic exchange field rather than by the applied field to avoid the need of applying large magnetic fields. As we showed before, this is possible by using europium sulfide substrates.

For the future, further efforts for the improvement of the fabrication of the europium sulfide/aluminum proximity system seem to be promising. There are reports about intrinsic exchange fields in zero magnetic field [35] and reproducing this results will open the way to perform new interesting experiments which require an inhomogeneous magnetization between the spin-splitting field and the magnetization of the electrodes. Furthermore, by structuring the europium sulfide [38] itself the spin-splitting could be controlled locally in the superconductor and a way to fabricate superconducting spin-valve structures might open up.

# References

[1] F. S. Bergeret, A. F. Volkov, and K. B. Efetov. *Odd triplet superconductivity and related phenomena in superconductor-ferromagnet structures.* Reviews of Modern Physics **77**(2005), 1321

[2] R. S. Keizer, S. T. B. Goennenwein, T. M. Klapwijk, G. Miao, G. Xiao, and A. Gupta. *A spin triplet supercurrent through the half-metallic ferromagnet $CrO_2$.* Nature **439**(2006), 825

[3] J. W. A. Robinson, J. D. S. Witt, and M. G. Blamire. *Controlled Injection of Spin-Triplet Supercurrents into a Strong Ferromagnet.* Science **329**(2010), 59

[4] Trupti S. Khaire, Mazin A. Khasawneh, W. P. Pratt, and Norman O. Birge. *Observation of Spin-Triplet Superconductivity in Co-Based Josephson Junctions.* Physical Review Letters **104**(2010), 137002

[5] M. S. Anwar, F. Czeschka, M. Hesselberth, M. Porcu, and J. Aarts. *Long-range supercurrents through half-metallic ferromagnetic $CrO_2$.* Physical Review B **82**(2010), 100501

[6] Matthias Eschrig. *Spin-polarized supercurrents for spintronics.* Physics Today **64**(2010), 43

[7] Matthias Eschrig. *Spin-polarized supercurrents for spintronics: a review of current progress.* Reports on Progress in Physics **78**(2015), 104501

[8] Jacob Linder and Jason W. A. Robinson. *Superconducting spintronics.* Nature Physics **11**(2015), 307

[9] F. Hübler, M. J. Wolf, D. Beckmann, and H. v. Löhneysen. *Long-Range Spin-Polarized Quasiparticle Transport in Mesoscopic Al Superconductors with a Zeeman Splitting.* Physical Review Letters **109**(2012), 207001

[10] C. H. L. Quay, D. Chevallier, C. Bena, and M. Aprili. *Spin imbalance and spin-charge separation in a mesoscopic superconductor.* Nature Physics **9**(2013), 84

[11] M. J. Wolf, F. Hübler, S. Kolenda, H. v. Löhneysen, and D. Beckmann. *Spin injection from a normal metal into a mesoscopic superconductor.* Physical Review B **87**(2013), 024517

[12] M. J. Wolf, C. Sürgers, G. Fischer, and D. Beckmann. *Spin-polarized quasiparticle transport in exchange-split superconducting aluminum on europium sulfide.* Physical Review B **90**(2014), 144509

[13] D. Beckmann. *Spin manipulation in nanoscale superconductors.* Journal of Physics: Condensed Matter **28**(2016), 163001

[14] F. Hübler, J. Camirand Lemyre, D. Beckmann, and H. v. Löhneysen. *Charge imbalance in superconductors in the low-temperature limit.* Physical Review B **81**(2010), 184524

[15] Florian Hübler. *Experimentelle Untersuchung des lokalen und nichtlokalen Transports in Supraleiter-Ferromagnet-Hybridstrukturen.* Dissertation, Karlsruhe Institute of Technology, 2011

[16] M. Silaev, P. Virtanen, F. S. Bergeret, and T. T. Heikkilä. *Long-Range Spin Accumulation from Heat Injection in Mesoscopic Superconductors with Zeeman Splitting.* Physical Review Letters **114**(2015), 167002

[17] I. V. Bobkova and A. M. Bobkov. *Long-range spin imbalance in mesoscopic superconductors under Zeeman splitting.* JETP Letters **101**(2015), 118

[18] Tatiana Krishtop, Manuel Houzet, and Julia S. Meyer. *Nonequilibrium spin transport in Zeeman-split superconductors.* Physical Review B **91**(2015), 121407

[19] I. V. Bobkova and A. M. Bobkov. *Injection of nonequilibrium quasiparticles into Zeeman-split superconductors: A way to create long-range spin imbalance.* Physical Review B **93**(2016), 024513

[20] P. Machon, M. Eschrig, and W. Belzig. *Nonlocal Thermoelectric Effects and Nonlocal Onsager relations in a Three-Terminal Proximity-Coupled Superconductor-Ferromagnet Device.* Physical Review Letters **110**(2013), 047002

[21] A. Ozaeta, P. Virtanen, F. S. Bergeret, and T. T. Heikkilä. *Predicted Very Large Thermoelectric Effect in Ferromagnet-Superconductor Junctions in the Presence of a Spin-Splitting Magnetic Field.* Physical Review Letters **112**(2014), 057001

[22] A. Slachter, F. L. Bakker, J.-P. Adam, and B. J. van Wees. *Thermally driven spin injection from a ferromagnet into a non-magnetic metal.* Nature Physics **6**(2010), 879

[23] J. Flipse, F. L. Bakker, A. Slachter, F. K. Dejene, and B. J. van Wees. *Direct observation of the spin-dependent Peltier effect.* Nature Nanotechnology **7**(2012), 166

[24] Gerrit E. W. Bauer, Eiji Saitoh, and Bart J. van Wees. *Spin caloritronics.* Nature Materials **11**(2012), 391

[25] P. Machon, M. Eschrig, and W. Belzig. *Giant thermoelectric effects in a proximity-coupled superconductor–ferromagnet device.* New Journal of Physics **16**(2014), 073002

[26] Mikhail S. Kalenkov and Andrei D. Zaikin. *Electron-hole imbalance and large thermoelectric effect in superconducting hybrids with spin-active interfaces.* Physical Review B **90**(2014), 134502

[27] Mikhail S. Kalenkov and Andrei D. Zaikin. *Enhancement of thermoelectric effect in diffusive superconducting bilayers with magnetic interfaces.* Physical Review B **91**(2015), 064504

[28] F. Giazotto, P. Solinas, A. Braggio, and F. S. Bergeret. *Ferromagnetic-Insulator-Based Superconducting Junctions as Sensitive Electron Thermometers.* Physical Review Applied **4**(2015), 044016

[29] Francesco Giazotto, Tero T. Heikkilä, Arttu Luukanen, Alexander M. Savin, and Jukka P. Pekola. *Opportunities for mesoscopics in thermometry and refrigeration: Physics and applications.* Reviews of Modern Physics **78**(2006), 217

[30] Juha T. Muhonen, Matthias Meschke, and Jukka P. Pekola. *Micrometre-scale refrigerators.* Reports on Progress in Physics **75**(2012), 046501

[31] M. Nahum, T. M. Eiles, and John M. Martinis. *Electronic microrefrigerator based on a normal-insulator-superconductor tunnel junction.* Applied Physics Letters **65**(1994), 3123

[32] J. P. Pekola, T. T. Heikkilä, A. M. Savin, J. T. Flyktman, F. Giazotto, and F. W. J. Hekking. *Limitations in Cooling Electrons using Normal-Metal-Superconductor Tunnel Junctions.* Physical Review Letters **92**(2004), 056804

[33] Michael Johannes Wolf. *Spin Transport and Proximity Effect in Nanoscale Superconductor Hybrid Structures.* Dissertation, Karlsruhe Institute of Technology, 2013

[34] P. M. Tedrow, J. E. Tkaczyk, and A. Kumar. *Spin-Polarized Electron Tunneling Study of an Artificially Layered Superconductor with Internal Magnetic Field: EuO-Al.* Physical Review Letters **56**(1986), 1746

[35] J. S. Moodera, X. Hao, G. A. Gibson, and R. Meservey. *Electron-Spin Polarization in Tunnel Junctions in Zero Applied Field with Ferromagnetic EuS Barriers.* Physical Review Letters **61**(1988), 637

[36] X. Hao, J. S. Moodera, and R. Meservey. *Thin-film superconductor in an exchange field.* Physical Review Letters **67**(1991), 1342

[37] Y. M. Xiong, S. Stadler, P. W. Adams, and G. Catelani. *Spin-Resolved Tunneling Studies of the Exchange Field in* EuS/Al *Bilayers.* Physical Review Letters **106**(2011), 247001

[38] M. J. Wolf, C. Sürgers, G. Fischer, T. Scherer, and D. Beckmann. *Fabrication and magnetic characterization of nanometer-sized ellipses of the ferromagnetic insulator EuS.* Journal of Magnetism and Magnetic Materials **368**(2014), 49

[39] M. Silaev, P. Virtanen, T. T. Heikkilä, and F. S. Bergeret. *Spin Hanle effect in mesoscopic superconductors.* Physical Review B **91**(2015), 024506

[40] Mark Johnson and R. H. Silsbee. *Interfacial charge-spin coupling: Injection and detection of spin magnetization in metals.* Physical Review Letters **55**(1985), 1790

[41] F. J. Jedema, A. T. Filip, and B. J. van Wees. *Electrical spin injection and accumulation at room temperature in an all-metal mesoscopic spin valve.* Nature **410**(2001), 345

[42] F. J. Jedema, H. B. Heersche, A. T. Filip, J. J. A. Baselmans, and B. J. van Wees. *Electrical detection of spin precession in a metallic mesoscopic spin valve.* Nature **416**(2002), 713

[43] J. M. Kikkawa and D. D. Awschalom. *Lateral drag of spin coherence in gallium arsenide.* Nature **397**(1999), 139

[44] Ian Appelbaum, Biqin Huang, and Douwe J. Monsma. *Electronic measurement and control of spin transport in silicon.* Nature **447**(2007), 295

[45] Stephen Blundell. *Magnetism in condensed matter / Stephen Blundell* (Oxford [u.a.] : Oxford Univ. Pr., Oxford, 2006), repr. edition

[46] Michael Tinkham. *Introduction to superconductivity / Michael Tinkham* (Dover Publications, INC., Mineola, New York, 2004), 2nd edition

[47] J. Bardeen, L. N. Cooper, and J. R. Schrieffer. *Microscopic Theory of Superconductivity.* Physical Review **106**(1957), 162

[48] Leon N. Cooper. *Bound Electron Pairs in a Degenerate Fermi Gas.* Physical Review **104**(1956), 1189

[49] N. N. Bogoljubov. *On a new method in the theory of superconductivity.* Il Nuovo Cimento (1955-1965) **7**(2007), 794

[50] Ivar Giaever. *Energy Gap in Superconductors Measured by Electron Tunneling.* Physical Review Letters **5**(1960), 147

[51] Kazumi Maki. *Pauli Paramagnetism and Superconducting State. II.* Progress of Theoretical Physics **32**(1964), 29

[52] Peter Fulde. *High field superconductivity in thin films.* Advances in Physics **22**(1973), 667

[53] R. Meservey, P. M. Tedrow, and Ronald C. Bruno. *Tunneling measurements on spin-paired superconductors with spin-orbit scattering.* Physical Review B **11**(1975), 4224

[54] A. A. Abrikosov and L. P. Gor'kov. Zh. Eksp. Teor. Fiz. **39**(1960), 1781

[55] Kazumi Maki. *The Behavior of Superconducting Thin Films in the Presence of Magnetic Fields and Currents.* Progress of Theoretical Physics **31**(1964), 731

[56] S. Skalski, O. Betbeder-Matibet, and P. R. Weiss. *Properties of Superconducting Alloys Containing Paramagnetic Impurities.* Physical Review **136**(1964), A1500

[57] P. M. Tedrow and R. Meservey. *Spin-Dependent Tunneling into Ferromagnetic Nickel.* Physical Review Letters **26**(1971), 192

[58] John Clarke. *Experimental Observation of Pair-Quasiparticle Potential Difference in Nonequilibrium Superconductors.* Physical Review Letters **28**(1972), 1363

[59] M. Tinkham and John Clarke. *Theory of Pair-Quasiparticle Potential Difference in Nonequilibrium Superconductors.* Physical Review Letters **28**(1972), 1366

[60] Albert Schmid and Gerd Schön. *Linearized kinetic equations and relaxation processes of a superconductor near T.* Journal of Low Temperature Physics **20**(1974), 207

[61] Neil W. Ashcroft and N. David Mermin. *Festkörperphysik* (Oldenbourg Verlag München, München, 2013), 4. edition

[62] Melvin Cutler and N. F. Mott. *Observation of Anderson Localization in an Electron Gas.* Physical Review **181**(1969), 1336

[63] T. M. Klapwijk. *Proximity Effect From an Andreev Perspective.* Journal of Superconductivity **17**(2004), 593

[64] A. F Andreev. *The thermal conductivity of the intermediate state in superconductors.* Zh. Eksp. Teor. Fiz. **46**(1964), 1823

[65] P.G. De Gennes. *Boundary Effects in Superconductors.* Reviews of Modern Physics **36**(1964), 225

[66] A. I. Buzdin. *Proximity effects in superconductor-ferromagnet heterostructures.* Reviews of Modern Physics **77**(2005), 935

[67] T. Tokuyasu, J. A. Sauls, and D. Rainer. *Proximity effect of a ferromagnetic insulator in contact with a superconductor.* Physical Review B **38**(1988), 8823

[68] Audrey Cottet, Daniel Huertas-Hernando, Wolfgang Belzig, and Yuli V. Nazarov. *Spin-dependent boundary conditions for isotropic superconducting Green's functions.* Physical Review B **80**(2009), 184511

[69] Jakob Brauer. *Lokaler und nichtlokaler Transport in Normalleiter-Supraleiter-Heterostrukturen.* Dissertation, Karlsruhe Institute of Technology, 2009

[70] Alexandr Cosceev, Christoph Sürgers, Hans-Gerd Boyen, Peter Schweiss, and Hilbert v. Löhneysen. *Superconducting state of very thin Pd films deposited on a diluted insulating $Eu_xSr_{1-x}S$ ferromagnet.* Physical Review B **83**(2011), 174516

[71] C. M. Mayr, F. Metawe, P. Grünberg, and W. Zinn. *Optical investigations and light scattering from spinwaves in thin films of ferromagnetic EuS.* Journal of Magnetism and Magnetic Materials **13**(1979), 177

[72] J. Köhne, G. Mair, N. Rasula, B. Saftic, and W. Zinn. *EuS thin film properties in relation to stoichiometry and defects.* Le Journal de Physique Colloques **41**(1980), C5

[73] B. Saftić, N. Rašula, W. Zinn, and J. Chevallier. *Molecular beam epitaxy and magnetic properties of EuS films on silicon.* Journal of Magnetism and Magnetic Materials **28**(1982), 305

[74] Christoph Sürgers. *private communication*

[75] W. Zinn. *Microscopic studies of magnetic properties and interactions recent results on europium-monochalcogenides.* Journal of Magnetism and Magnetic Materials **3**(1976), 23

[76] S. Kolenda, M. J. Wolf, and D. Beckmann. *Observation of Thermoelectric Currents in High-Field Superconductor-Ferromagnet Tunnel Junctions.* Physical Review Letters **116**(2016), 097001

[77] M. Münzenberg and J. S. Moodera. *Superconductor-ferromagnet tunneling measurements indicate sp-spin and d-spin currents.* Physical Review B **70**(2004), 060402

[78] J. A. X. Alexander, T. P. Orlando, D. Rainer, and P. M. Tedrow. *Theory of Fermi-liquid effects in high-field tunneling.* Physical Review B **31**(1985), 5811

[79] P. M. Tedrow, J. T. Kucera, D. Rainer, and T. P. Orlando. *Spin-Polarized Tunneling Measurement of the Antisymmetric Fermi-Liquid Parameter $G_0$ and Renormalization of the Pauli Limiting Field in A1.* Physical Review Letters **52**(1984), 1637

[80] R. C. Dynes, V. Narayanamurti, and J. P. Garno. *Direct Measurement of Quasiparticle-Lifetime Broadening in a Strong-Coupled Superconductor.* Physical Review Letters **41**(1978), 1509

[81] K. Yu. Arutyunov, H.-P. Auraneva, and A. S. Vasenko. *Spatially resolved measurement of nonequilibrium quasiparticle relaxation in superconducting Al.* Physical Review B **83**(2011), 104509

[82] Detlef Beckmann. *private communication*

[83] S. Kolenda, C. Sürgers, G. Fischer, and D. Beckmann. *Thermoelectric effects in superconductor-ferromagnet tunnel junctions on europium sulfide.* arXiv:1704.07241 [cond-mat] (2017). Accepted by Physical Review B

[84] X. S. Wu, P. W. Adams, and G. Catelani. *Density of states, entropy, and the superconducting Pomeranchuk effect in Pauli-limited Al films.* Physical Review B **74**(2006), 144519

[85] G. Catelani, X. S. Wu, and P. W. Adams. *Fermi-liquid effects in the gapless state of marginally thin superconducting films.* Physical Review B **78**(2008), 104515

[86] Stefan Kolenda, Peter Machon, Detlef Beckmann, and Wolfgang Belzig. *Nonlinear thermoelectric effects in high-field superconductor-ferromagnet tunnel junctions.* Beilstein Journal of Nanotechnology **7**(2016), 1579

[87] Lars Onsager. *Reciprocal Relations in Irreversible Processes. I.* Physical Review **37**(1931), 405

[88] Lars Onsager. *Reciprocal Relations in Irreversible Processes. II.* Physical Review **38**(1931), 2265

[89] Robert S. Whitney. *Most Efficient Quantum Thermoelectric at Finite Power Output.* Physical Review Letters **112**(2014), 130601

[90] S. Takahashi, H. Imamura, and S. Maekawa. *Spin Imbalance and Magnetoresistance in Ferromagnet/Superconductor/Ferromagnet Double Tunnel Junctions.* Physical Review Letters **82**(1999), 3911

[91] Jan Petter Morten, Arne Brataas, and Wolfgang Belzig. *Spin transport in diffusive superconductors.* Physical Review B **70**(2004), 212508

[92] Jan Petter Morten, Arne Brataas, and Wolfgang Belzig. *Spin transport and magnetoresistance in ferromagnet/superconductor/ferromagnet spin valves.* Physical Review B **72**(2005)

[93] P. C. van Son, H. van Kempen, and P. Wyder. *Boundary Resistance of the Ferromagnetic-Nonferromagnetic Metal Interface.* Physical Review Letters **58**(1987), 2271

[94] T. Valet and A. Fert. *Theory of the perpendicular magnetoresistance in magnetic multilayers.* Physical Review B **48**(1993), 7099

[95] W. Thomson. *On the Electro-Dynamic Qualities of Metals:–Effects of Magnetization on the Electric Conductivity of Nickel and of Iron.* Proceedings of the Royal Society of London **8**(1856), 546

[96] T. McGuire and R. Potter. *Anisotropic magnetoresistance in ferromagnetic 3d alloys.* IEEE Transactions on Magnetics **11**(1975), 1018

[97] E. C. Stoner and E. P. Wohlfarth. *A Mechanism of Magnetic Hysteresis in Heterogeneous Alloys.* Philosophical Transactions of the Royal Society of London A: Mathematical, Physical and Engineering Sciences **240**(1948), 599

# A Additional information

| sample pseudonym | real sample name | measurement period |
|---|---|---|
| FIS4 | SK09-G1-S2 | April 2015 |
| FIS3 | SK09-G2-S1 | April/May 2015 |
| FIS1 | SK09-H1-S3 | May 2015 |
| FIS2 | SK09-I3-S4 | June 2015 |
| NIS | SK10-A1-S1 | June/July 2015 |
| EUS1 | EuS10-H2-S2 | October 2015 |
| EUS2 | EuS10-H4-S2 | November 2015 |
| EUS3 | EuS10-I1-S3 | February/March 2016 |
| FIS5 | SK08-B4-S2 | October/November 2014 |

**Table A.1:** Assignment of the here used sample pseudonyms to the real sample names that were used while processing and measuring the sample. The measurement period is given approximately.

# Acknowledgements

Zum Abschluss möchte ich mich sehr herzlich bei allen Personen bedanken, die mich während der Anfertigung dieser Arbeit unterstützt haben.

An erster Stelle möchte ich mich bei Dr. Detlef Beckmann für die hervorragende Betreuung der Arbeit bedanken. Ohne ihn hätte ich nicht auf diesem interessanten Themengebiet forschen können und die Erstellung dieser Arbeit wäre nicht möglich gewesen. Vielen Dank für die kompetente Hilfe und die erhellenden fachlichen Diskussionen, die wir miteinander führen konnten.

Professor Dr. Alexey Ustinov danke ich für die Übernahme des Koreferats.

Für die Unterstützung bei der Fabrikation und der Charakterisierung der Europiumsulfidfilme möchte ich mich bei Dr. Christoph Sürgers bedanken. Vielen Dank, dass ich von deiner großen experimentellen Erfahrung profitieren konnte.

Des Weiteren danke ich Dr. Gerda Fischer für die Magnetisierungsmessungen an den Europiumsulfidfilmen.

Dr. Michael Wolf danke ich für die gute Einarbeitung zu Beginn meiner Arbeitszeit. Außerdem möchte ich mich bei allen Kollegen und Kolleginen am INT für die angenehme Arbeitsatmosphäre in Büro und Labor bedanken. Herauszuheben ist hierbei Simone Dehm, die mir immer wieder mit nützlichen Tipps bezüglich der Probenherstellung geholfen hat.

Ein großer Dank gebührt meiner Familie und meinen Freunden, die mich immer auf meinem Weg unterstützt haben. Meiner Freundin Nayancee Pandey danke ich für die Geduld, die sie mit mir in dieser nicht immer ganz einfachen Zeit hatte. Vielen Dank auch für das Korrekturlesen und die guten Vorschläge die Sie mir gemacht hat.